ABSTRACT

IMPLEMENTATION OF A THREE-DIMENSIONAL NON-INTRUSIVE PARTICLE TRACKING SYSTEM

by
Vivek Gupta

A Three-Dimensional Non-Intrusive Particle Tracking System has been developed at NJIT's Particle Technology Center to provide experimental results for validating theories being developed in the field of Particle Technology. The system utilizes the principle of magnetic induction between several high-frequency miniature transmitters mounted inside a sphere and a set of receiving loop antennae mounted outside the experimental apparatus. Basic theories and algorithms for the tracking system have already been developed. The focus of this thesis is to make the tracking system more accurate, reliable and user-friendly and to apply it to the study of vibrated beds and chute flows. Various techniques to reduce errors in solution and to reduce multiple solutions in orientations are discussed and implemented. Some experimental results of tracking in a vibrated bed of particles are also presented.

IMPLEMENTATION OF A THREE-DIMENSIONAL NON-INTRUSIVE PARTICLE TRACKING SYSTEM

by
Vivek Gupta

A Thesis
Submitted to the Faculty of
New Jersey Institute of Technology
in Partial Fulfillment of the Requirements for the Degree of
Master of Science in Mechanical Engineering

Department of Mechanical Engineering

January 1996

APPROVAL PAGE

IMPLEMENTATION OF A THREE-DIMENSIONAL NON-INTRUSIVE PARTICLE TRACKING SYSTEM

Vivek Gupta

Dr. Rajesh N. Dave, Thesis Advisor Associate Professor of Mechanical Engineering, NJIT	Date
Dr. Anthony D. Rosato, Committee Member Associate Professor of Mechanical Engineering, NJIT	Date
Dr. Kwabena A. Narh, Committee Member Assistant Professor of Mechanical Engineering, NJIT	Date

BIOGRAPHICAL SKETCH

Author: Vivek Gupta

Degree: Master of Science in Mechanical Engineering

Date: January 1996

Undergraduate and Graduate Education

- Master of Science in Mechanical Engineering,
  New Jersey Institute of Technology,
  Newark, New Jersey, 1996

- Bachelor of Engineering in Mechanical Engineering,
  College of Engineering,
  Pune, India, 1994

Major: Mechanical Engineering

Presentations and Publications:

Gupta, V. B., Testing of the Non-Intrusive Particle Tracking System, *Proceedings of the Fifth ASME Region II Graduate Student Technical Conference*, p. 53-54, 1995

This thesis is dedicated to
my parents
and my sister

TABLE OF CONTENTS

TABLE OF CONTENTS
(Continued)

TABLE OF CONTENTS
(Continued)

LIST OF TABLES

Table **Page**

LIST OF FIGURES

Figure **Page**

LIST OF FIGURES
(Continued)

Figure **Page**

LIST OF FIGURES
(Continued)

LIST OF FIGURES
(Continued)

Figure **Page**

LIST OF FIGURES
(Continued)

Figure **Page**

LIST OF FIGURES
(Continued)

Figure **Page**

LIST OF FIGURES
(Continued)

Figure **Page**

LIST OF FIGURES
(Continued)

Figure **Page**

CHAPTER 1

INTRODUCTION

1.1 Motivation

Dry particulates or bulk solids composed of particles of different sizes are frequently encountered in industries. Automatic processing and handling systems like chutes, hoppers and vibrated beds are widely used for handling such material but their design is often far from optimum because the behavior of granular materials in flow is not very well understood. A great amount of research is being done in the field of particle technology to remedy this situation. Much progress has been made in numerical simulations and theoretical investigations as well as practical experimentation. Furthermore, experimental studies are required in order to validate theories and computer simulations.

A particular phenomenon of interest is vibratory size segregation which is frequently encountered in industry and is generally problematic as it counteracts mixing processes. For this reason, vibratory size segregation is an area of extensive research. Though discussion of this phenomenon in details is beyond the scope of this thesis, it can be mentioned that the phenomenon is manifest as the tendency of the larger particles in a granular mixture to rise to the top. There are various theories proposed to explain such behavior [1, 2, 3, 4], however, it appears that no single theory can fully explain it. Detailed experimental measurements such as particle translation and rotations should provide good insight into the underlying phenomenon. To our knowledge, continuous tracking of three dimensional trajectory (translations and rotations) of a particle undergoing segregation has never been reported before. Therefore, the three-dimensional,

non-intrusive particle tracking technique can be a very useful diagnostic tool for studying size segregation in vibrated beds.

In the past, researchers have employed various techniques for the study of particulate flows. Many of the techniques like fiber optic probes and radio pills are intrusive in nature, and hence influence the flow. Others, such as photo-optics, X-rays ultrasound, magnetic tracers, nuclear magnetic resonance etc., though non-intrusive in nature, suffer from some of the drawbacks of high cost, potential health risks, limited accuracy, small experimental space, time averaged measurements and inability to resolve orientation. Dave et al. [5] have provided a background on these techniques and their relative advantages and disadvantages.

A system capable of non-intrusively tracking the motion of an *individual* particle in a three-dimensional flow has been developed at the Particle Technology Center at New Jersey Institute of Technology. The system is based on the principle of magnetic induction coupling and has advantages over other systems as it is non-intrusive, low cost, free of health risks and resolves true three dimensional motion in real-time. Theoretical aspects of this system are discussed in Dave and Bukiet [6]. The method involves tracking a sphere containing three small transmitters, associated electronic circuitry and a power supply, as it moves through the flow space. These embedded transmitters induce voltages in the array of receiving loop antennae surrounding the flow space.

Given the position and orientation of the transmitting sphere, it is possible to calculate the voltages induced in the antennae by electromagnetic theory as discussed by Dave et al. [4] and Ashok [7]. The system of non-linear equations modeling these

voltages are referred to as the *forward model*. The inverse problem of calculating the position and orientation of the transmitting sphere from the induced voltages is referred to as *backward solution*. Since a closed form solution to the forward model equations can not be found, numerical techniques are employed to solve this over determined system of highly complex and non-linear equations (Dave and Bukiet [6]). Systematic errors are introduced in the solution due to imperfections in the equipment and approximations in the theoretical model. These errors were previously studied by Volcy [10] who proposed a 27-point correction scheme for reducing them. The errors, evident in the form of inaccuracies in the solution and multiple solutions in orientation, are discussed in Chapters Three, Four and Five.

1.2 Research Objectives

The main objectives of this research are to improve the 'Solution Algorithm' to improve the accuracy and reliability of the tracking system by reducing the errors in the results and the multiple solutions in orientations and to apply the tracking system to the 'Vibrated Beds' experiment.

As part of these objectives, the development of an efficient Data Acquisition System (DAS) for the 'Chute Flows' experiments, development and implementation of algorithms for smoothing of results and calculation of linear as well as angular velocities are also undertaken. Also it is proposed to make the tracking system more flexible and user friendly by improving the user interface and developing a single solution system capable of handling multiple setups.

1.3 Outline of Remaining Chapters

Chapter Two presents an overview of the Three-Dimensional Non-Intrusive Particle Tracking System, its components and operation. In Chapter Three, an experimental study of 27-point correction scheme and model-reality voltage plots are presented, while in Chapter Four an empirical equation is proposed to replace the 27-point correction scheme. Chapter Five focuses on the problem of multiple solutions in orientations and describes the techniques used for reducing them. Chapter Six presents some experimental results obtained from the vibrated bed experiments and Chapter Seven discusses data smoothing and velocity calculation techniques. Chapter Eight summarizes the accomplishments of this research, draws conclusions based on current results and outlines directions for future work.

CHAPTER 2

AN OVERVIEW OF THE TRACKING SYSTEM

The tracking system consists of three main parts: 1) the transmitter assembly and associated electronics, 2) the data acquisition system and, 3) the signal processing codes. In what follows, we will discuss the various aspects of this system. Section 2.1 discusses the basic principles of the technique while Section 2.2 describes the signal processing algorithm. Section 2.3 focuses on the hardware aspects, including the transmitter assembly, the data acquisition system and recent progress made in the transmitter electronics and the DAS. Applications of the tracking system to inclined chute flows and vibrated beds are discussed in Chapter Six.

2.1 Basic Concepts

Consider a small loop of wire carrying a sinusoidal current $I = I_0 \sin(\omega t)$, where ω is the frequency. This loop behaves like a small magnetic dipole, and has a magnetic field around it. If another loop is placed anywhere in this magnetic field, then there is a corresponding voltage induced within it. This is known as the *principle of electromagnetic induction*. The strength of the induced voltage depends on the relative position and orientation of the second loop. The current carrying loop is the *transmitter*, and the loop in which voltage is induced is the receiving *antenna*.

It is difficult to find a convenient form for the voltage induced because of the large area of the receiving loop (Dave and Bukiet [6]). This problem is circumvented by using the *principle of reciprocity* (Van Valkenburg [8]) which allows an interchange of the sinusoidal current and induced voltage, if the area of the transmitting loop is very small.

Accordingly, an induced voltage in the transmitting coil can be computed by assuming that the current $I = I_0 \sin(\omega t)$ is flowing in the receiving loop (which is much larger than the small transmitting coil). Then through the principle of reciprocity, this can be transformed into the actual induced voltage in the receiver loop.

2.2 Signal Processing Codes

Based on the principle of electromagnetic induction and assumption of perfect reciprocity, the voltage induced in transmitting coil can be theoretically computed if the physical position and orientation of the transmitting coil is known with respect to the antenna. This formulation is referred to as the *Forward Model*. Using the Forward Model and numerical techniques, the position and orientation of the transmitter can be computed if the induced voltages are known. This computation is referred to as the *Backward Solution.*

2.2.1 Forward Model

The location of the tracking sphere, specified by the spatial location of its center (x, y, z) and its orientation represented by a set of RPY (Roll, Pitch and Yaw) rotations, (α, β, γ) relative to a fixed set of axes, is denoted by $\mathbf{X} = (x, y, z, \alpha, \beta, \gamma)$. Given the location of the tracking sphere $\mathbf{X}$, then v_{ij}, the voltage induced in receiver i due to transmitter j can be expressed as,

$$v_{ij} = f_{ij}(\mathbf{X}) \tag{2.1}$$

If there are p receivers and q transmitters, then there are $m = p \times q$ equations in six position variables $\mathbf{X}$. This model is a system of complex and highly nonlinear equations. For a given value of $\mathbf{X}$, determination of v_{ij} is called the *Forward Solution*.

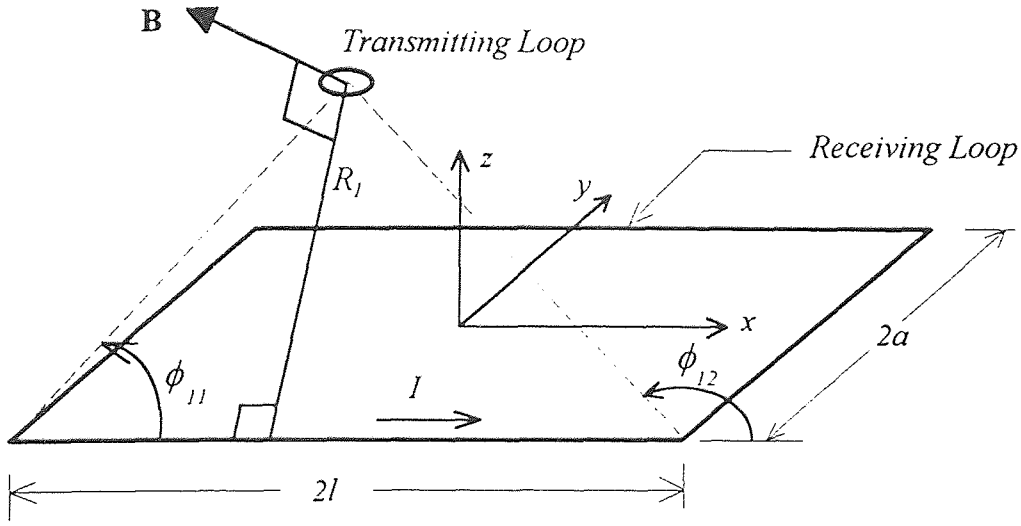

Figure 2.1 Transmitting Coil and Receiving Antenna

The forward model development is based on Fig. 2.1, where the transmitter is depicted as a small circular loop and the receiving antenna is a rectangular loop of dimensions $2l \times 2a$. For the sake of brevity, only the final formulae of the forward model are presented. Details of this model are discussed in [5, 7, 9, 10]. The resultant magnetic flux density $\bar{B}$ is given by,

$$\bar{B} = \sum_{k=1}^{4} \left[\left(\frac{\mu I_i}{4\pi R_k} \right) \left(\cos\varphi_{k1} - \cos\varphi_{k2} \right) \right] \hat{\theta}_k \qquad (2.2)$$

where,

μ is the permeability of the transmission medium (air)

I_i is the current in transmitter i (i = 1, 2, 3,...)

$R_k, \cos\varphi_k, \hat{\theta}_k$ = parameters describing relative position and orientation of the transmitter with respect to the receiving antenna.

The voltage induced in the receiver is the inner product of $\bar{B}$ with the area vector of the transmitter $\bar{A}$ and can be written as,

$$V = -N\omega(\bar{A} \cdot \bar{B}) \tag{2.3}$$

$$or \quad V = -N\omega A(B_x cos\alpha + B_y cos\beta + B_z cos\gamma) \tag{2.4}$$

Here, x, y, z, are the position coordinates of the transmitter in a coordinate system fixed to the receiving loop antenna.

Computation of voltages using the forward model requires the position and orientation of the transmitter in (or relative to) the antenna coordinate system. These computations, involving homogenous RPY coordinate transformations based on Paul [11] were implemented by Agrawal [9]. In brief, the calculations are,

$$X(x,y,z,\alpha,\beta,\gamma) \equiv {}^{g}T_s(x,y,z,\alpha,\beta,\gamma) \tag{2.5}$$

Matrix ${}^{g}T_s$ describes how the transmitter i (i = 1, 2, 3; for three transmitters) is positioned and oriented in the coordinate system of antenna j (j = 1, 2, 3, ... m; the number of antennae). The actual packaging of three transmitters in the sphere results in a deviation from perfect orthogonality of the transmitting cores, resulting in deviation of measured voltages from those predicted by the forward model. This deviation is taken into account by appending a correction matrix to ${}^{g}T_s$ in equation (2.5).

Thus, the forward model can predict induced voltages, given the position and orientation of the transmitters. In the real experiments, the sphere's position and

orientation are unknown while the voltages are known. Therefore, the objective is to predict the position and orientation of the transmitters from these induced antennae voltages. This is done by considering equation (2.1) as an over determined system of m non-linear equations in $\mathbf{X}$. The determination of $\mathbf{X}$ is called the *backward solution* and the method is described in the next section.

2.2.2 Backward Solution

A closed form solution to these non-linear equations (2.1) cannot be found. Hence, we use numerical techniques to solve for x. In theory, only six equations are needed to solve for six unknowns. However, in practice, due to noise problems, low signals at certain positions and orientations, and the inherent non-linearity of the system, we use a larger number of equations. This requires solution of an over determined system of highly complex and non-linear equations.

The forward model equations are given in units of volts, while the actual measured signals from data acquisition are in arbitrary unit of *counts*. Therefore the counts must be scaled down to the actual voltage in volts. This is done by a calibration process described in Section 3.2. A flexible jig onto which the tracking sphere is mounted is used to obtain the data for calibration prior to experiments (and also to conduct controlled trajectory experiments). This jig permits independent control and adjustment of values of x, y, z, α, β and γ when conducting the calibration procedure.

The idea of the backward solution is to find a solution **X** that minimizes the difference or *residual* between the measured values of voltage at actual **X** (i.e. $\mathbf{X}_{actual}$) and those predicted by the m model equations. The residual R is given by,

$$R = \frac{1}{2}\sum_{i=1}^{m} r_i(x)^2 \tag{2.6}$$

where,

$r_i = (V_{model} - V_{mesd})$

V_{model} = voltage computed at **X** by forward model and

V_{mesd} = voltage scanned by data acquisition system at $\mathbf{X}_{actual}$

To minimize equation (2.6), the inverse or backward solution algorithm uses the *lmdif* routine from MINPACK [12], which is Moré's [13] implementation of the Levenberg-Marquardt algorithm. A detailed discussion on the choice and implementation of the Lavenberg-Maquardt algorithm as the solution scheme can be found in Dave et al. [5] and Dave and Bukiet [6]. Figure 2.2 shows a flow chart of the *backward algorithm*. An initial guess **X** is provided as input to the voltage model. Based on this **X**, each transmitter's position and orientation is determined in each antenna's coordinate system by coordinate transformations. Using the forward model given by equations (2.2 - 2.4), a theoretical voltage array V_{model} is computed. A similar measured voltage array V_{mesd} is also obtained from the data acquisition system readings by calibration. An error voltage array EV is then calculated as the absolute difference between the theoretical and measured voltages. The magnitude of this error voltage array is,

$$\|EV\| = \sum_{i=1}^{m} |V_{model} - V_{mesd}| \tag{2.7}$$

To compute the solution that minimizes R, *lmdif* (as shown in the circular loop in Fig. 2.2) iteratively changes X to reduce $\|EV\|$ until it falls within the acceptable range.

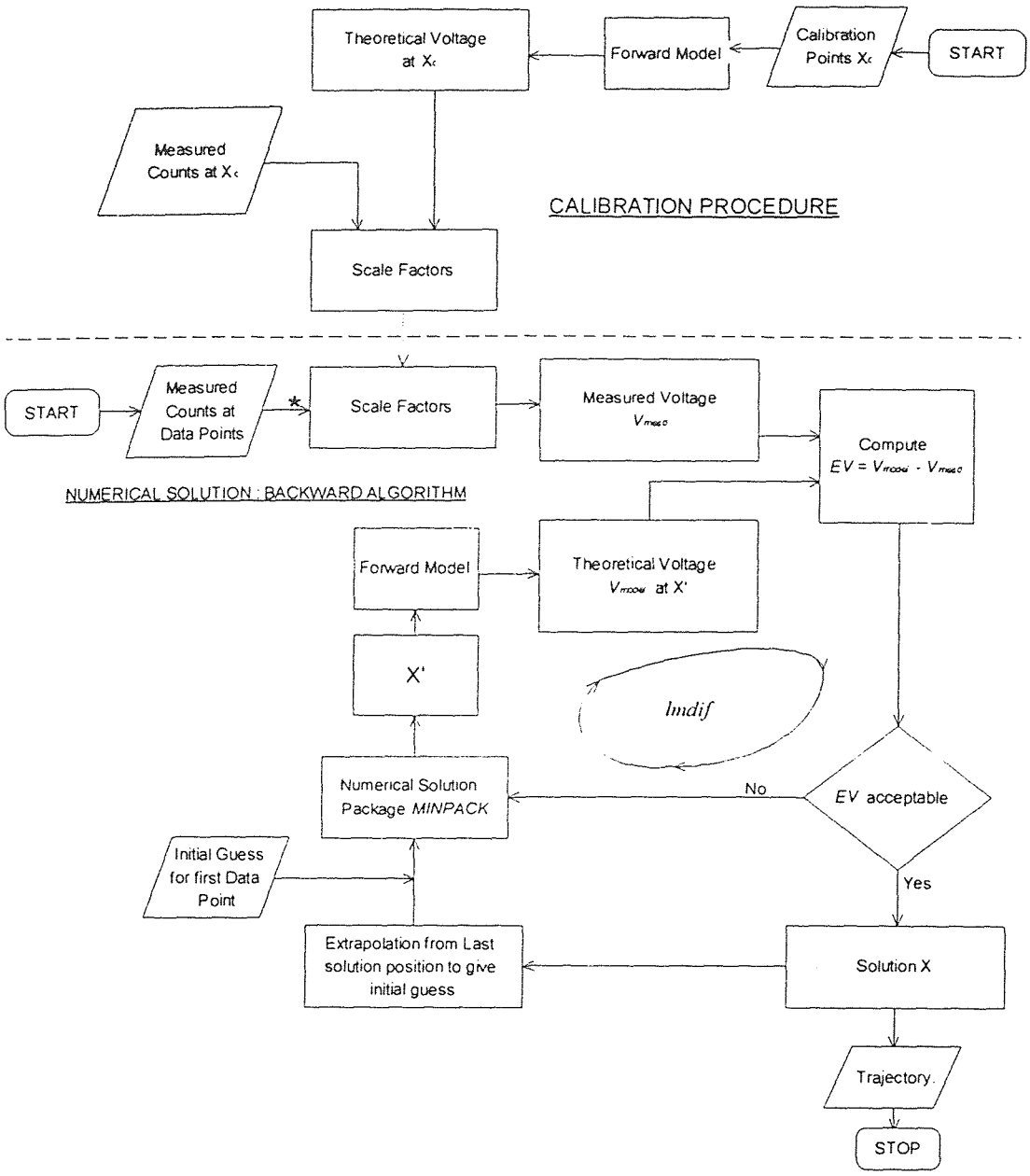

Figure 2.2 Flow Chart of Backward Algorithm

The algorithm also uses a perturbation technique to improve the accuracy of the solutions. This involves providing initial guesses for position and orientation at a data point. From the resulting solutions for the particular data point, the one having lowest $\|EV\|$ value is selected as the best solution. Perturbation techniques are employed to improve the robustness of the algorithm and prevent the solution from straying. The details can be found in [5, 7, 10].

Systematic errors are introduced in the model due to imperfections in equipment and approximations of the theoretical model. These have been minimized by adding an empirical extension, called 27 point correction scheme, proposed by Volcy [10] and implemented by Agrawal [9], to the theoretical model that is discussed in Chapter Three.

2.3 Hardware Development

Successful implementation of the tracking system is contingent on the ability to successfully build, integrate and "tune" the electrical, mechanical and computer hardware needed. Over a period of time, various alternative configurations have been studied, simulated and evaluated to attain the optimal configuration. Prior to conducting tracking experiments on the actual chute (to be described later), experiments are carried out on a model chute to perfect the electronic circuitry as well as the signal processing code.

2.3.1 Experimental Setups

The tracking system has been implemented for three experimental setups: 1) Model-chute, 2) Chute and 3) Vibrated Cylinder. Since the particle tracking technique is based on the

principle of electromagnetic induction, all the setups are fabricated using radio transparent material, e.g., acrylic. The flow areas of interest are surrounded by loop antennae.

The model-chute of dimensions 40"X20"X20" is made of radio transparent acrylic and is mounted with 7 antennae as shown in Fig. 2.3. The dotted rectangles in the figure represent the antennae. The numbers in parentheses show the sequencing of antennae, while the label (i.e. X, Y or Z) gives the direction of the normal to the plane of the antenna. Antennae dimensions are given in Table 2.1. Since the dimensions and aspect ratio of antennae play an important role in the solution process, a detailed study of the antennae configurations has been conducted by Patel [14].

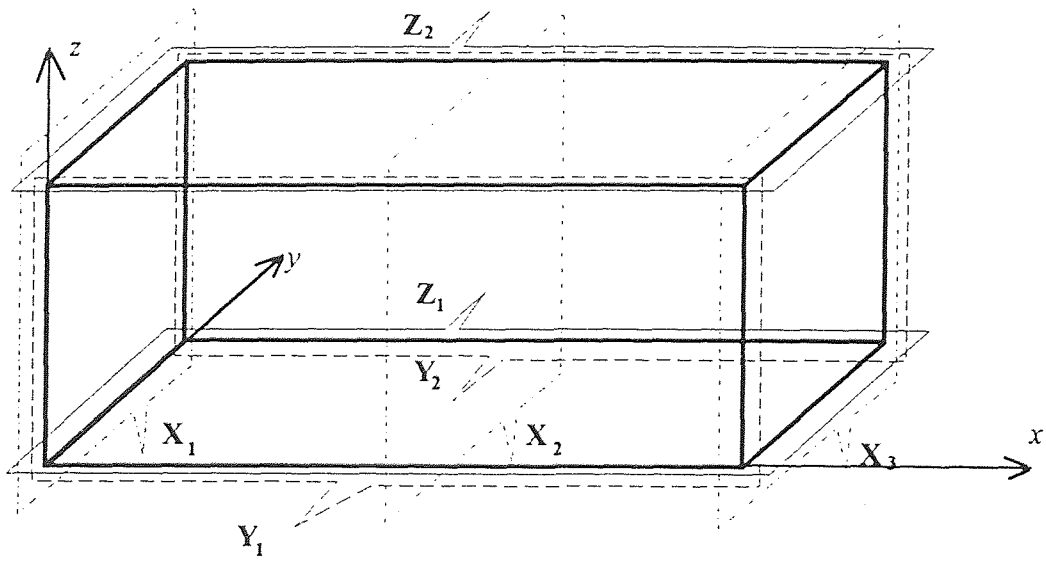

Figure 2.3 Model-chute with Antennae

The actual inclined chute is 10 feet long with a variable inclination angle from zero to 25 degrees. It has an adjustable width from 5 inches to 14.5 inches, and a flexible sluice entrance gate that can open from 0 to 9 inches. Further details on the chute can be found

in Zhang [15]. The entire volume of the chute is made accessible to the tracking sphere by using 27 antennae surrounding the flow region. Details of antennae dimensions and number are given in Table 2.1. The sequencing of the antennae is the same as shown in Fig. 2.3. In this setup, the transmitting sphere is used to measure the trajectory of the center of a sphere during chute flow experiments involving similar solid spheres.

The vibrated cylindrical bed, shown in Fig. 2.4, is 4.5 inches in diameter and its floor can be vibrated from 6 Hz to 1000 Hz (the range being used is 10 Hz to 30 Hz), with an amplitude of up to 0.25 inch. The 1 inch transmitting particle can be tracked in this vibrated bed (consisting of spheres of variable diameters) by six surrounding loop antennae of dimensions given in Table 2.1.

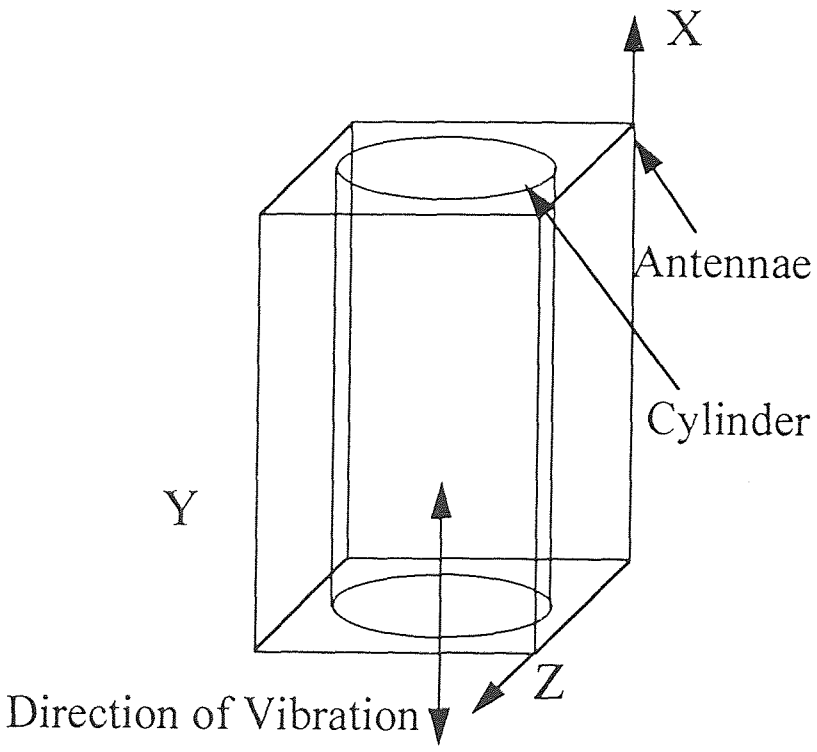

Figure 2.4 Vibrated Bed Setup

Table 2.1 Antennae Specification for the Three Setups

Setup	Total Number of Antennae		Number of antennae	Dimensions
Model-Chute	7	X - Antennae	3	20" X 20"
		Y - Antennae	2	20" X 40"
		Z - Antennae	2	20" X 40"
Chute	27	X - Antennae	11	24" X 24"
		Y - Antennae	8	24" X 32"
		Z - Antennae	8	24" X 32"
Vibrated Bed	6	X - Antennae	2	6" X 6"
		Y - Antennae	2	6" X 10"
		Z - Antennae	2	6" X 10"

2.3.2 The Tracking Sphere and Transmitters

The tracking particle is fabricated from a 1" high density polyethylene sphere typical of those used in the chute flow experiments. A sphere is cut into two halves which are bored hollow and threaded to fit a cylindrical collar. Packaged within the sphere are three oscillators (broadcasting at 2 MHz, 3.65 MHz, and 4.4 MHz), the associated electronic circuitry and batteries. These particular frequencies are chosen in order to avoid interference from standard radio broadcast and radio communication frequencies and also to avoid harmonics.

In the initial stages of the project, a single transmitter was used for particle tracking. Although this had the advantages of being easy to fabricate while consuming less power, it had a major disadvantage. When the transmitter axis was parallel to the plane of an antenna, results were highly inaccurate due to low signal to noise to ratio. Furthermore, due to symmetry of the voltages, if the transmitter was rotated about its own axis, voltage readings in all three antennae do not change (see Fig. 2.5). Such a rotation

of the transmitter, (and hence of the particle within which it is embedded), cannot be detected by the signal processing software.

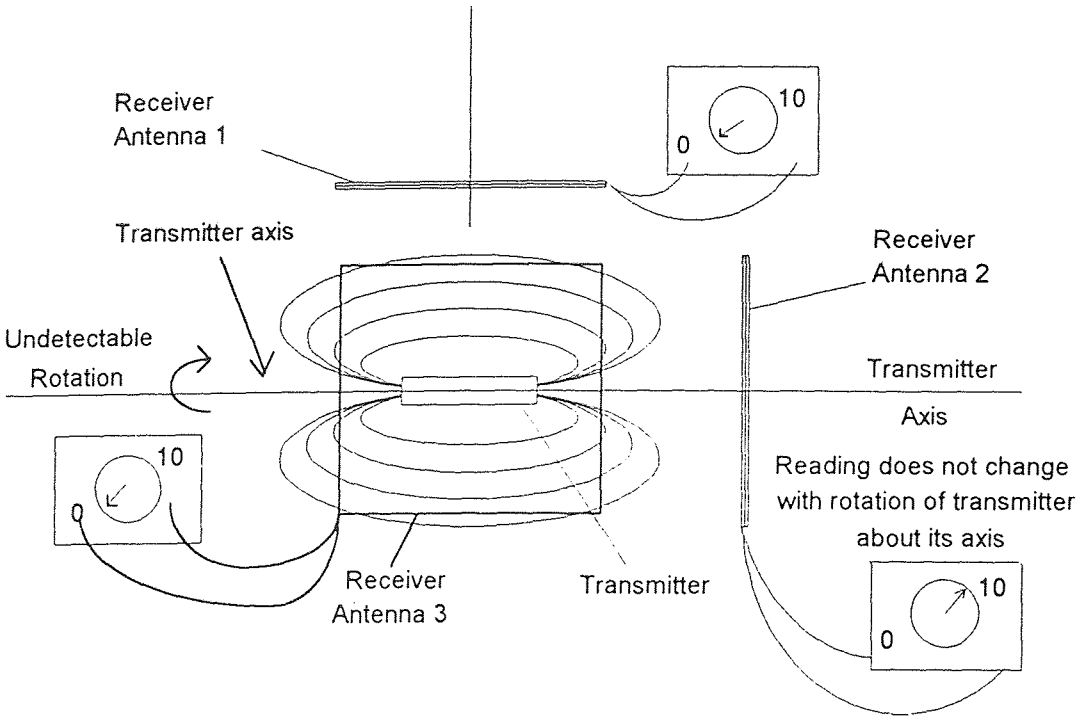

Figure 2.5 Orthogonality Effect
(Adapted from Agrawal [9])

To overcome these problems, a three-transmitter system was designed and fabricated by Troiano [16]. The three transmitter core is shown in Fig. 2.6. The ferrite cross acts as the core of two transmitters, and the third transmitter coil is wound around these two using the flat ferrite of first two transmitters as its core material. Thus, the fields of all the three transmitters are mutually orthogonal. The surface mount devices that are part of the transmitters are mounted on printed circuit boards.

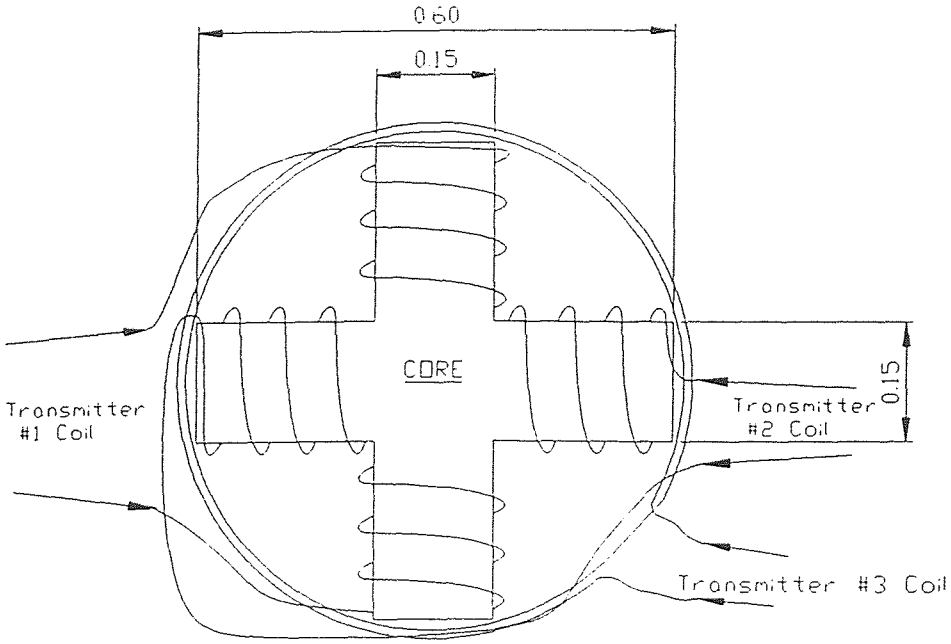

Figure 2.6 The Three-Transmitter Core

The power supply is obtained from two Ni-Cd batteries (Eveready OverTime No. 386) of 1.5V each, located on either end of the transmitter assembly. Fig. 2.7 shows that the relation between battery voltage and the DAS reading is linear in nature. Fig. 2.8 shows the variation of the battery voltage over its life. Evidently the battery has an effective life of less than 20 minutes. Also, the battery is unstable at the start and end of its life. Therefore, it is important to avoid these periods for taking readings. To increase the battery life, it is important to switch off the transmitter when it is not in use. This can be either be done by using either a mechanical or an electronic switch. An optical switch was developed by Ren [17] for this purpose. When the transmitter is in ambient light the optical switch is ON while in dark the switch turn OFF after a 10 to 15 second delay.

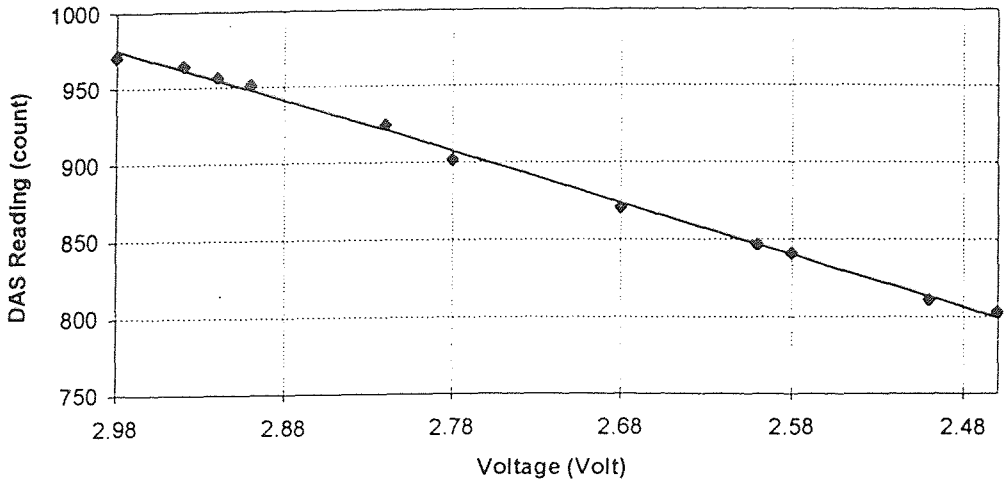

Figure 2.7 Relation of Battery Voltage to DAS Reading (Ren [17])

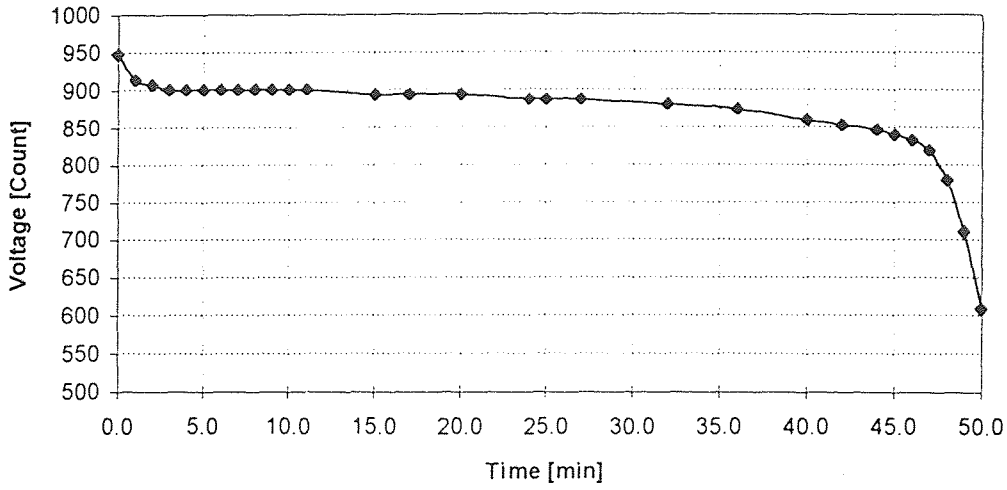

Figure 2.8 Variation of Battery Voltage (Count) over its Life (Ren [17])

2.3.3 The Data Acquisition System (DAS)

The Data Acquisition System has been developed by Troiano [16] and Ren [17]. It consists of the receiving antennae, multiplexers, amplifiers and A/D converters. On the

model-chute there are 7 antennae while the actual chute has 27 antennae. All the antennae consist of uniform hook up wires and have individual pre-amplifiers physically located within a few inches of its terminals. The antennae multiplexers and detecting boards are connected to pre-amplifier outputs with twisted pairs of wires to minimize stray pick up and distributed capacity. Current in the antennae is kept to a minimum so that the pre-amplifier input impedance is high, while output impedance is low so that the twisted pair capacity has little or no effect upon the amplitude of the output signal.

Signals picked up by an antenna are filtered through demodulator boards, fed to a pin on the data acquisition card and then stored on a personal computer. A *channel* is defined as the flow path of a signal from a transmitter (emitting at a given frequency) to the equivalent signal (counts) on the hard disk of PC. The signal path is given by:

receiving antenna $\rightarrow$ demodulator boards $\rightarrow$ input pin on data acquisition card.

Fig. 2.9 shows a schematic of the DAS. The left-dashed block, labeled *Antenna System*, represents sixteen antennae that receive signals from the tracking sphere. Up to sixteen antennae can be read in this setup. The middle dashed block labeled *Antenna Multiplexing and Detection* has three subparts- Multiplexer, Clock circuitry and Demodulator Boards. The multiplexer is used to sequentially select each antenna to be read. The clock generates pulses that are fed to the counter and a variable duty clock. The counter controls the switching of multiplexer between antennae.

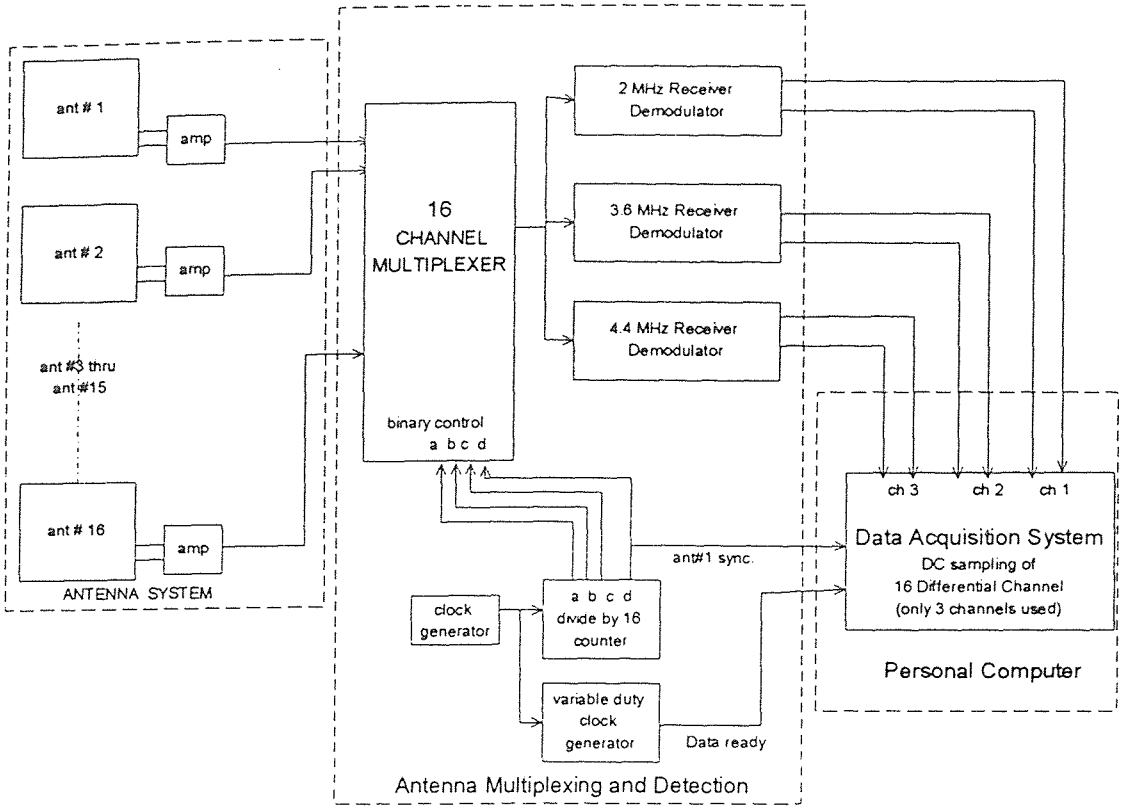

Figure 2.9 Data Acquisition System Schematic

At a given instant, only one antenna is connected to all three demodulator boards, built for each of the 3 frequencies. While the signal induced in an antenna may be positive or negative, only its magnitude is output from the demodulator board. This signal goes to the input pin the of the data acquisition card on the PC. After a delay for transient response of the boards, a *data ready* signal is sent to PC through variable duty clock. This triggers the scanning cycle for scanning sixteen antennae at 2.0, 3.65 and 4.4 MHz frequencies in succession.

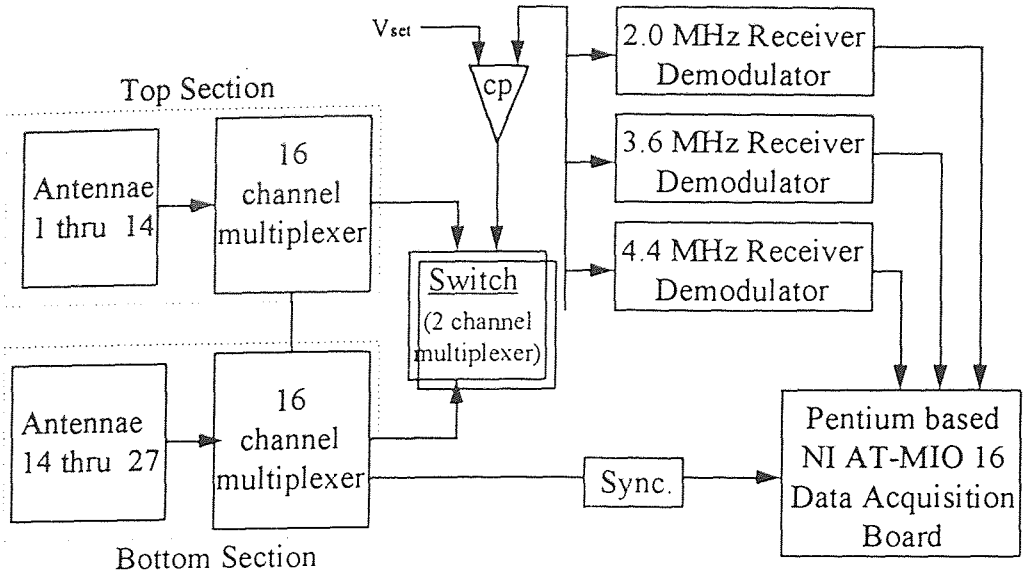

Figure 2.10 Block Diagram of the New Data Acquisition System for Chute

A double buffering technique is used to increase the speed of data acquisition. Data in binary form is stored at a very fast rate in the virtual memory of PC during data acquisition. Later, it is transferred in ASCII format to the hard disk. The rate of data acquisition is 463 data sets/second on a 66 MHz Pentium and 208 data sets/second on a 25 MHz 486 PC. Each set consists of all three frequency readings of sixteen antennae. A switching circuit has been developed for handling the 27 antennae on the actual flow chute since the DAS can manage only 16 antennae. A block diagram of the new Data Acquisition System for Chute developed by Ren [17] is shown in Fig. 2.10.

Twenty-seven antennae are used in the chute system with fourteen antennae in the top section and fourteen in the bottom section, one X-antenna being common to both. In the main DAS board there are two binary controlled 16 channel multiplexers. The chute DAS is divided into two sections in order to save switching time and to acquire more

relevant information. When the transmitting particle is in the top section, readings are obtained only from antennae 1 to 14. The switching circuit, consisting of a 2 channel multiplexer, a comparator and a timer, monitors the signal in sixth X-antenna (common to both the top and bottom section) and compares its signal to a preset level. When the transmitter crosses the X-6 antenna, the switching circuit switches to bottom section and the readings are now obtained from antenna 14 to 27. The timer maintains the switched state for 10 to 20 seconds and then resets to top section.

A much simpler DAS system, similar to that shown in Fig. 2.9, is used for the vibration experiment.

In the following chapters, all the results, except where noted, are obtained from the model-chute setup.

CHAPTER 3

STUDY OF THE 27-POINT SCHEME

3.1 Errors in the Tracking System

Errors are always present in any physical measurement and can be classified into two main types: random errors and systematic errors. Random errors are unpredictable fluctuations that creep into any measurement and are self-normalizing over a period of time. Therefore random errors are also referred to as noise. Systematic errors, on the other hand, are introduced due to imperfections in the equipment and/or operator errors in taking measurements. The systematic errors are not self-normalizing and tend to accumulate and bias the readings. Volcy [10] studied the systematic errors in detail and found that these are introduced due to various reasons such as:

- The field of the transmitter is not perfectly symmetrical
- The amplifier and data acquisition boards are not perfectly linear
- Magnetic coupling exists between antennae
- Higher order terms are neglected in the derivation of the model
- Principle of reciprocity is violated when the transmitter is very near the antenna

To correct these systematic errors, Volcy [10] proposed various correction schemes consisting of empirical extensions to the voltage model in the form of three-dimensional correction maps. Agrawal [9] implemented this 27-point correction scheme. The aim here is to demonstrate effectiveness of the 27-point correction scheme and select an effective reference point for the correction map. Section 3.2 discusses the basic concepts and implementation of the 27-point correction scheme in brief and explains the

nomenclature adopted throughout the remaining sections of this chapter. Sections 3.3 presents model-reality voltage plots while Section 3.4 discusses the effectiveness of the 27-point correction scheme and choice of reference point.

3.2 The 27-Point Correction Scheme

Recall that (Section 2.2.2) the forward model equations are given in units of volts, while the actual measured signals from data acquisition are in arbitrary unit of *counts*. Therefore the counts must be scaled down to the actual voltage in volts. This is done by a process called *calibration*. For the purpose of calibration, voltage readings in units of counts are obtained from the DAS at predecided points called the *calibration points*. The forward model is also used to compute the voltage at the calibration points. A *scaling factor* is then obtained by taking a ratio of these two values. Thus,

$$scaling\ factor = \frac{voltage\ obtained\ from\ forward\ model\ at\ calibration\ points\ (in\ volts)}{voltage\ obtained\ from\ D.A.S.\ at\ calibration\ points\ (in\ counts)} \qquad (3.1)$$

Such a scaling factor is obtained for each antenna-transmitter pair. For example, the model chute setup with 7 antennae has 21 scaling factors when 3 transmitters are used. This approach assumes that the scaling factors remain constant throughout the experimental space. However, it is observed that, in reality the scaling factors vary significantly over the experimental space. This can be attributed to the presence of systematic errors as discussed in Section 3.1. Volcy [10] has proposed to vary the scaling factors for every antenna-transmitter pair over the experimental space by creating an empirical correction map and interpolating correction to scaling factors.

A correction map is then created by using the scaling factors at the 27 points in the octant. A *correction factor* is a correction applied to the theoretical (forward model) voltage to compensate for the systematic errors in the actual voltage. Interpolation functions are set up between these 27 points to find the correction factor at any point in the experimental space. The interpolation functions make use of the symmetry of voltages about the antennae planes and can be summarized as,

$$\text{c. f.} = \psi(x, y, z, \alpha, \beta, \gamma) \tag{3.2}$$

where,

c.f. = correction factor

ψ = interpolation function for calculating the correction factor

(x, y, z, α, β, γ) = position and orientation of transmitter in local antenna coordinates.

Further details about the interpolation functions and implementation of the 27-point correction scheme can be found in Agrawal [9]. The corrective effect of the correction scheme is demonstrated by means of model-reality plots described in the following sections.

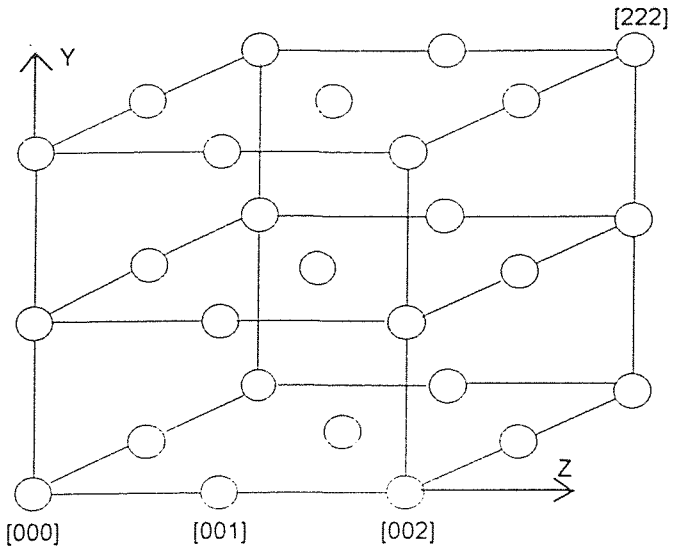

Figure 3.2 The 27 Nodes in an Octant

The 27-point map needs to be set up only once for each antennae configuration. But prior to conducting an experiment, the correction map must be scaled to take care of the environmental changes, electronic drift, change in transmitter voltage and other such factors that might cause an overall scaling of the correction map. One of the 27 points is used as the *reference point* and scaling factor is found at this point using equation (3.1). This scaling factor is compared to that obtained while setting up the 27-point map and a constant correction is applied to the scaling factors obtained previously at all the 27 points. This correction is equal to the ratio of new and old scaling factors at the reference point The three points along the axis of the antenna are considered as possible candidates for choice as reference points. These points, shown in Figure 3.2, are [000], [001] and [002]. Model-reality and error plots are generated in the following sections to show the

effectiveness of the 27-point correction scheme and to choose one of the three points as the reference point.

3.3 Model-Reality Plots

The purpose of making model-reality plots is to compare the theoretical voltages given by the forward model to the actual voltages (obtained from the counts) given by the data acquisition system. Three trajectories (called Type I, Type II and Type III) are chosen along the central planes of the antenna for making the model-reality plots and are described in Sections 3.3.1, 3.3.2 and 3.3.3. Voltage readings (in counts) at these points are collected using the data acquisition system. These readings are converted to volts by using one of the points [000], [001] or [002] as the calibration point. Voltages (in volts) at these points are also given by the forward model since the positions along the trajectory are known. The plot of actual voltages obtained from the data acquisition system and the voltages predicted by the forward model, is called the *model-reality plot*.

Since it is necessary to demonstrate the effectiveness of the 27-point correction scheme, and also choose one of the three points, [000], [001] and [002] as a reference point, there are six possible combinations of the conditions. The plots can be created with or without the 27-point correction scheme for each of the three points as the reference point. An error plot can also be plotted using the data for these six plots. Thus, each type of "model-reality plot set" consists of six model-reality plots and one error plot. In this and the following sections, an antenna of dimensions 20" X 20" is used to generate the model-reality plots. For this antenna, point [000], [001] and [002] are respectively 0", 5"

and 10" away from the plane of the antenna. One complete set of model-reality plots of Type I, II and III generated using a new transmitter (currently being used for experimental work) is presented and explained in this chapter. Another set generated using the old transmitter (used for the initial investigation by Agrawal [9]) is presented in Appendix A. All the plots in this chapter have been scaled up by a factor of 10^6 for better visualization.

3.3.1 Model-Reality Plots: Type I

The model-reality plots of Type I, hereby referred to as M-R (I), are generated using a trajectory normal to the plane of the antenna as shown in Figure 3.3. The z-axis of the antenna (in antenna coordinate system) and the axis of the transmitter are kept coincident and the distance between the transmitter and the antenna is increased from 0" to 20" at 0.5" increments.

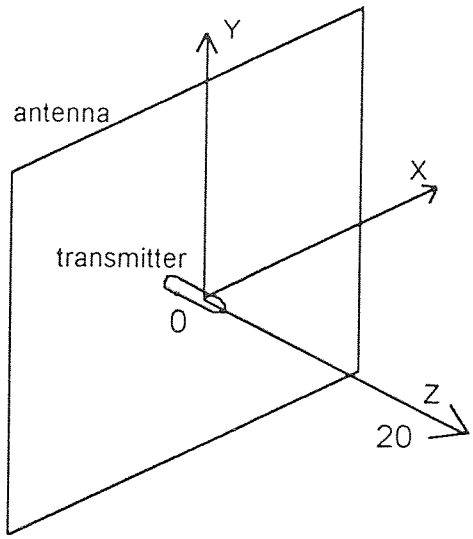

Figure 3.3 Trajectory for M-R (I)

The collected data is used to generate the six model-reality plots. The collected data, converted to volts by calibration, gives rise to the "actual" voltage series. The "model" voltages are generated by the forward model with or without 27-point correction, using either of the three points as the reference point. Figures 3.4 through 3.9 are representative of the model-reality plots of Type I. Fig. 3.10 is the plot of errors, that is deviation of the model voltage from the actual for various conditions, as a percentage of maximum voltage. Careful observation of the error plots in Fig. 3.10 reveals that consistently lower errors are obtained on using 27-point correction with either point [000] or [002] as the reference point.

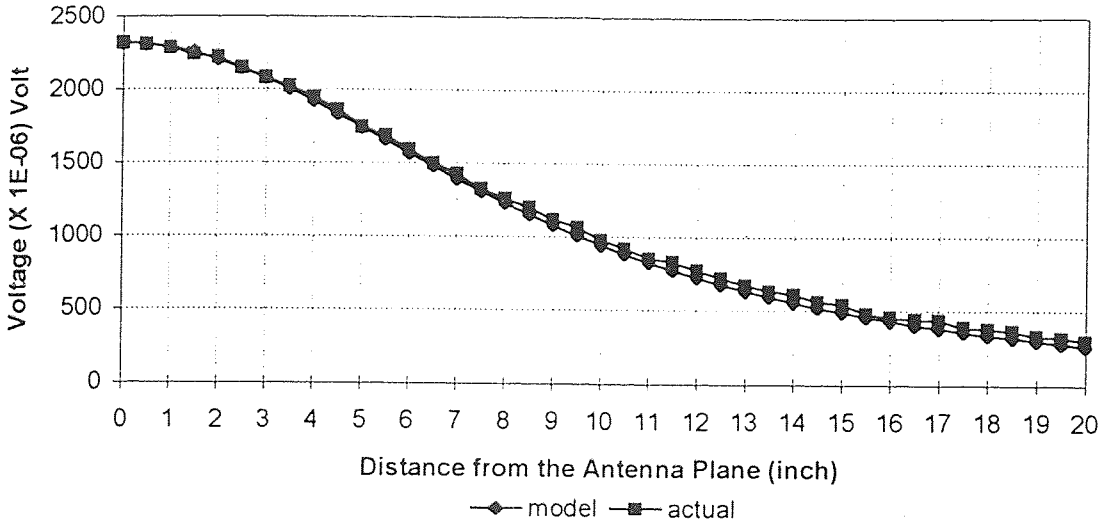

Figure 3.4 M-R (I) no 27-point correction, reference point [000]

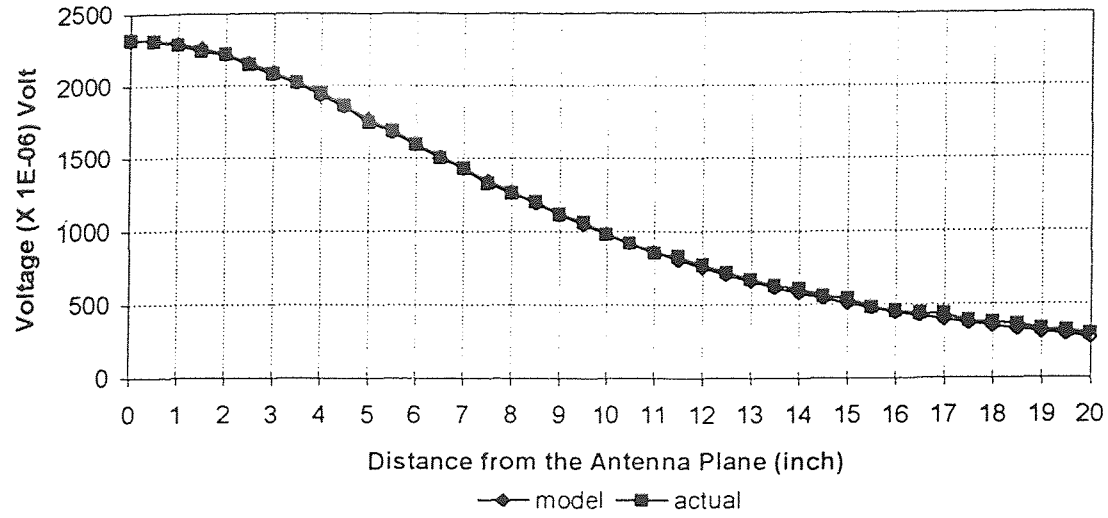

Figure 3.5 M-R (I) using 27-point correction, reference point [000]

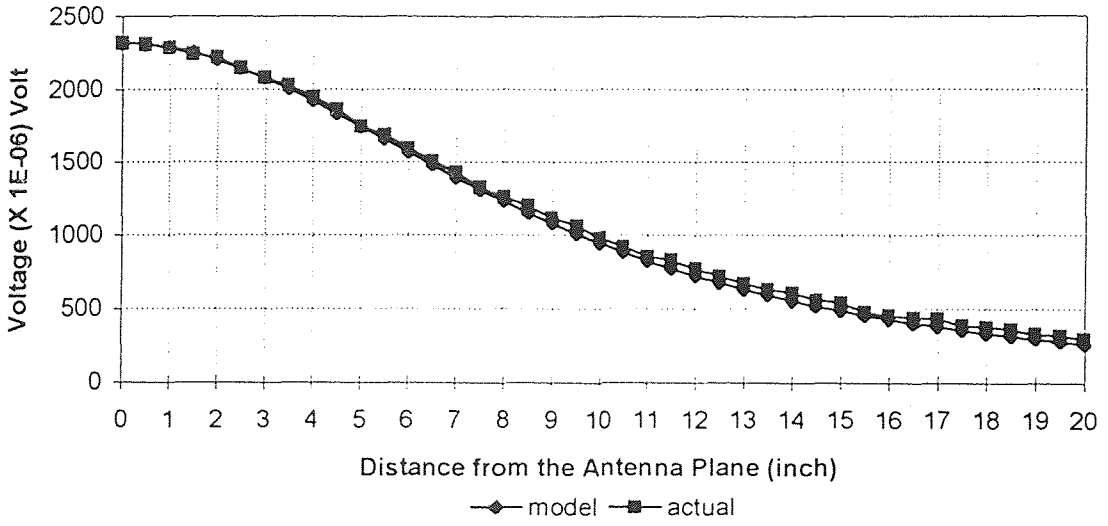

Figure 3.6 M-R (I) no 27-point correction, reference point [001]

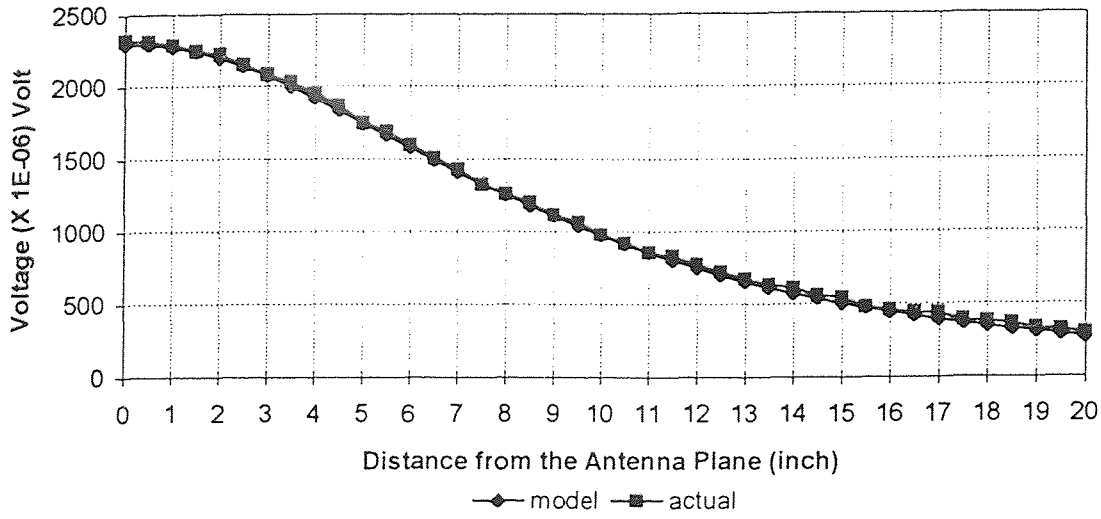

Figure 3.7 M-R (I) using 27-point correction, reference point [001]

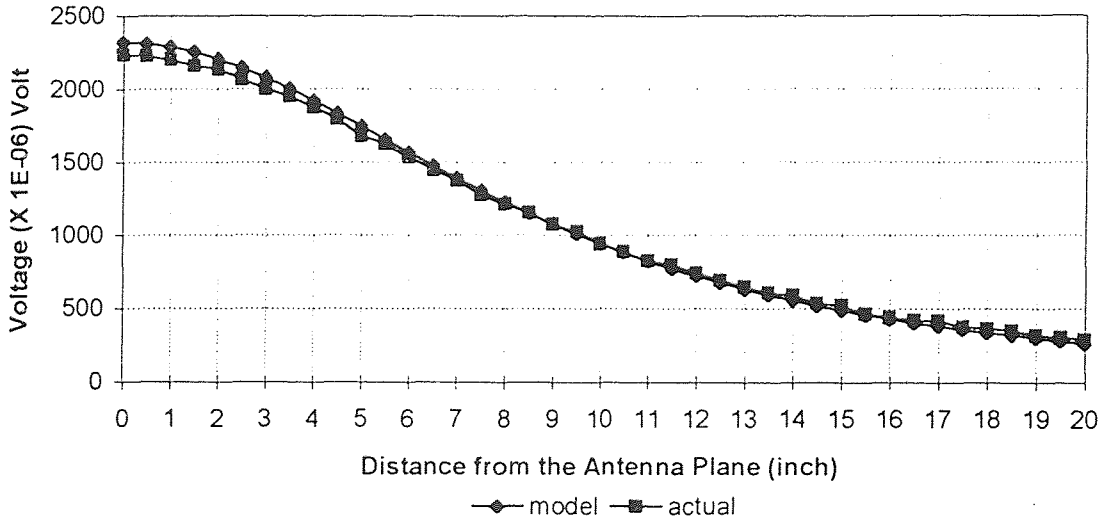

Figure 3.8 M-R (I) no 27-point correction, reference point [002]

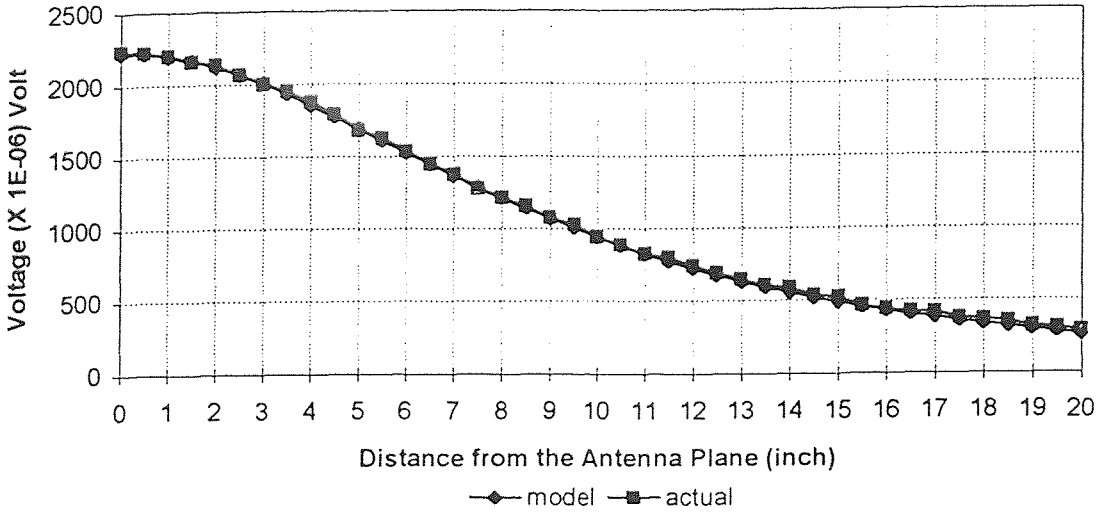

Figure 3.9 M-R (I) using 27-point correction, reference point [002]

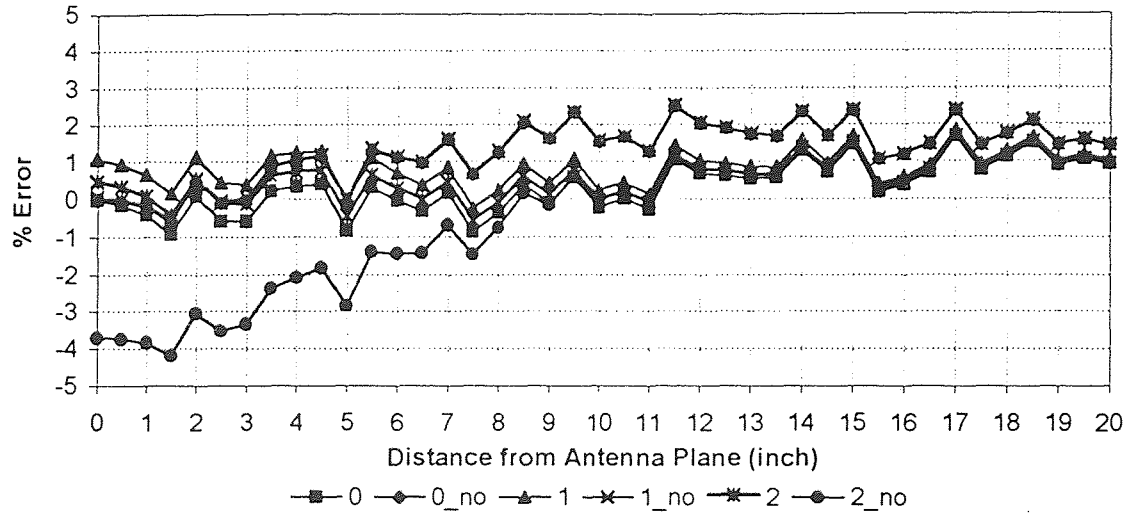

Figure 3.10 Error Plots for M-R (I)

"0", "1" and "2" stand for the cases of using 27-point correction with [000], [001] and [002] as reference points respectively. "0_no", "1_no" and "2_no" are the corresponding cases without using 27-point correction.

3.3.2 Model-Reality Plots: Type II

The model-reality plots of Type II, also referred to as M-R (II), are generated using a trajectory in the plane of an antenna as shown in Figure 3.11. The transmitter is moved in the plane of the antenna with the z-axis of the antenna (in antenna coordinate system) and the axis of the transmitter parallel. The distance between the z-axis of the antenna and the transmitter is varied from -5" to 5" in 0.5" increments.

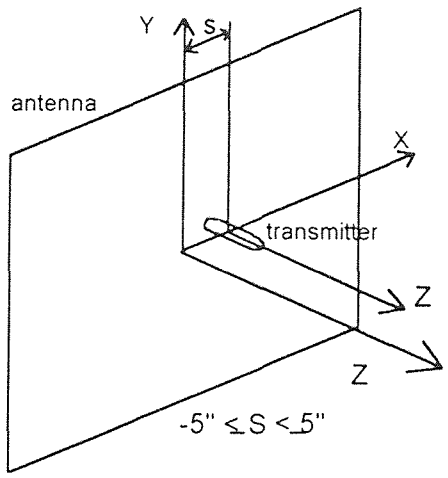

Figure 3.11 Trajectory for M-R (II)

The collected data is used to generate the six model-reality plots. The collected data, converted to volts by calibration, gives rise to the "actual" voltage series. The "model" voltages are generated by the forward model with or without 27-point correction, using either of the three points as reference point. Figures 3.12 to 3.17 are representative of the model-reality plots of Type II. Fig. 3.18 is the plot of errors, that is deviation of the model voltage from the actual for various conditions, as a percentage of maximum

voltage. Careful observation of error plots (Fig. 3.18) shows that using 27-point correction with either point [000] or [002] as the reference point results in least errors.

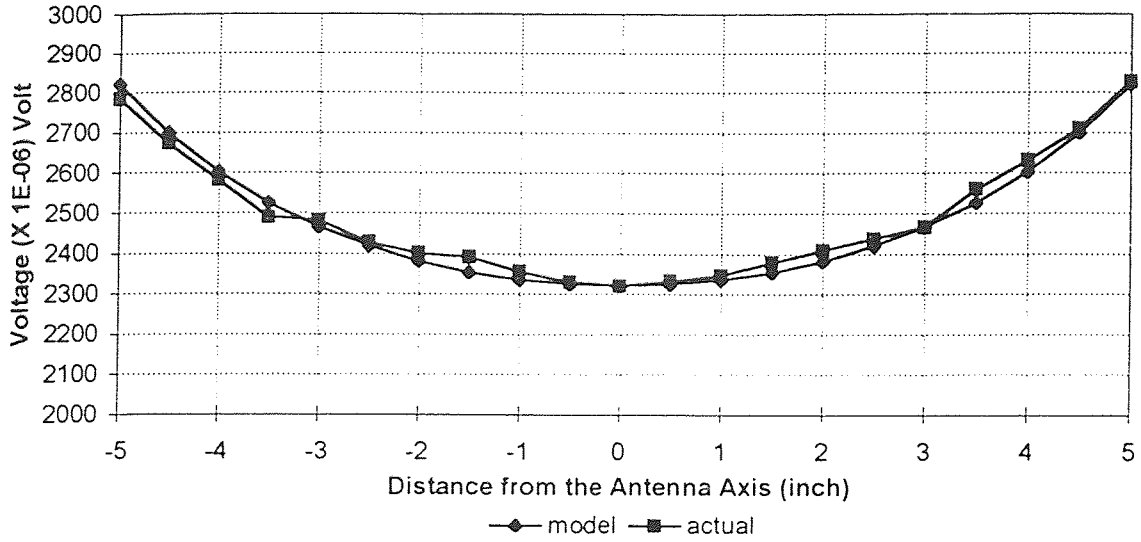

Figure 3.12 M-R (II) no 27-point correction, reference point [000]

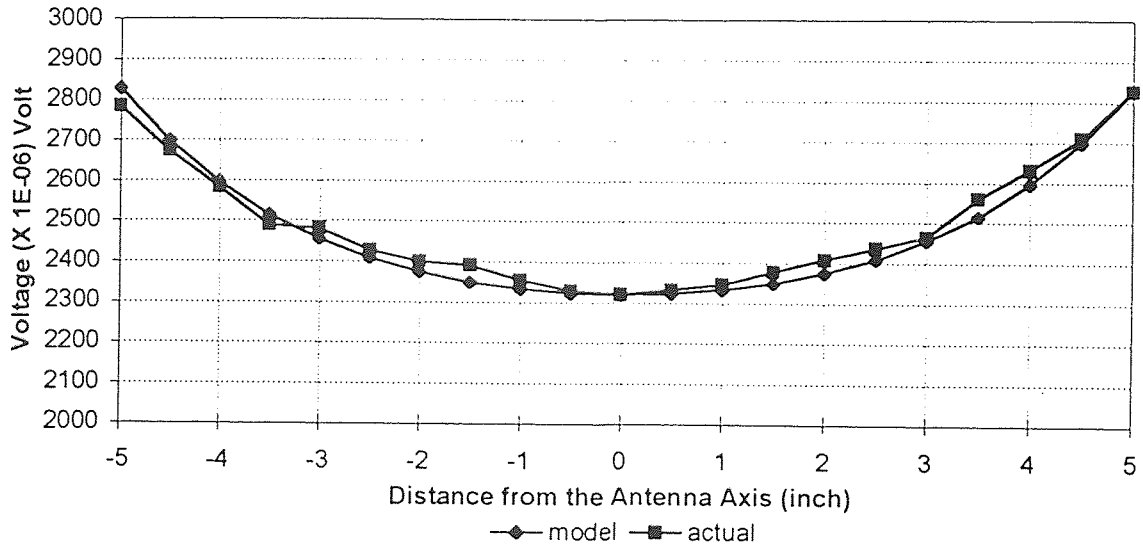

Figure 3.13 M-R (II) using 27-point correction, reference point [000]

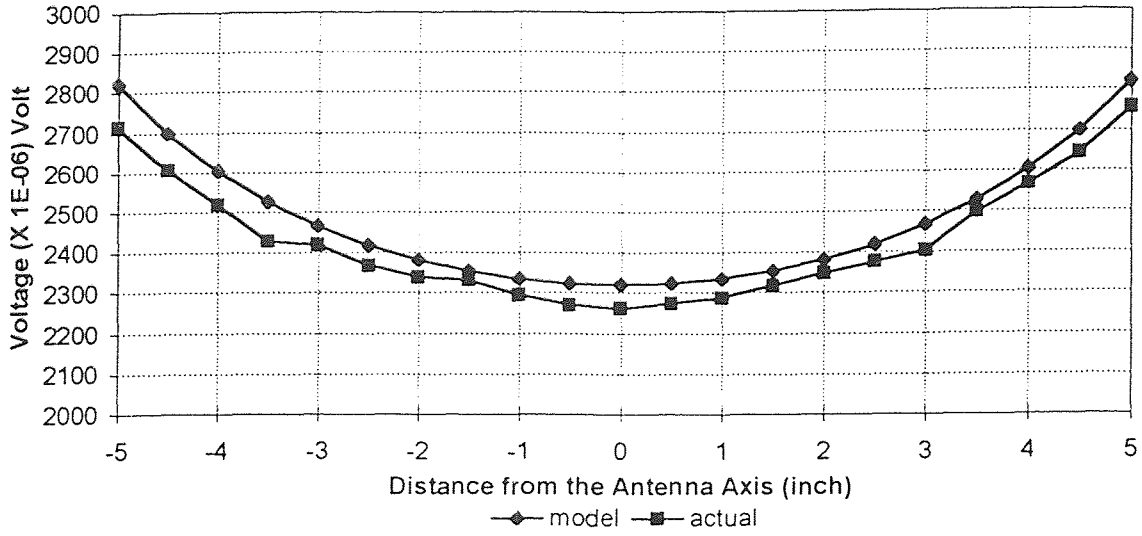

Figure 3.14 M-R (II) no 27-point correction, reference point [001]

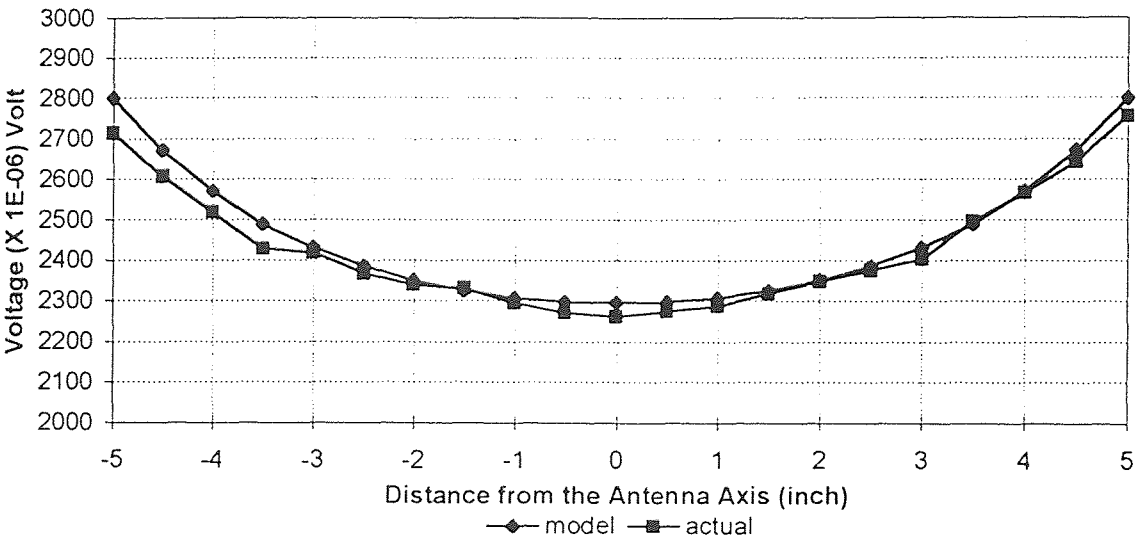

Figure 3.15 M-R (II) using 27-point correction, reference point [001]

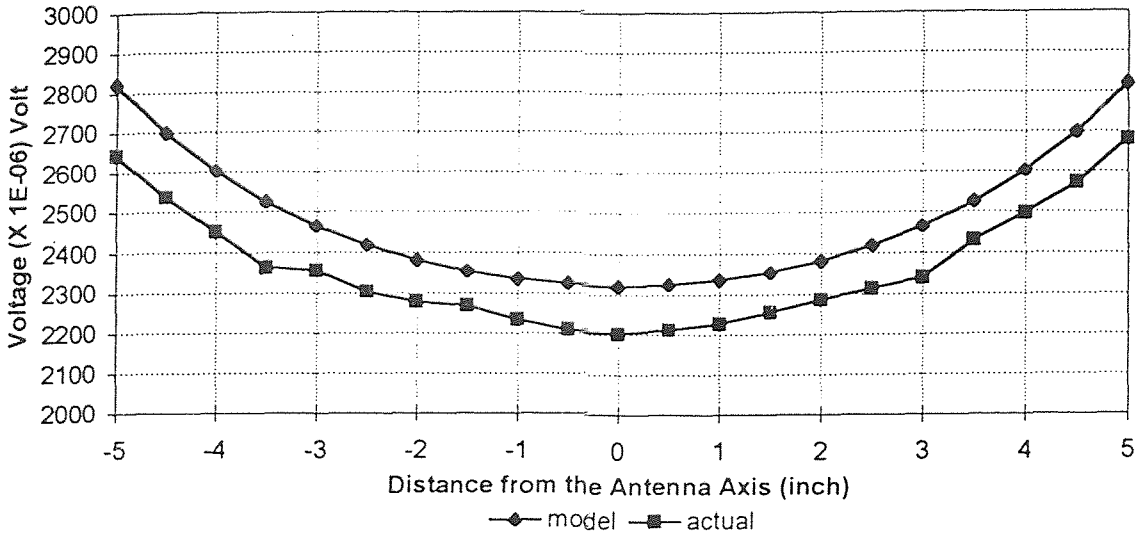

Figure 3.16 M-R (II) no 27-point correction, reference point [002]

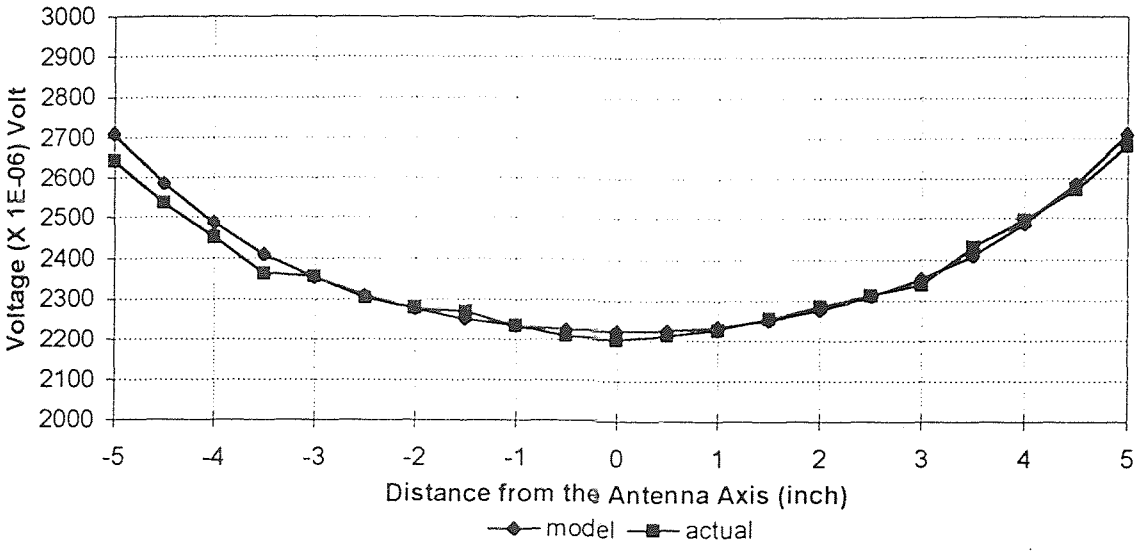

Figure 3.17 M-R (II) using 27-point correction, reference point [002]

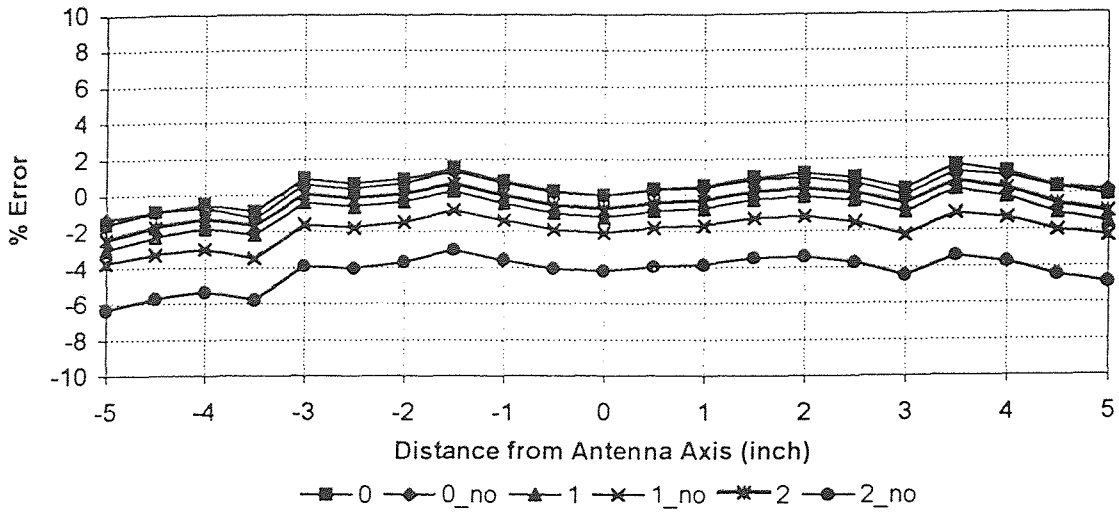

Figure 3.18 Error Plots for M-R (II)

"0", "1" and "2" stand for the cases of using 27-point correction with [000], [001] and [002] as reference points respectively. "0_no", "1_no" and "2_no" are the corresponding cases without using 27-point correction.

3.3.3 Model-Reality Plots: Type III

The model-reality plots of Type III, also referred to as M-R (III), are generated by rotating the transmitter 180° about the Y-axis of the antenna as shown in Figure 3.19. In the antenna system, this is a rotation such that the transmitter axis and antenna Z-axis, which are initially orthogonal, become parallel and coincident and then are orthogonal again as the transmitter completes a rotation of 180 degrees. Thus, the angle between the z-axis of the antenna and the transmitter axis is varied from -90° to 90° in 10° increments.

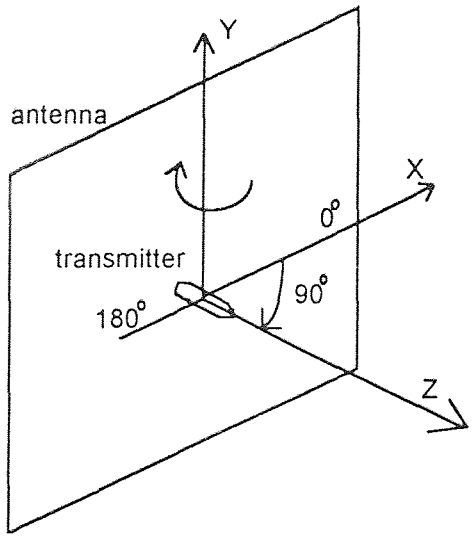

Figure 3.19 Trajectory for M-R (III)

The collected data is used to generate the six model-reality plots. The collected data, converted to volts by calibration, gives rise to the "actual" voltage series. The "model" voltages are generated by the forward model with or without 27-point correction, using either of the three points as the reference point. Figures 3.20 through 3.26 are representative of the model-reality plots of Type III. Fig. 3.27 is the plot of errors, that is deviation of the model voltage from the actual for various conditions, as a percentage of maximum voltage. Careful observation of the error plots in Fig. 3.26 shows that consistently lower errors are obtained when 27-point correction is used with either point [000] or [002] as the reference point.

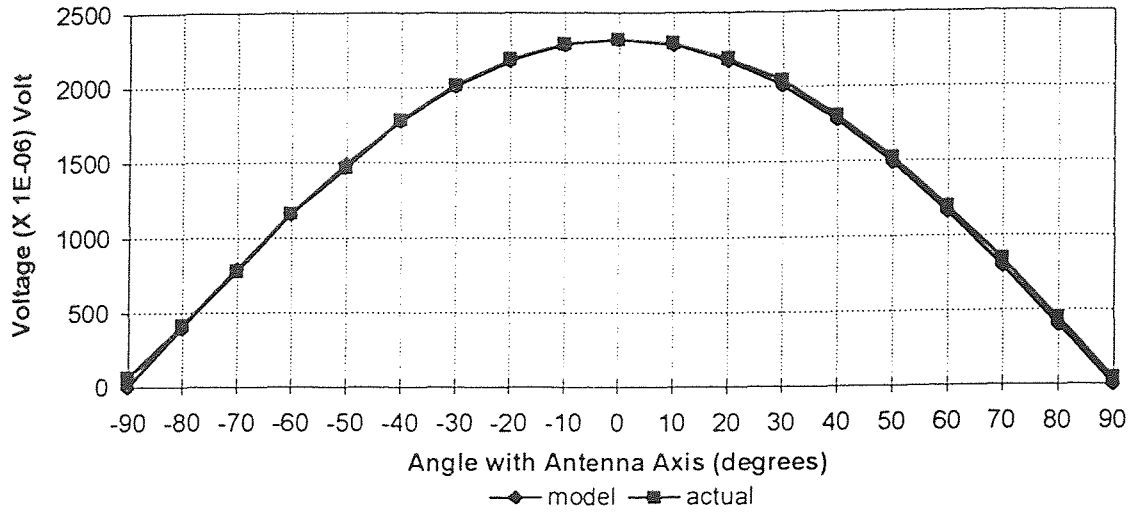

Figure 3.20 M-R (III) no 27-point correction, reference point [000]

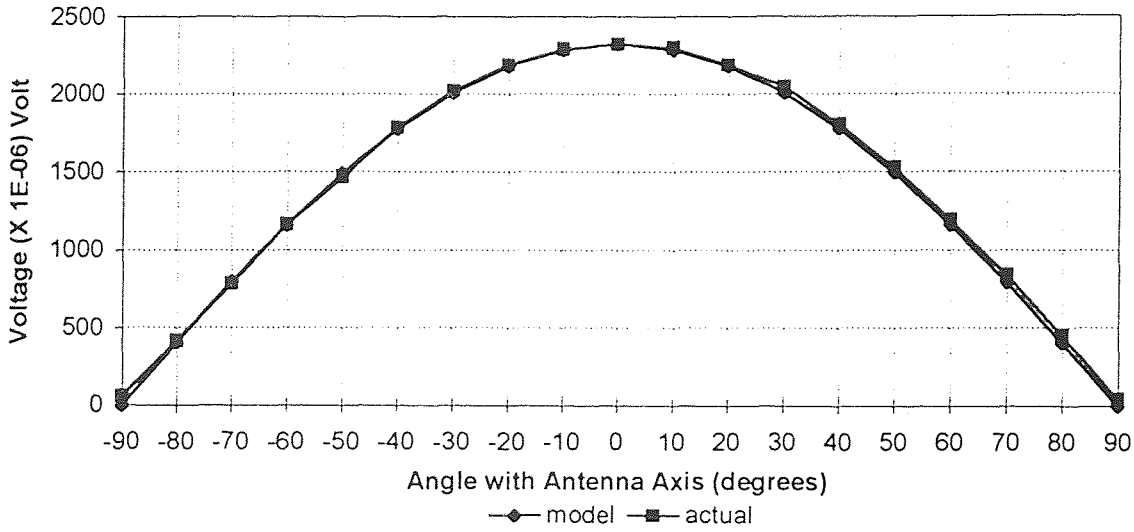

Figure 3.21 M-R (III) using 27-point correction, reference point [000]

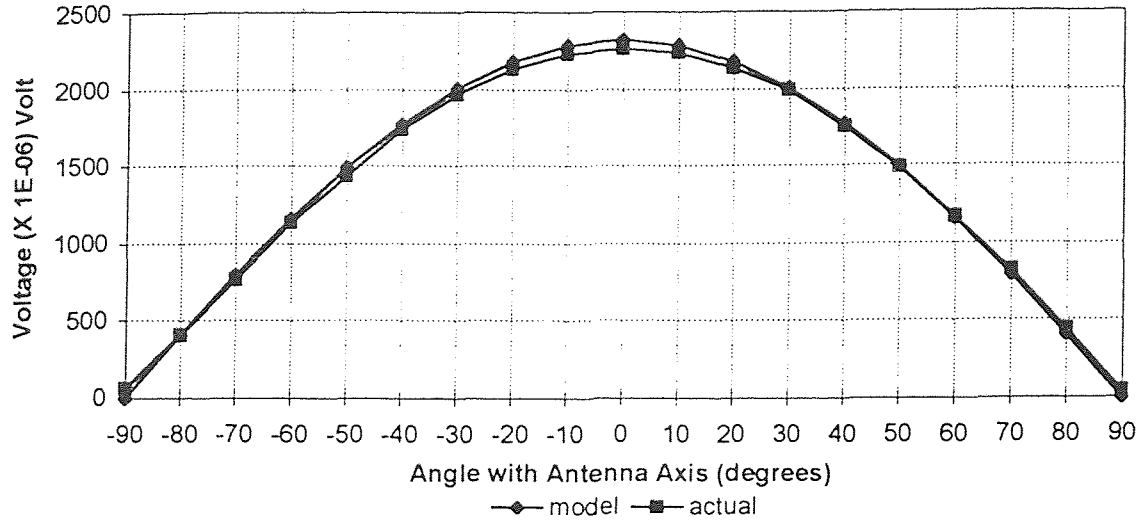

Figure 3.22 M-R (III) no 27-point correction, reference point [001]

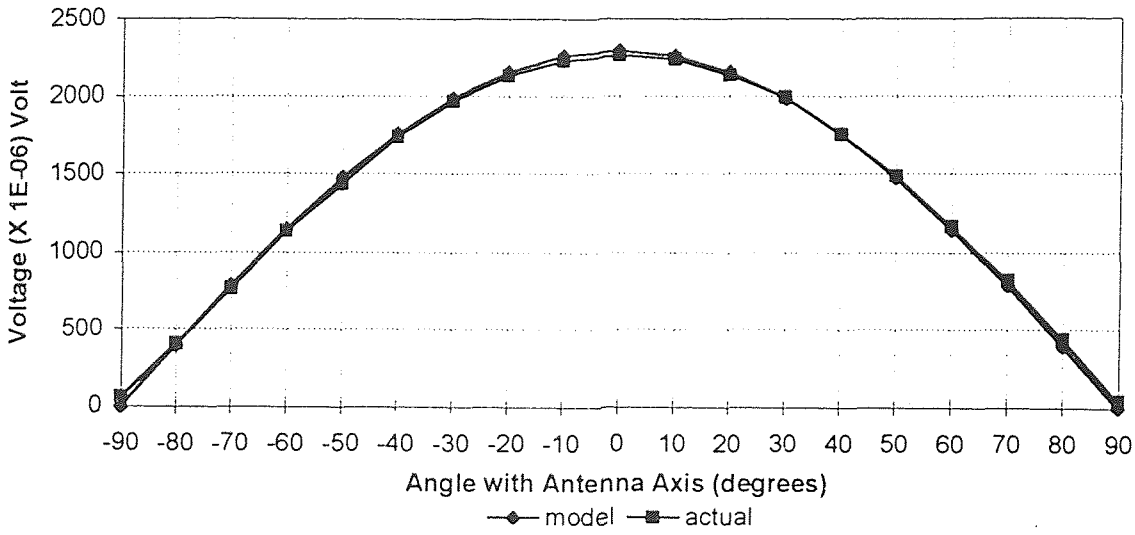

Figure 3.23 M-R (III) using 27-point correction, reference point [001]

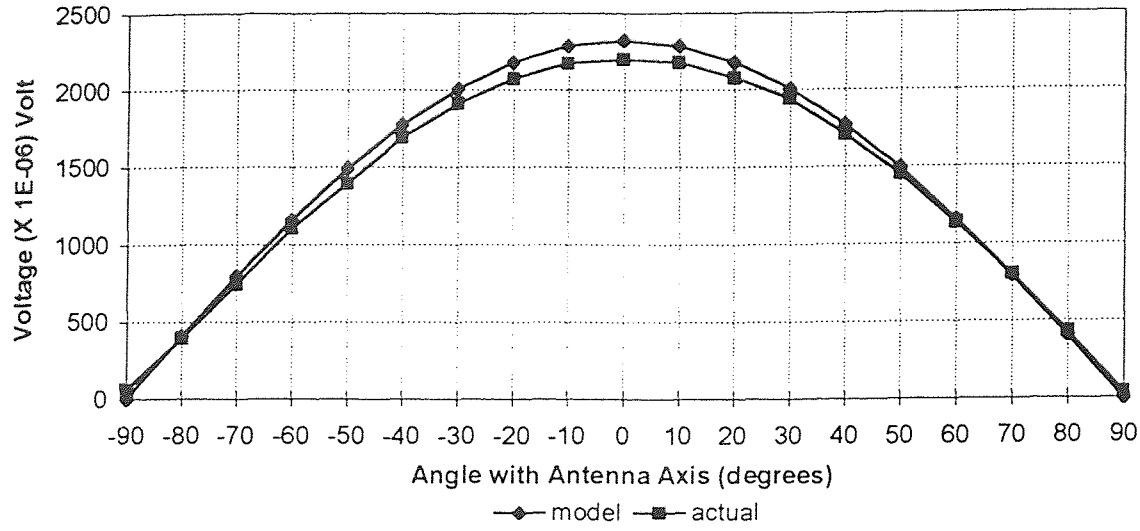

Figure 3.24 M-R (III) no 27-point correction, reference point [002]

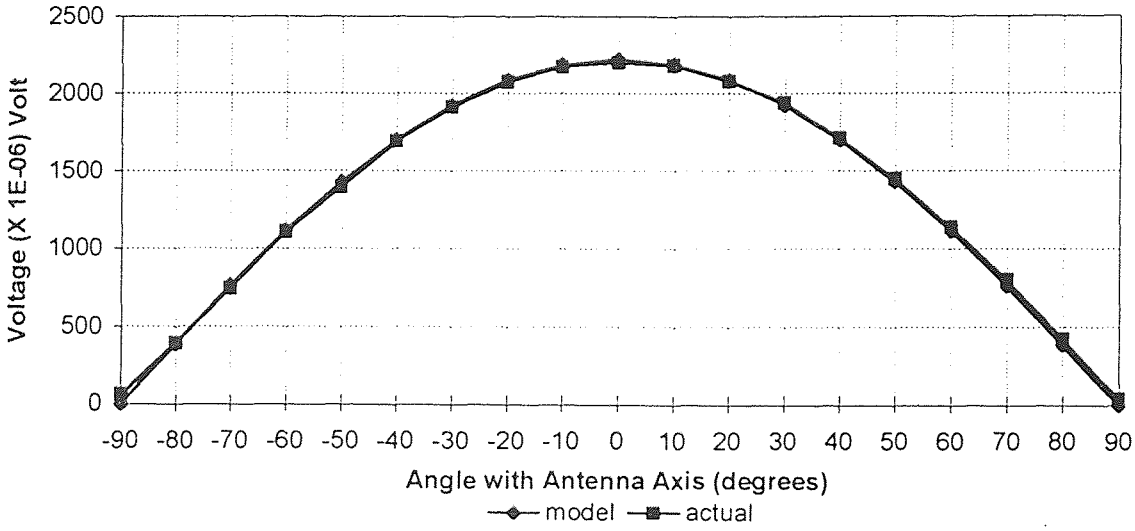

Figure 3.25 M-R (III) using 27-point correction, reference point [002]

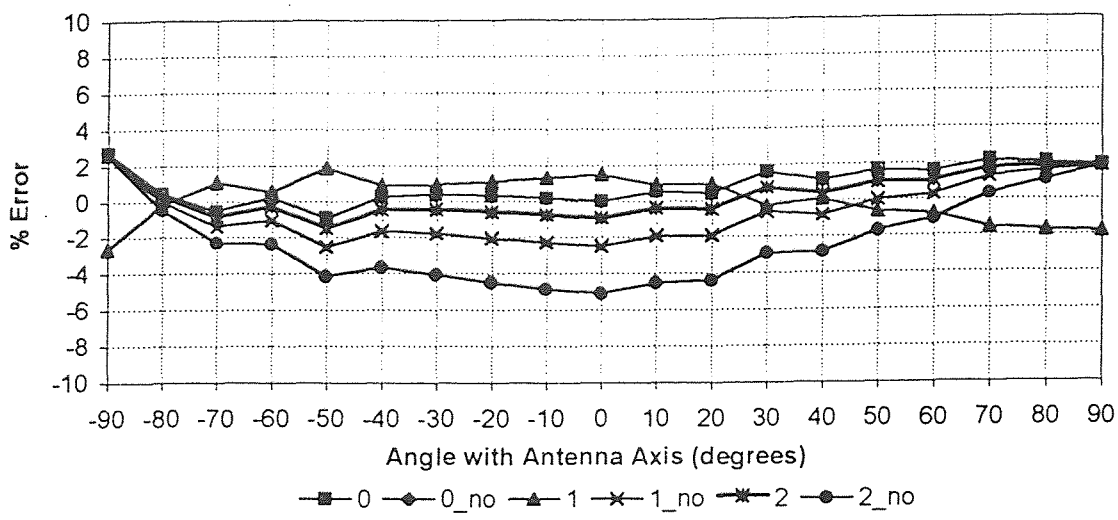

Figure 3.26 Error Plots for M-R (III)

"0", "1" and "2" stand for the cases of using 27-point correction with [000], [001] and [002] as reference points respectively. "0_no", "1_no" and "2_no" are the corresponding cases without using 27-point correction.

3.4 Conclusions of the 27-Point Study

As shown in previous sections as well as in Appendix A, the 27-point correction scheme is effective in correcting the theoretical voltages. and the theoretical voltages modified using the 27-point correction scheme effectively model the actual voltage map. The maximum errors between the theoretical and actual voltages are reduced on using the 27-point correction scheme and lie between 2% to 5% of the maximum voltage.

The error ranges obtained depend on the choice of reference point. It is observed that least errors are obtained by using either point [000] or point [002] as the reference point. The errors and error profiles obtained for both of these points are almost identical. Therefore the final selection of the reference point is based on practical considerations.

In general, for any antenna, reference point [000] lies in the plane or close to the plane of the antenna and might not be accessible easily in every experimental setup. On the other hand, point [002] lies farthest away from the antenna and is generally in the experimental space and therefore very easily accessible. Also, selection of point [002] will also lead to a reduction in the number of setups to be made for calibrating all the antennae. This is because the reference point [002] of adjacent antennae are normally common and readings for them can be taken in a single calibration setup. The number of calibration setups required for chute experiment using point [000] will be 84 (28 antennae X 3 transmitters). These are reduced to just 48 if reference point [002] is used as the reference point. For the vibrated bed experiment, the number of calibration setups can be reduced from 18 to just 4 and even the jig required for calibration can be made simple. Taking all these factors into consideration, reference point [002] is chosen as the reference point.

Thus it can be concluded that 27-point correction scheme with reference point [002] as the reference point reduces the systematic errors in the voltages by effectively modifying the theoretical voltages.

CHAPTER 4

AN EQUATION TO REPLACE THE 27-POINT SCHEME

4.1 Need for an Equation

A detailed study of the 27-point correction scheme for reducing systematic errors introduced in the tracking solution was presented in Chapter 3. The scheme is effective in minimizing the errors but it suffers from some disadvantages. The 27-point map has to be set up individually for every distinct tracking setup. This involves deciding the physical limits of the experimental space requiring correction (based on the antenna size, inter-antenna spacing and antenna configuration), and taking voltage readings at all of the 27 points of an octant of this space. This is so because the effectiveness of the 27-point scheme depends on the proper choice of the 27 points, and the accuracy with which voltage readings are taken at these points.

Also, if large antennae are used, 27 nodes may not be enough to model the non-linearity of scaling factors. In such cases a higher number of nodes may be required and the interpolation function will have to be modified accordingly. Also, the 27-point scheme is implemented for a single transmitter and the correction is assumed to be same for all three transmitters (Agrawal [9]).

In order to minimize these disadvantages, it is proposed to formulate an equation to replace the 27-point correction scheme. The proposed correction equation is the same for all systems and also eliminates the laborious task of determining the 27 points and taking accurate voltage readings for setting up the map.

4.2 The Proposed Equation

A careful study of the model-reality plots shows that the errors in the voltages depend not only on the position of the transmitter but also on its orientation. Dave [18] suggested that it could be possible to model the systematic errors by investigating the non-linear nature of the errors and by intuitively adding a small quadratic or higher order term to the voltage equation stated in Section 2.2.1. Recall that the theoretical voltage (V_{th}) induced in a receiving loop antenna by a transmitting coil is given by,

$$V_{th} = -N\omega(\vec{A} \cdot \vec{B}) \tag{4.1}$$

$$or \quad V_{th} = -N\omega A(B_x cos\alpha + B_y cos\beta + B_z cos\gamma) \tag{4.2}$$

where,

$\vec{B}$ = the resultant magnetic flux density

$\vec{A}$ = the area vector of the transmitting coil

N = number of turns in the transmitting coil

ω = 2π times the frequency of oscillation

$cos\alpha$, $cos\beta$, $cos\gamma$ = direction cosines of transmitter axis in antenna coordinate system

This voltage model assumes that the field of the transmitter is perfectly symmetrical, and the amplifier and data acquisition boards are perfectly linear. It also assumes that the principle of reciprocity is valid throughout the experimental space. As a consequence, the theoretical voltage map obtained using this model is symmetrical over the antenna while in practice this is not the case. The systematic errors in voltages can be

compensated by adding a correction factor V_c to the theoretical voltage V_{th}. Then, the new compensated model voltage V will be given by,

$$V = V_{th} + V_c \tag{4.3}$$

where V_c is the correction added to the theoretical voltage.

The objective here is to find this correction factor V_c. There are two approaches to this problem: analytical and intuitive. The analytical approach involves an in depth mathematical analysis of the voltage model and derivation of higher order terms by techniques such as Taylor series expansion or from the physics of the problem. The coefficients can then be determined by minimization of errors from a large set of experimental data points. In the intuitive approach adopted here, experience and insight in using the voltage model is employed to analyze various model-reality voltage plots and suggest intuitively an equation correction. Three types of model-reality plots (explained in Section 3.3) are used for this purpose.

It was observed that the correction equation appears to require quadratic or higher order terms. Therefore, various equations with quadratic, cubic and higher order terms were developed and corresponding model-reality plots were generated. After a careful study of all the model-reality plots, equation (4.4) was selected as the correction equation. Since N ω and A are constant for a given transmitter, the term ($-N\omega A$) can be combined into a single constant k. Then the correction equation is given by,

$$V_c = -0.15\,k \begin{bmatrix} \left(B_x^2 \cos^2\alpha + B_y^2 \cos^2\beta + B_z^2 \cos^2\gamma\right) \\ +0.01\left(B_x^3 \cos^3\alpha + B_y^3 \cos^3\beta + B_z^3 \cos^3\gamma\right) \end{bmatrix} \tag{4.4}$$

Effectively, the equation (4.4) adds a 15% quadratic and a 0.15% cubic behavior to the theoretical voltage to give the model voltage.

4.3 Testing of the Equation

In order to test the correction V_c, experiments are conducted in all the three setups - the model-chute, inclined chute and vibrated bed. The data collected is processed using the 27-point correction scheme (with point [002] as the reference point), and then by using the correction equation. The results are presented in the following pages.

Figures 4.1 to 4.3 are obtained for the model-chute setup. The data used for these plots is the same as that used for generating the model-reality plots in Section 3.3. Here an additional series representing voltages obtained after implementing the correction equation is also presented alongside the series for actual voltages and theoretical voltages after applying the 27-point correction (with point [002] as the reference point). An additional set of plots using the data of model-reality plots in Appendix A is presented in Appendix B. The nomenclature for the figures is same as that in Chapter 3.

It is observed that the series for voltage with 27-point correction and the series for voltage with equation correction are almost identical. Hence, it can be said that the corrections added by the correction equation are in good agreement with those added by the 27-point correction scheme.

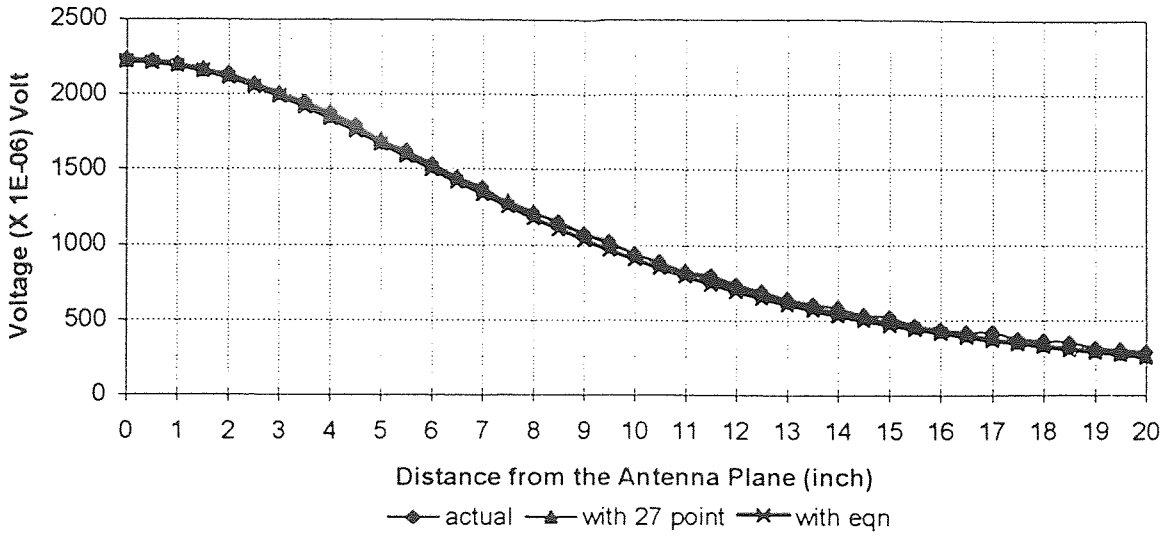

Figure 4.1 M-R (I) using equation correction
(Using data of Figure 3.9)

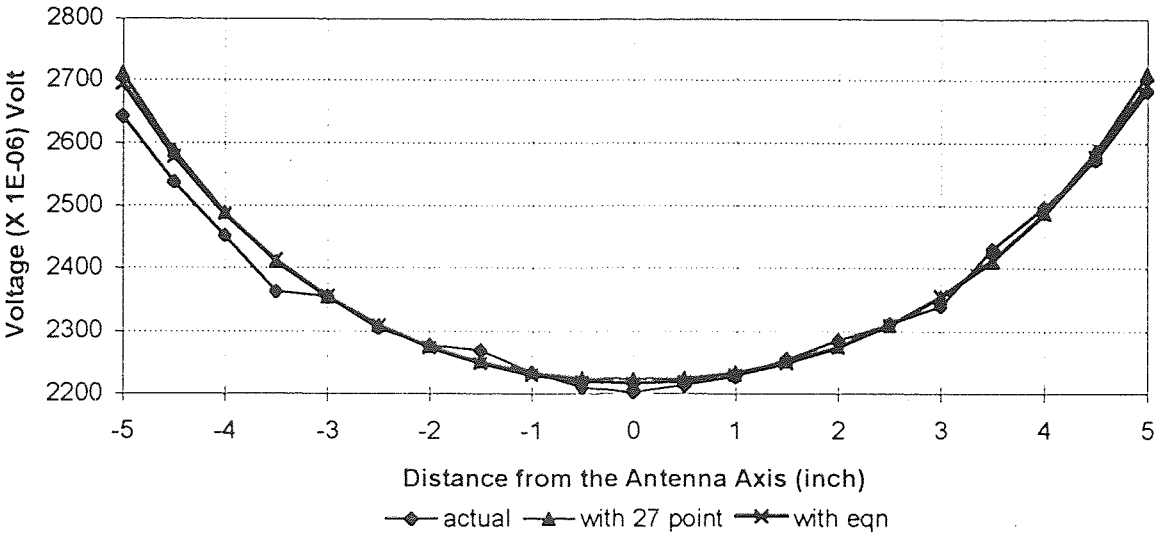

Figure 4.2 M-R (II) using equation correction
(Using data of Figure 3.17)

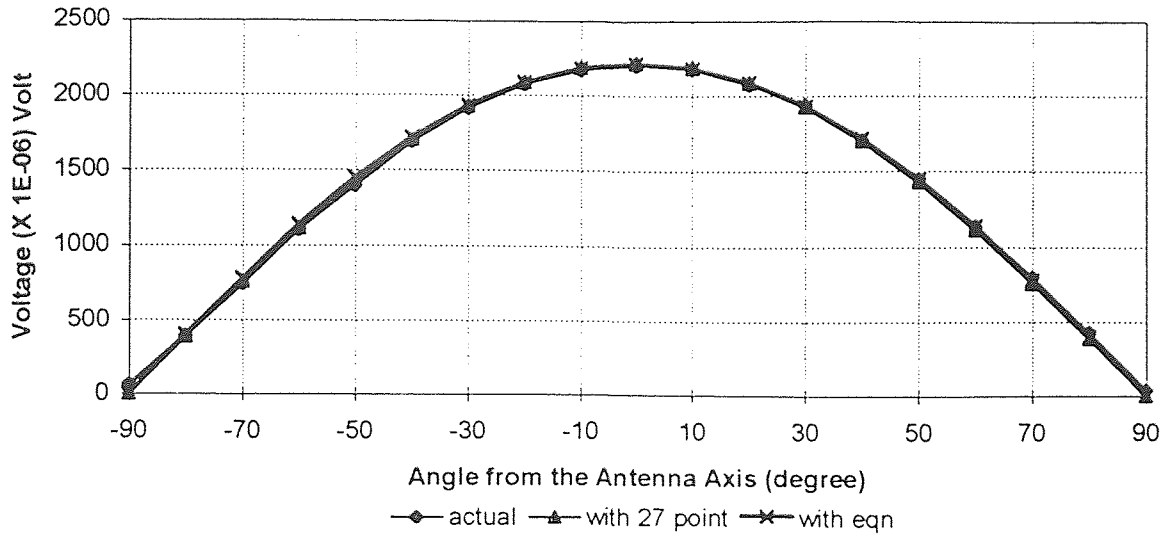

Figure 4.3 M-R (III) using equation correction

(Using data of Figure 3.25)

Figures 4.4 through 4.15 are obtained from the data collected from the top half of inclined chute. The global x, y and z coordinates of the transmitting sphere remain constant at (x = 41", y = 12", z = 15") and there is no rotation about x-axis i.e.($\alpha = 0^{\circ}$). The sphere is then rotated first about the global z-axis (γ) and then about the global y-axis (β). The data thus gathered is processed in two ways to predict the trajectory, that is, with the 27-point correction scheme and with the correction equation. Both sets of results have been presented here. The results shown in Figures 4.4 to 4.9 are obtained using the 27-point correction scheme (i.e. without using the equation correction) while those shown in Figures 4.10 to 4.15 are obtained using the correction equation. The maximum and mean errors in the results as well as the standard deviations are given below each plot.

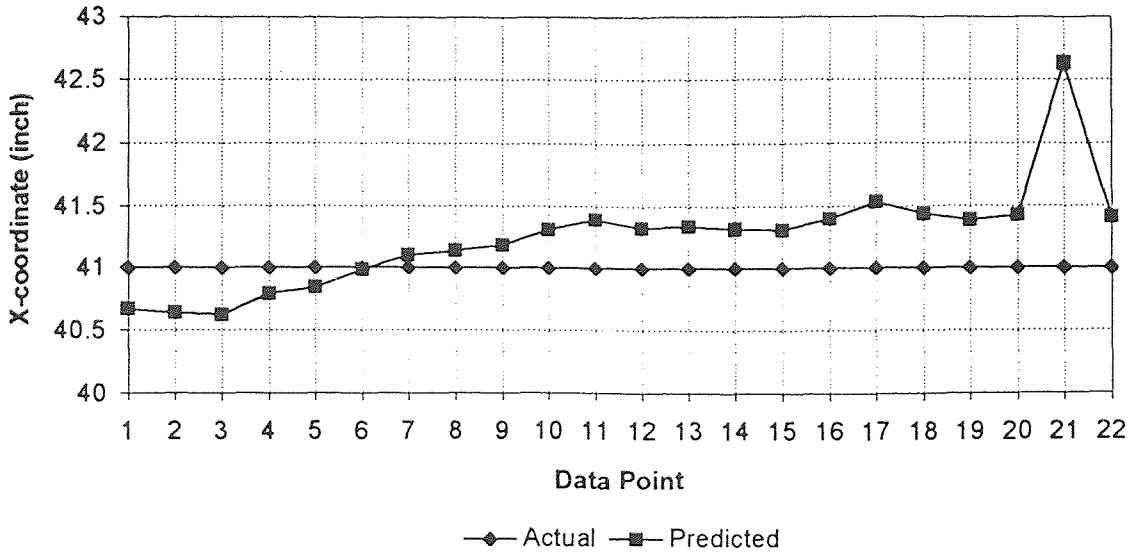

Figure 4.4 X plot, without correction equation
(maximum error = 1.63", mean error = 0.36", standard deviation = 0.30")

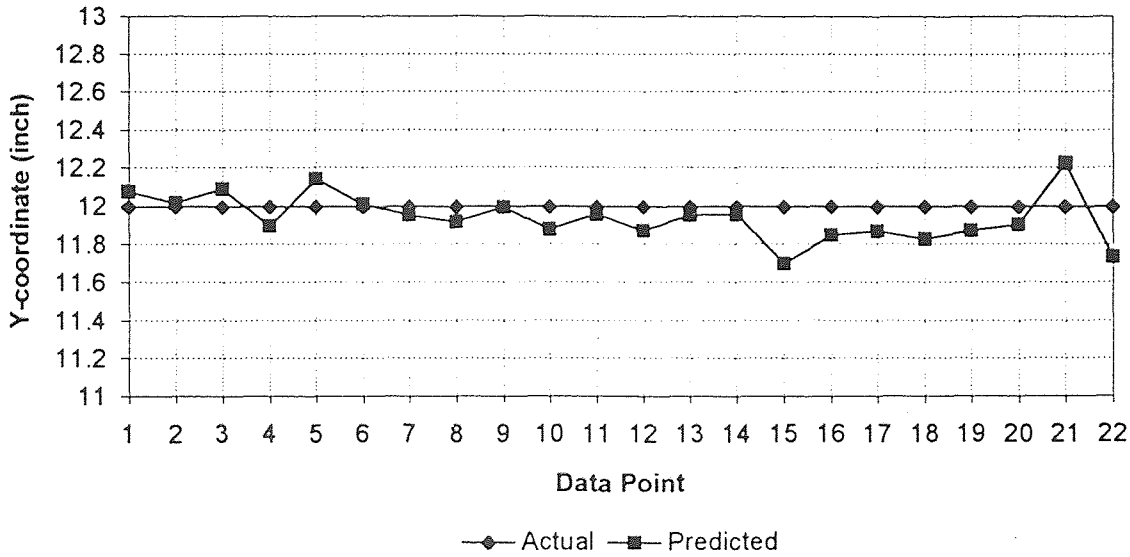

Figure 4.5 Y plot, without correction equation
(maximum error = 0.30", mean error = 0.11", standard deviation = 0.07")

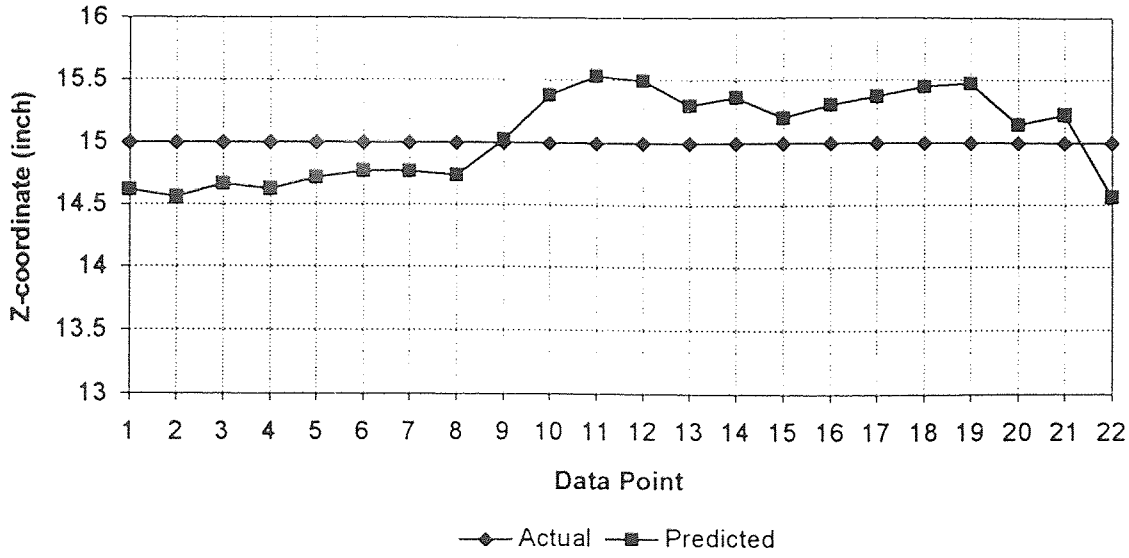

Figure 4.6 Z plot, without correction equation
(maximum error = 0.53", mean error = 0.32", standard deviation = 0.12")

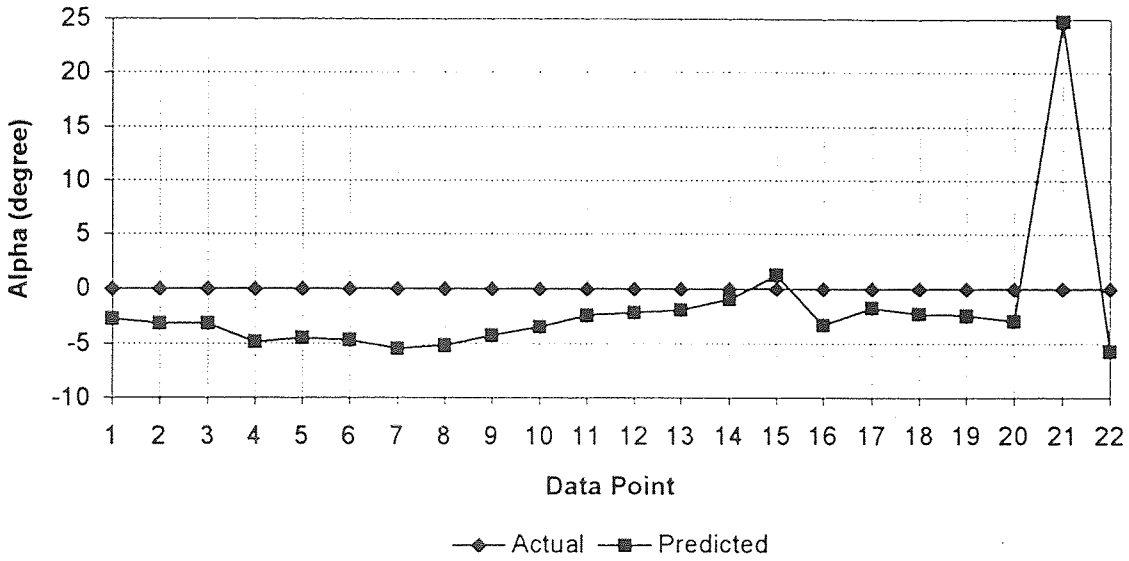

Figure 4.7 α plot, without correction equation
(maximum error = 24.84°, mean error = 4.24°, standard deviation = 4.69°)

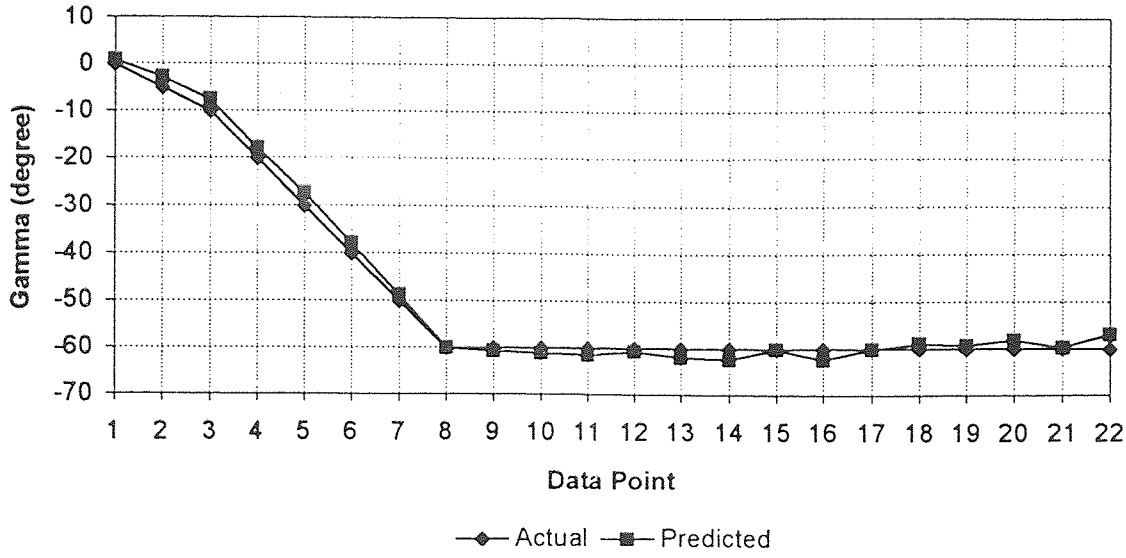

Figure 4.8 γ plot, without correction equation
(maximum error = 3.02°, mean error = 1.44°, standard deviation = 0.88°)

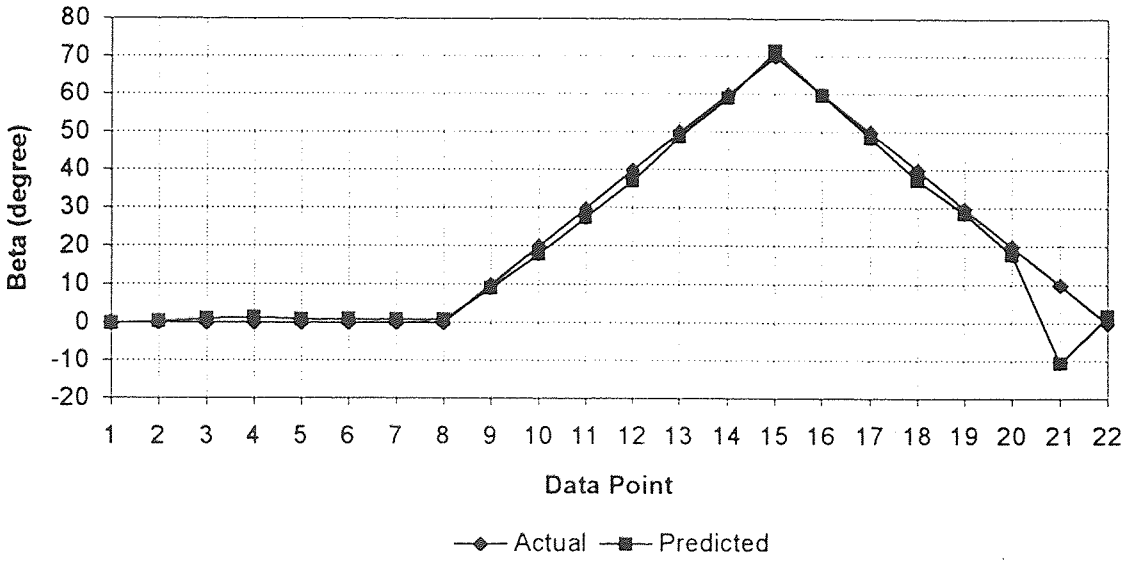

Figure 4.9 β plot, without correction equation
(maximum error = 20.48°, mean error = 2.18°, standard deviation = 4.06°)

A sudden glitch is observed in the plots for x, y, α and β at data point 21 even when 27-point correction is used. Such glitches were also observed previously by Agrawal [9]. These could be due to asymmetry of the voltage map or an anomaly in the 27-point map. When the correction equation is used instead of the 27-point correction scheme, the glitch is no longer observed in any of the plots. The results obtained at other points are the same as (or better than) those obtained using the 27-point correction scheme. This implies that the correction equation is able to model the errors in the voltage map more accurately than the 27-point scheme. The results obtained by using the correction equation are presented in Figures 4.10 to 4.15.

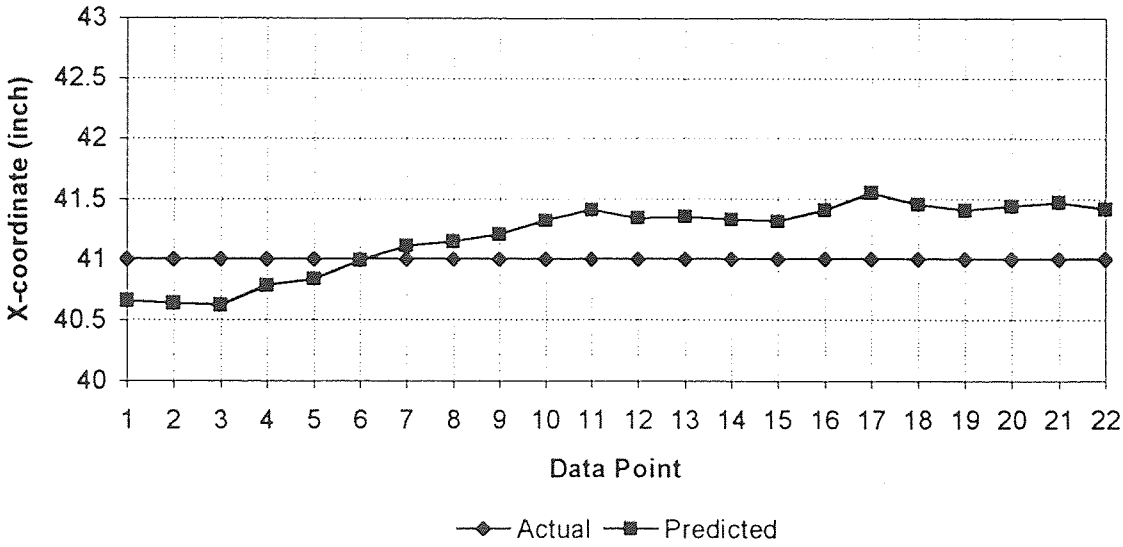

Figure 4.10 X plot, using correction equation
(maximum error = 0.55", mean error = 0.32", standard deviation = 0.12")

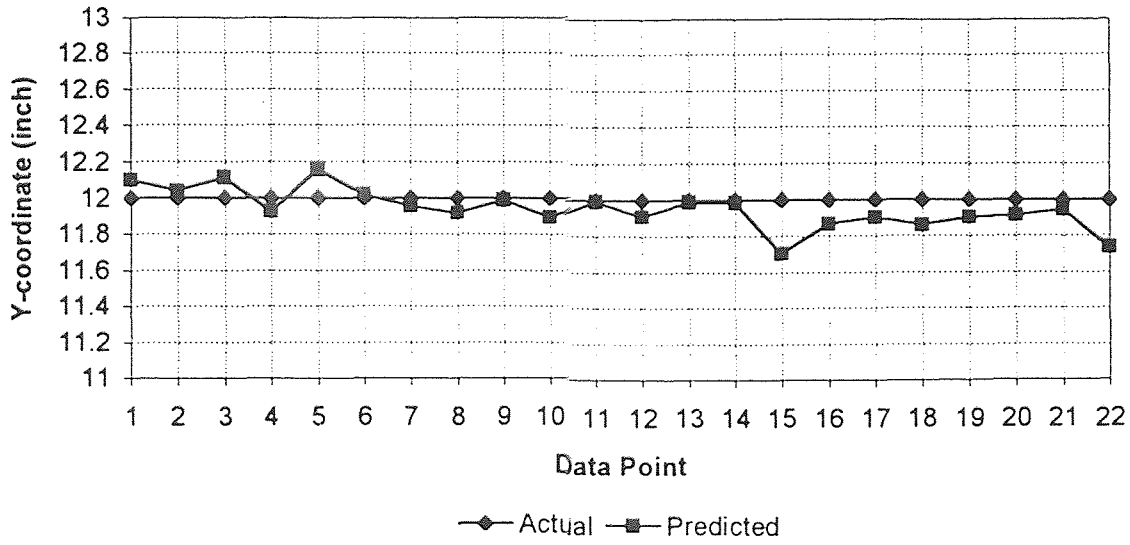

Figure 4.11 Y plot, using correction equation
(maximum error = 0.29", mean error = 0.09", standard deviation = 0.07")

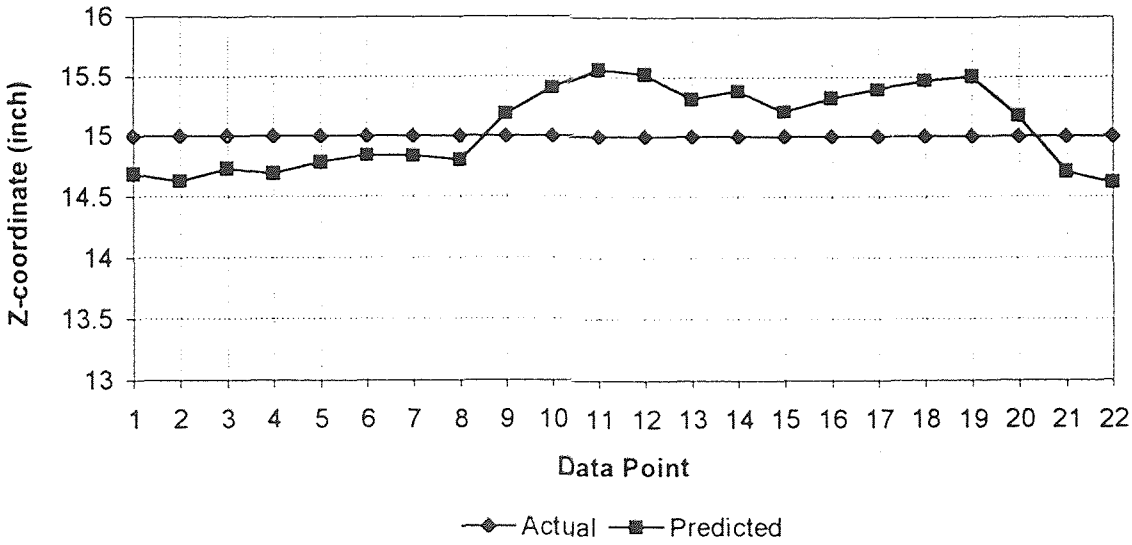

Figure 4.12 Z plot, using correction equation
(maximum error = 0.56", mean error = 0.32", standard deviation = 0.11")

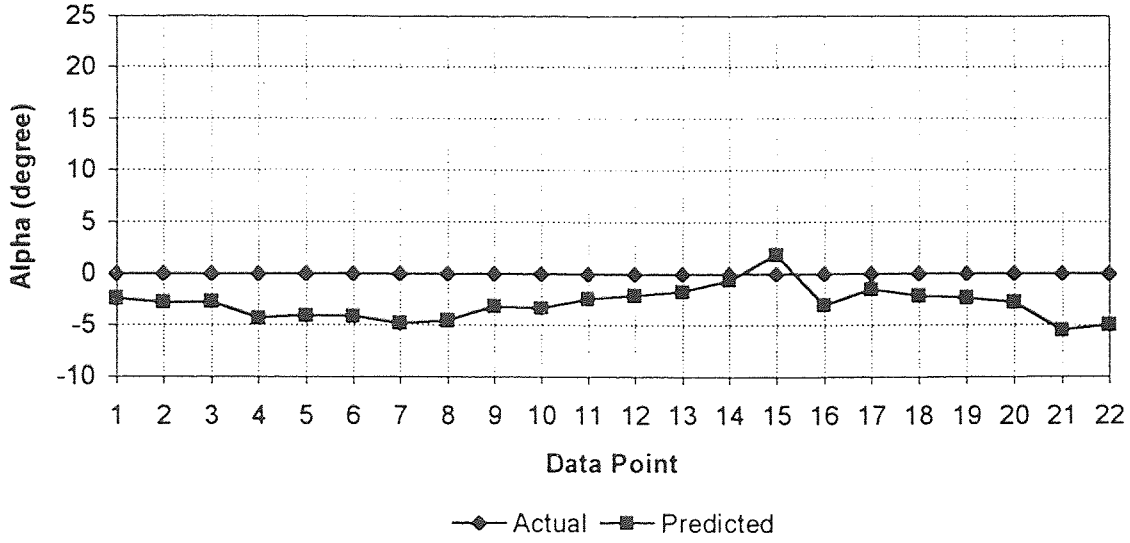

Figure 4.13 α plot, using correction equation
(maximum error = 5.50°, mean error = 3.06°, standard deviation = 1.24°)

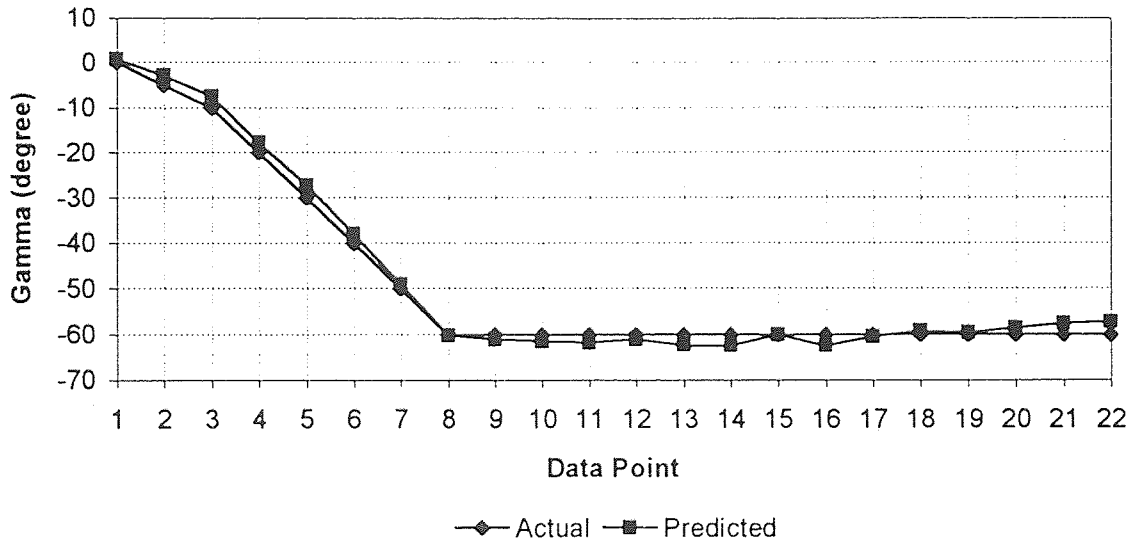

Figure 4.14 γ plot, using correction equation
(maximum error = 2.83°, mean error = 1.47°, standard deviation = 0.88°)

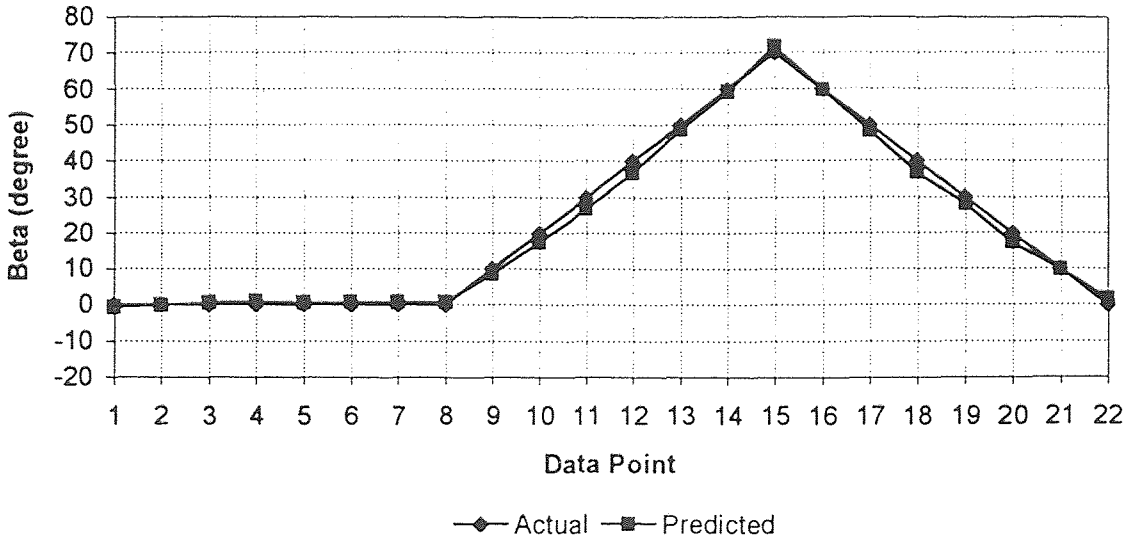

Figure 4.15 β plot, using correction equation
(maximum error = 3.18°, mean error = 1.38°, standard deviation = 0.96°)

The model-reality plots for the vibrated bed setup are shown in Figures 4.17 and 4.18. The trajectory for both the plots is similar in nature. The z-axis of the antenna (in antenna coordinate system) and the axis of the transmitter are kept coincident and the distance between the transmitter and the antenna is increased as shown in Figure 4.16.

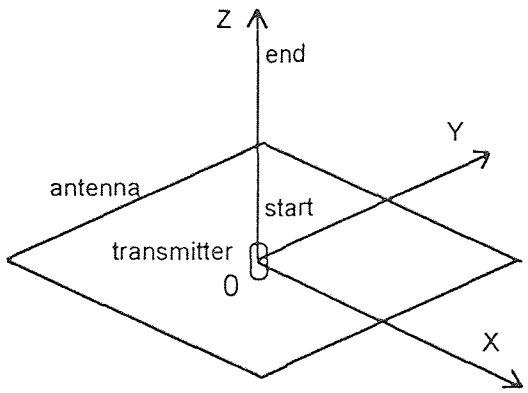

Figure 4.16 Trajectory for vibrated bed model-reality plots

Figure 4.17 is the model reality plot for the antenna of size 6"X6". Here the distance between the transmitter and antenna is increased from 1.5" to 8.5" at 0.5" increments.

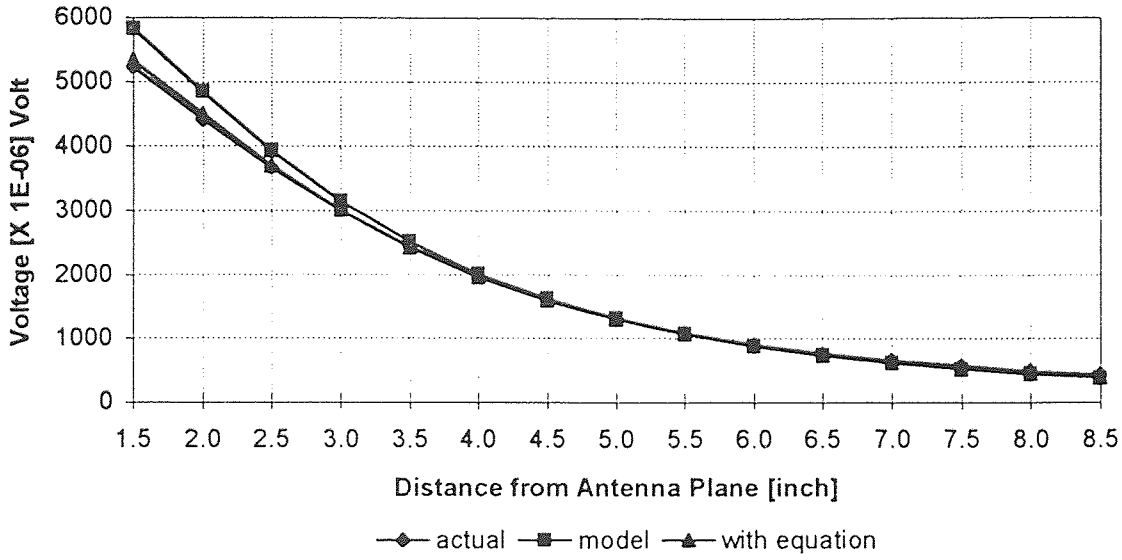

Figure 4.17 Model-Reality plot for vibrated bed: 6"X6" antenna

Figure 4.18 is the model reality plot for the antenna of size 6"X10". Here the distance between the transmitter and antenna is increased from 1.5" to 8.5" at 0.5" increments.

Due to small size of the vibrated bed experimental setup, it is extremely difficult to take voltage reading for setting up the 27-point correction scheme. It is observed that there is a very good agreement between the theoretical and the actual voltages throughout the usable extent of the antenna. There is a deviation of model voltages from the actual voltages near the antenna plane. This could be because near the plane of the antenna, the

area of the transmitting loop is not negligible compared to that of the antenna. This results in the principle of reciprocity becoming invalid near the antenna plane. These deviations are minimized (almost eliminated) when the correction equation is used to modify the theoretical voltages.

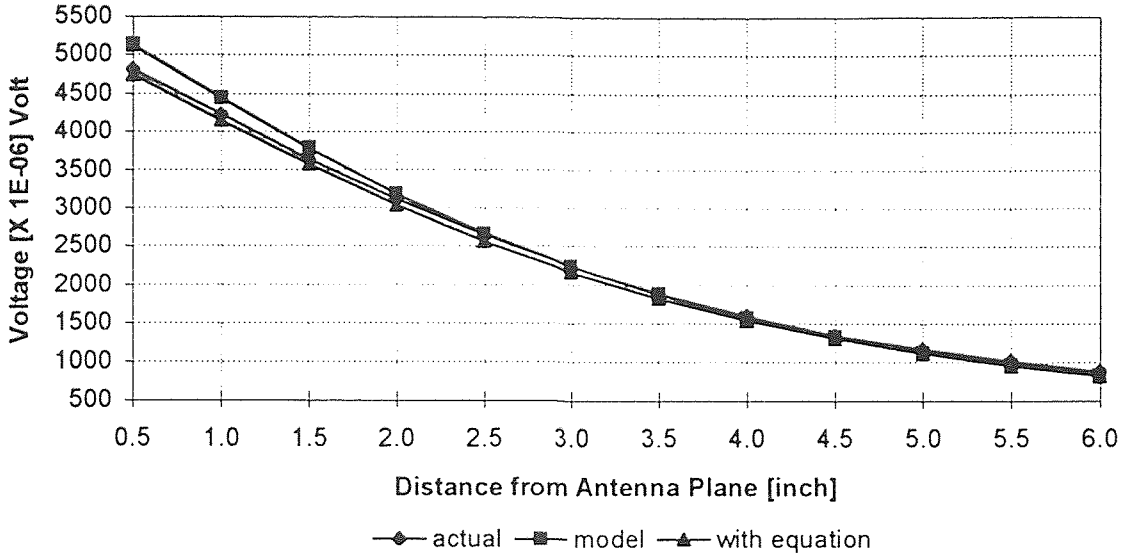

Figure 4.18 Model-Reality plot for vibrated bed: 6"X10" antenna

From all the above plots it can be concluded that the correction equation is an accurate modeling of the systematic errors and provides a better alternative to the 27-point scheme. The correction equation can also be used to correct the theoretical voltage in cases such as vibration cell, where it is extremely difficult to accurately setup the 27-point scheme.

CHAPTER 5

MULTIPLE SOLUTIONS IN ORIENTATIONS

Sometimes it is observed that the results obtained are correct in positions but not in angles. A careful analysis of such solutions reveals that in most of the cases although the angles are very different, they have almost same direction cosines. Such solutions are called "multiple solutions in orientations".

The forward model predicts theoretical voltages based on the direction cosines of transmitter axis in antenna coordinate system. The direction cosines are functions of α, β and γ, however, a given set of direction cosines does not correspond to a unique set of angles (α, β, γ). In other words, in certain cases, different sets of angles (α, β, γ) can result in almost equal direction cosines values and hence almost equal theoretical voltages. Hence, the "multiple solutions in orientations" are the angular solutions that are apparently very different from the actual solution but have almost the same direction cosines as the correct solution.

In this chapter two techniques for minimizing the multiple solutions in orientations are presented. Section 5.1 discusses a solution re-extraction scheme while Section 5.2 presents a different representation of angles called equivalent angle-axis representation.

5.1 Solution Re-extraction

A majority of the multiple solutions in orientations are of the type mentioned by Agrawal [9] and reproduced in Table 5.1. It is observed from the table that the predicted angles differ by multiples of 90°. For example, the predicted $\alpha = 247^\circ$ is approximately the actual $\alpha = 70^\circ + 2(90^\circ)$, predicted $\beta = 196^\circ$ is approximately the actual $\beta = 6(90^\circ) - 345^\circ$.

Though it is possible to correct all the multiple solutions in orientations by examining each solution, no generic equation is found for eliminating these multiple solutions. Hence, the source of the multiple solutions, i.e. the solution algorithm is closely examined.

Table 5.1 Multiple solutions in orientations (Agrawal [9])

Actual (degree)						Predicted (degree)					
X	Y	Z	α	β	γ	X	Y	Z	α	β	γ
6.3	2.8	6.4	0	345	30	6.1	3.2	6.5	174	193	211
12.3	6.0	8.1	70	345	30	12.1	6.1	7.9	247	196	213
14.0	7.0	8.6	90	345	30	13.8	6.7	8.2	267	197	212
14.8	7.5	8.8	100	345	30	15.3	7.8	8.9	260	16	208

The backward solution algorithm employs a perturbation technique for calculating the positions and orientations from the voltages. This involves individually perturbing each of the unknowns x, y, z, α, β and γ about initial guesses to converge to a solution where the residuals are minimum as discussed in Section 2.2. Due to the random nature of the perturbation technique and periodicity of trigonometric functions, often the algorithm converges to an angular solution that is different from the expected solution but has the same direction cosines.

A solution re-extraction scheme is developed and used to map these solutions into the interval [-180°, 180°] for post-processing and better visualization of results. The solution given by the backward algorithm is used to calculate the global to transmitter transformation matrix, T given by equation (5.1). A simple and easy to use representation of the transformation matrix T is given by equation (5.2).

$$T = \begin{bmatrix} \cos\beta\cos\gamma & \sin\alpha\sin\beta\cos\gamma - \cos\alpha\sin\gamma & \cos\alpha\sin\beta\cos\gamma + \sin\alpha\sin\gamma \\ \cos\beta\sin\gamma & \sin\alpha\sin\beta\sin\gamma + \cos\alpha\cos\gamma & \sin\gamma \\ -\sin\beta & \sin\alpha\cos\beta & \cos\alpha\cos\beta \end{bmatrix} \quad (5.1)$$

$$T = \begin{bmatrix} n_x & o_x & a_x \\ n_y & o_y & a_y \\ n_z & o_z & a_z \end{bmatrix} \quad (5.2)$$

The angles can be re-extracted from this matrix using the *atan2(sin, cos)* function as shown in equations (5.3), (5.4) and (5.5). Since the *atan2* function takes both the sine and the cosine of the angle as its arguments, information about the sign of the angle is preserved and a unique value in the interval [-180°, 180°] is found.

$$\alpha = atan2(o_z, a_z) \quad (5.3)$$

$$\beta = atan2\left(-n_z, \sqrt{n_x^2 + n_y^2}\right) \quad (5.4)$$

$$\gamma = atan2(n_y, n_x) \quad (5.5)$$

Results obtained after re-extracting the actual and the predicted angles shown in Table 5.1 are presented in Table 5.2. The results, except for the last one, no longer exhibit multiple solutions in orientations.

Table 5.2 Table 5.1 after solution re-extraction

Actual (degree)						Predicted (degree)					
X	Y	Z	α	β	γ	X	Y	Z	α	β	γ
6.3	2.8	6.4	0	-15	30	6.1	3.2	6.5	-6	-13	31
12.3	6.0	8.1	70	-15	30	12.1	6.1	7.9	67	-16	33
14.0	7.0	8.6	90	-15	30	13.8	6.7	8.2	87	-17	32
14.8	7.5	8.8	100	-15	30	15.3	7.8	8.9	-100	16	-152

The solution re-extraction process results in a marked improvement in visualization of results that is evident from Figures 5.1 and 5.2. Both of these plots are for the same experiment. The transmitting sphere was allowed to roll down an inclined plane with the rotation taking place about the y-axis. Only the parameter under consideration i.e. the rotation β is shown here.

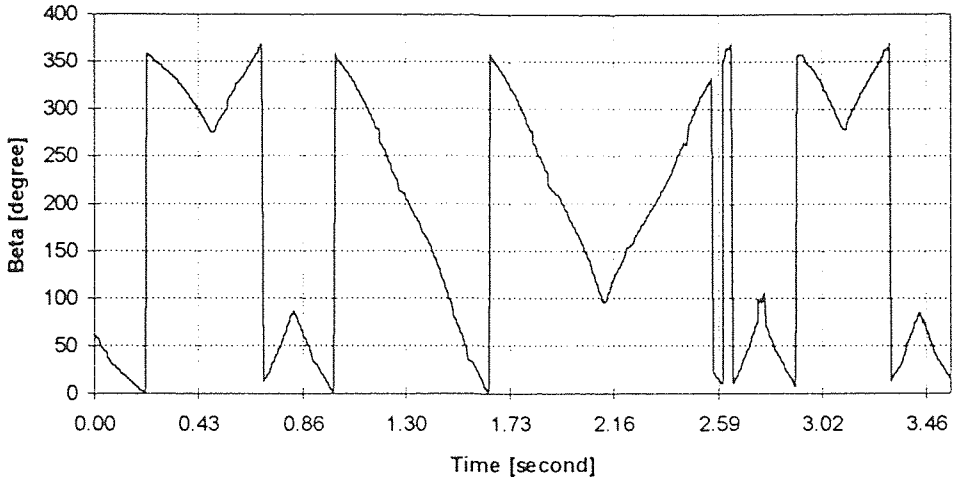

Figure 5.1 Rotation β before solution re-extraction

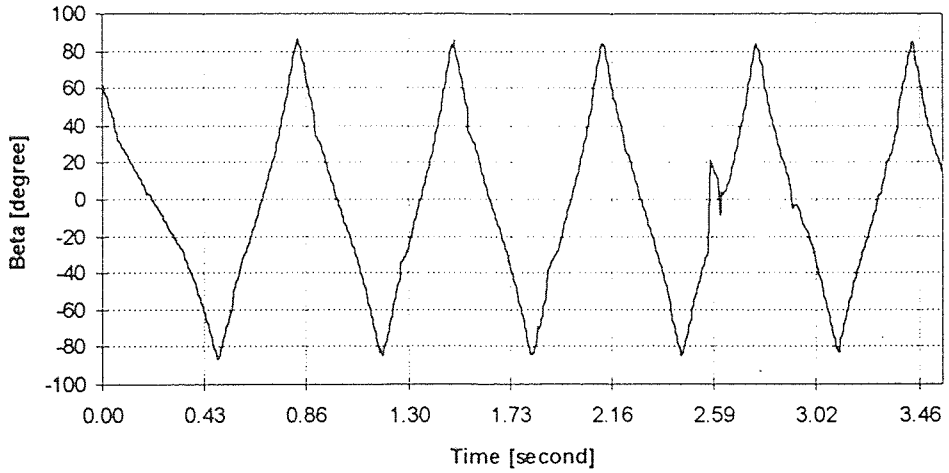

Figure 5.2 Rotation β after solution re-extraction

5.2 Equivalent Angle-Axis Representation

There are various methods of representing rotations in three dimensions. We have adopted the Roll-Pitch-Yaw or RPY convention as explained by Paul [11] for calculating the rotations. According to the RPY convention, the first rotation α is about the x-axis, followed by a rotation β about y-axis and then a rotation γ about the z-axis.

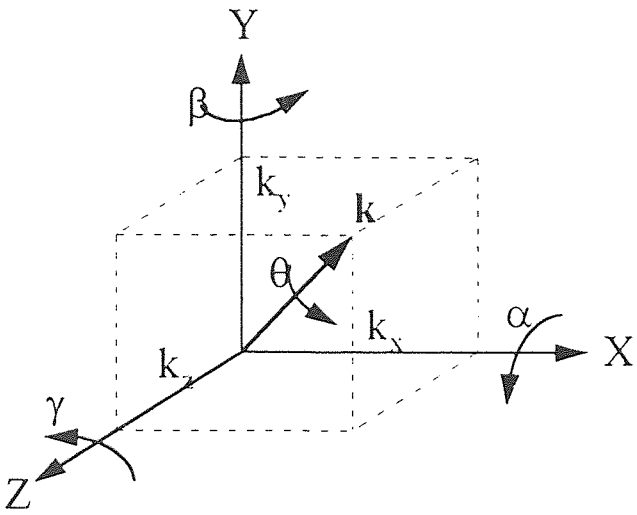

Figure 5.3 The equivalent angle-axis representation

In this section another representation of rotations, the equivalent angle-axis representation as explained by Craig [19] and Paul [11] is introduced. Using this convention, it is possible to represent any angular transformation as a rotation about an equivalent axis. Thus the rotations α about x-axis, β about y-axis and γ about z-axis can be converted to an equivalent rotation θ about an axis $\hat{k}$ with unit vectors k_x, k_y and k_z as shown in Figure 5.3. The corresponding transformation matrix is given by equation (5.6). The procedure for converting the angles α, β and γ into an equivalent rotation θ about an axis with unit vectors k_x, k_y, k_z is detailed in Appendix C.

$$T = \begin{bmatrix} k_x k_x(1-\cos\theta)+\cos\theta & k_y k_x(1-\cos\theta)-k_z\sin\theta & k_z k_x(1-\cos\theta)+k_y\sin\theta \\ k_x k_y(1-\cos\theta)+k_z\sin\theta & k_y k_y(1-\cos\theta)+\cos\theta & k_z k_y(1-\cos\theta)-k_x\sin\theta \\ k_x k_z(1-\cos\theta)-k_y\sin\theta & k_y k_z(1-\cos\theta)+k_x\sin\theta & k_z k_z(1-\cos\theta)+\cos\theta \end{bmatrix} \quad (5.6)$$

The equivalent angle-axis representation is helpful in visualizing the results and also converts orientation data into a form that is more helpful for generating animations from the obtained results.

An interesting application of this representation is to check whether the errors in the orientations even after solution re-extraction are in fact multiple solutions. This is demonstrated by the series of plots, Figures 5.4 through 5.13. This experiment was conducted in the vibrated bed setup using the calibration jig by moving the transmitter in x direction, keeping y, z, α, β and γ fixed. Figures 5.4 through 5.9 are the results obtained from this *straight run* experiment.

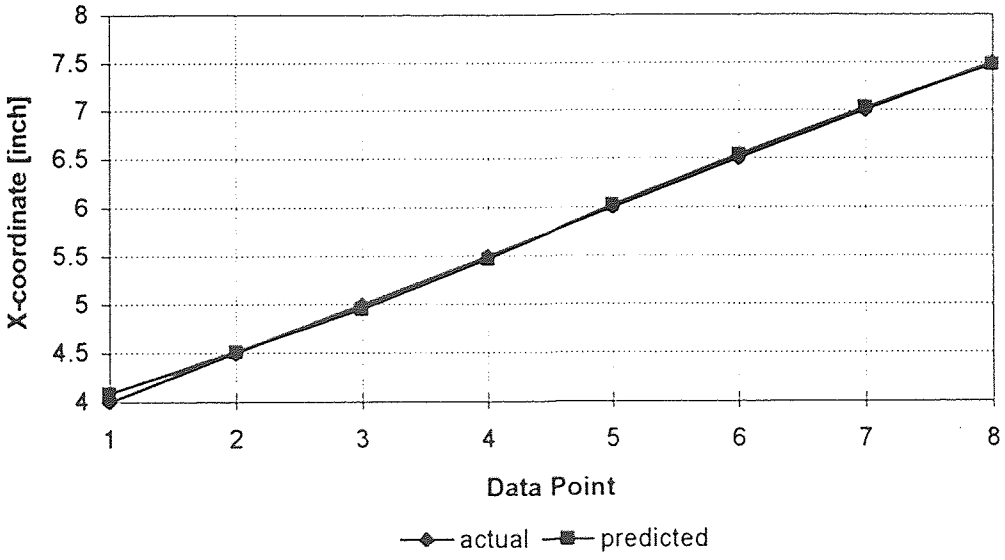

Figure 5.4 Straight run: X plot

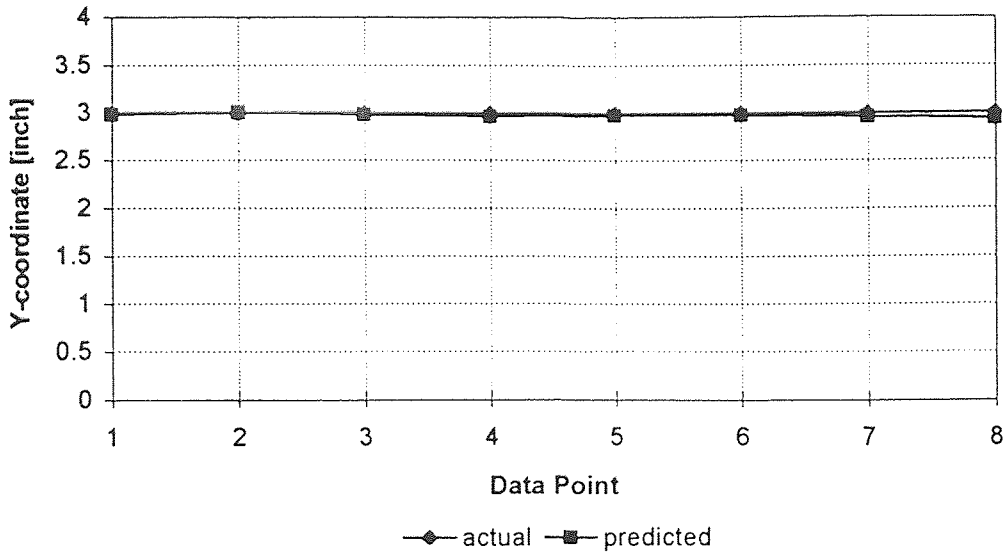

Figure 5.5 Straight run: Y plot

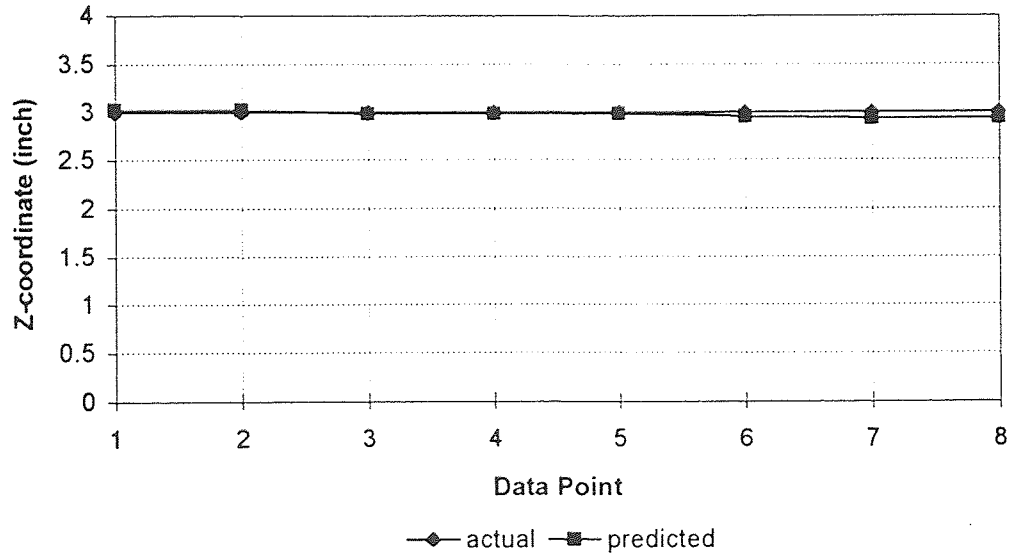

Figure 5.6 Straight run: Z plot

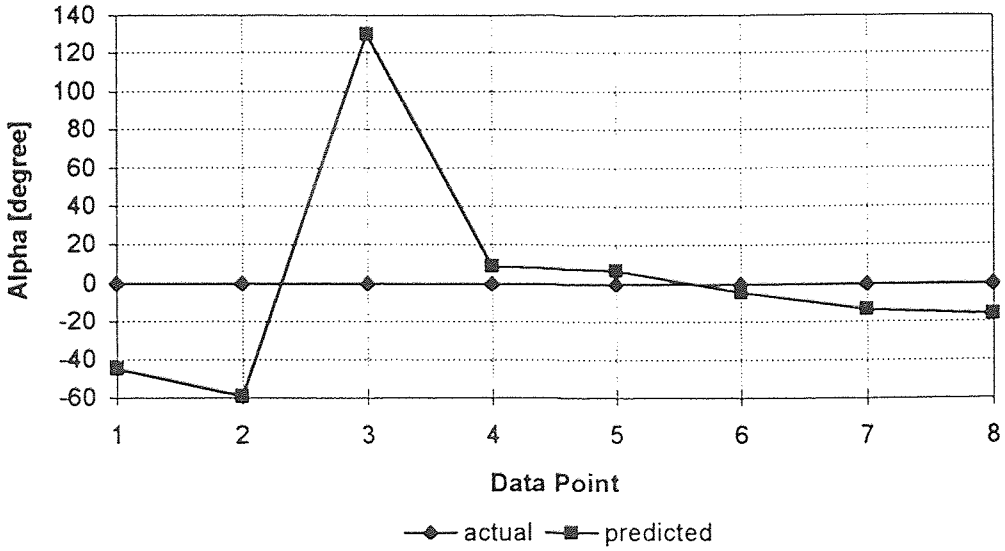

Figure 5.7 Straight run: α plot

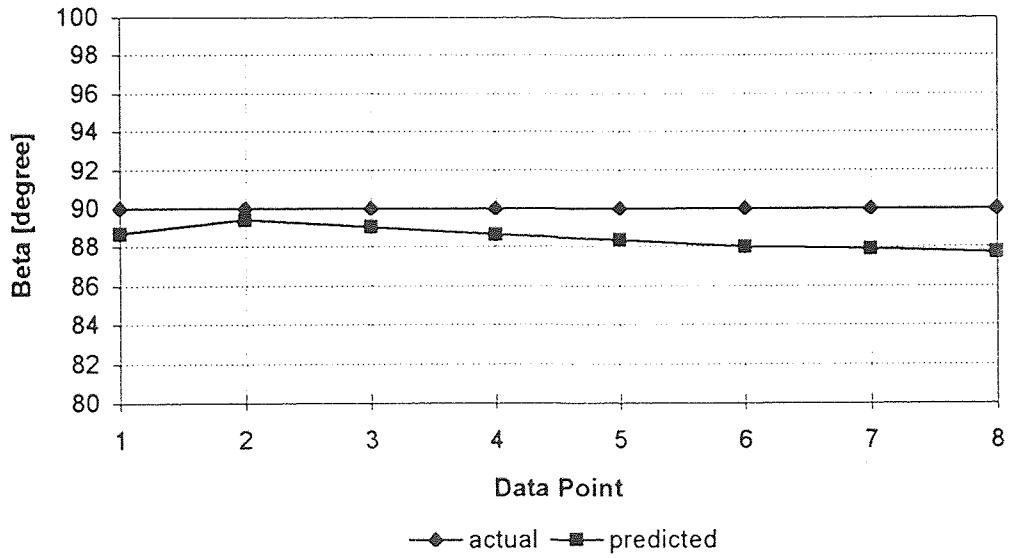

Figure 5.8 Straight run: β plot

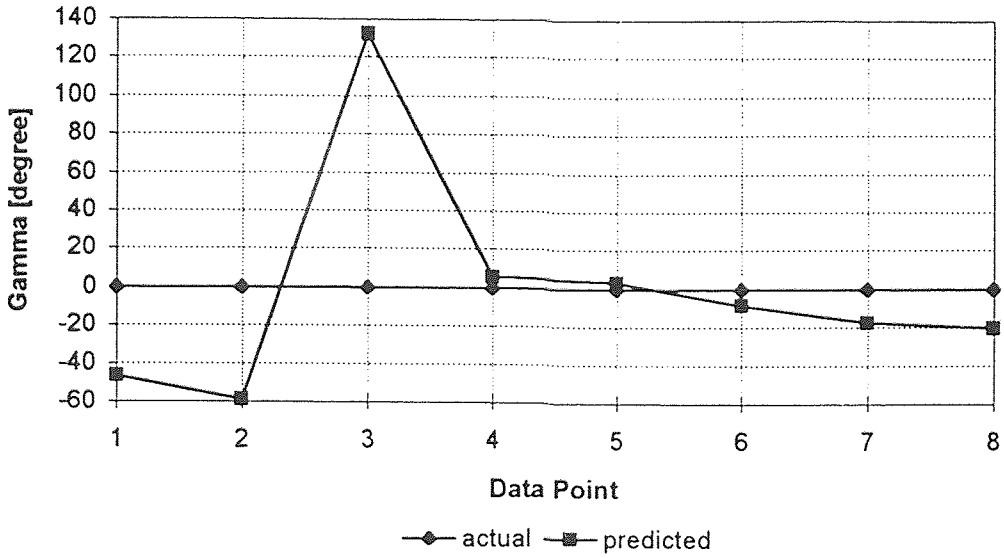

Figure 5.9 Straight run: γ plot

There is a very good agreement between the actual and predicted values of x, y, z and β, but very large errors are seen in α and γ. These surprisingly large errors in α and γ are similar in nature and magnitude and hence they might be interdependent.

When the angles are converted to the equivalent angle-axis representation, no such large errors are observed in either the axis or the equivalent angle of rotation as seen in Figures 5.10 to 5.13. This indicates that the errors in α and γ are certainly a case of multiple solution in orientations. Though the equivalent angle-axis representation of angles proves that these errors were a case of multiple solutions, the nature and cause of these multiple solutions is not very well understood.

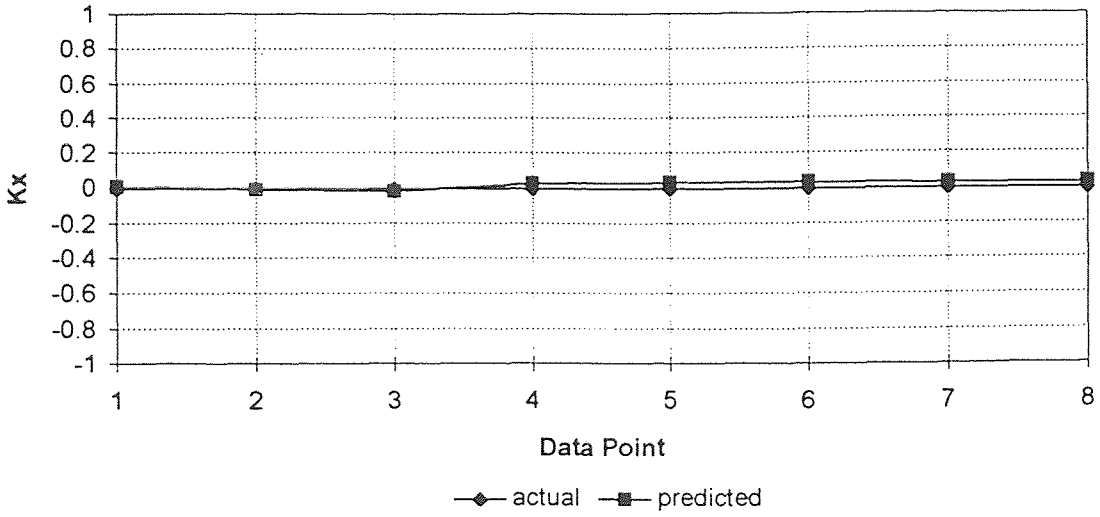

Figure 5.10 Straight run: k_x plot

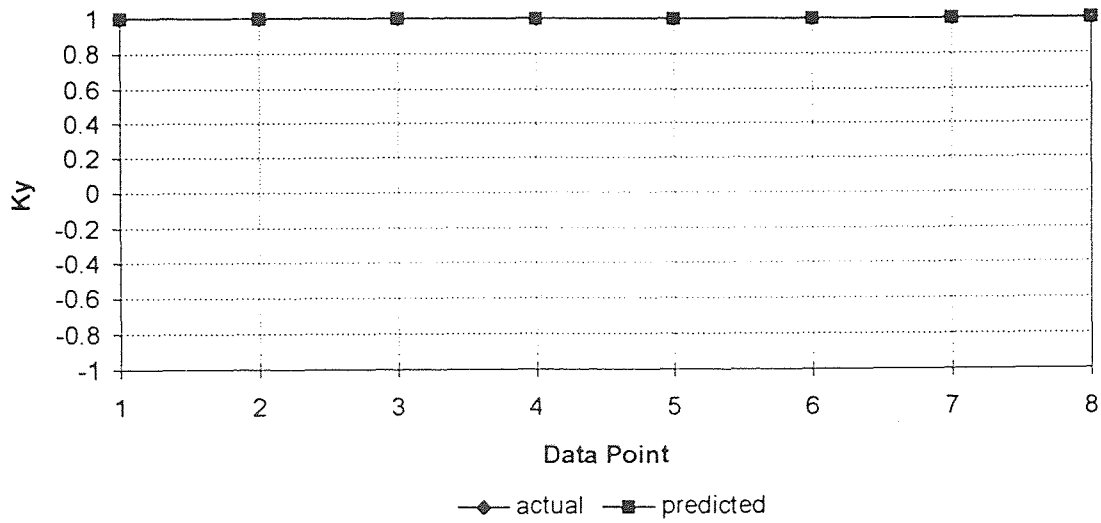

Figure 5.11 Straight run: k_y plot

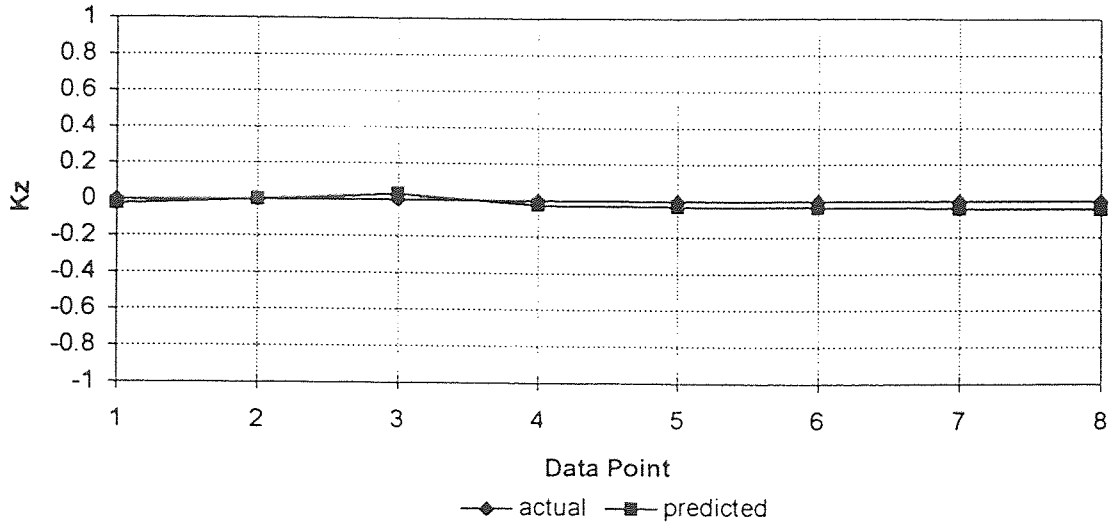

Figure 5.12 Straight run: k_z plot

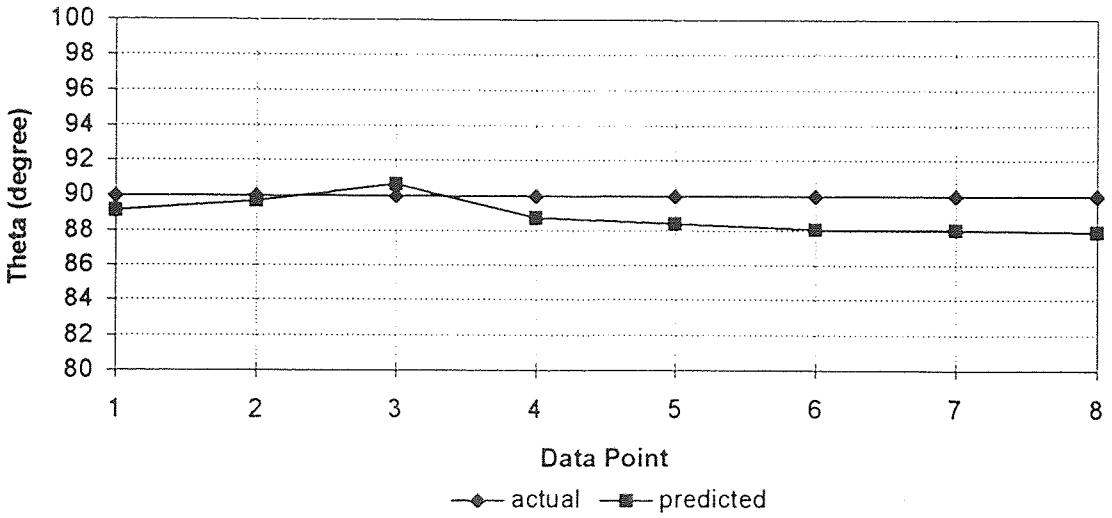

Figure 5.13 Straight run: θ plot

Thus, the solution re-extraction process and the equivalent angle-axis representation scheme demonstrated in this chapter are successfully able to eliminate a large number of multiple solutions in orientations.

CHAPTER 6

EXPERIMENTAL RESULTS

The particle tracking system has been applied to the study of one model and two experimental setups. In this chapter, some results obtained from the vibrated bed and the inclined chute are presented. Results of a free fall test carried out in the model-chute are presented in Section 6.1. Section 6.2 shows some vibrated bed results while Section 6.3 presents the inclined chute results.

6.1 Free Fall Test

In order to check the performance of the data acquisition system with fast data acquisition a controlled trajectory is used where the tracking sphere is allowed to fall freely from rest. The objective of this "free fall test" is to check:

- The real time data acquisition capability of the DAS.
- The accuracy of the DAS.

In this experiment, the model-chute is oriented with its x-axis vertical and the ball containing the transmitters is tracked as it falls. Since the data acquisition rate is known, the time between data points is known. From the trajectory $x(t) = 0.5at^2$ predicted by the signal processing backward algorithm, the acceleration a of the sphere can be computed by fitting the trajectory with a quadratic. This yielded $a = 383.97$ inch/s^2 which is in very good agreement with the accepted value of $g = 386.4$ inch/s^2. Only the typical results in x, y, z are shown in Figures 6.1, 6.2 and 6.3. Details can be found in Gupta [20]. From the free fall test results it can be concluded that the DAS is capable of real time data acquisition.

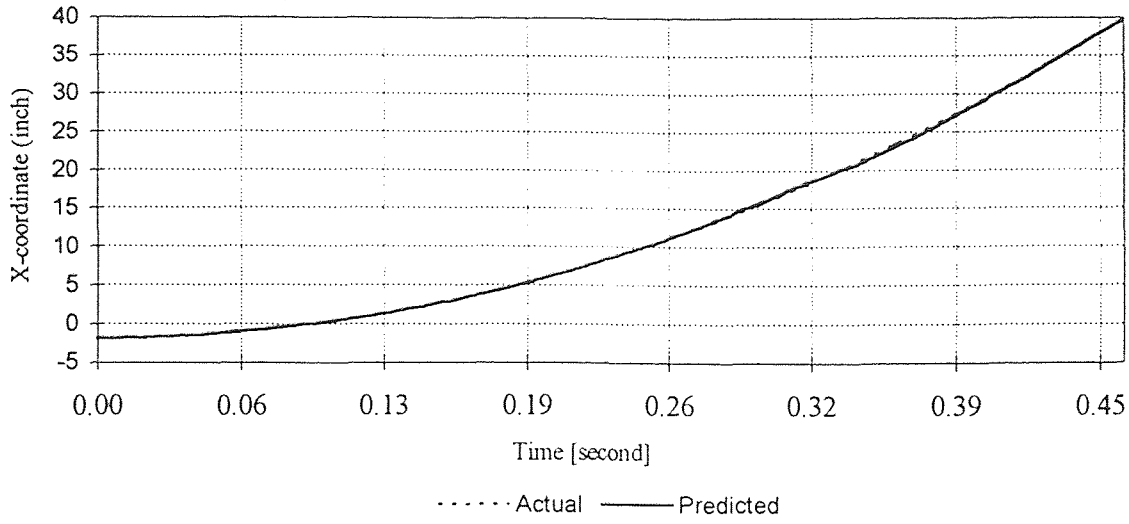

Figure 6.1 Free fall test: X plot

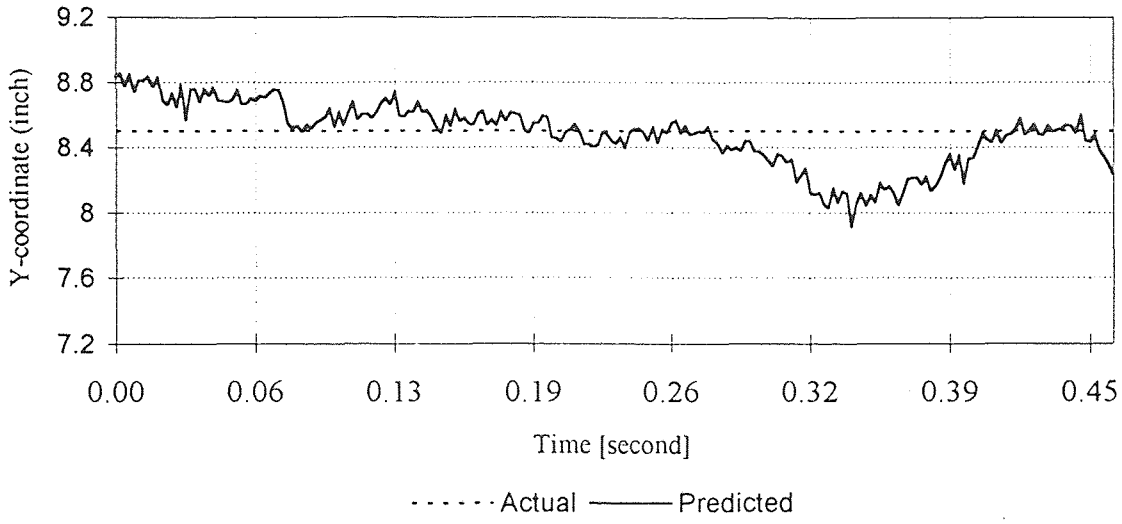

Figure 6.2 Free fall test: Y plot

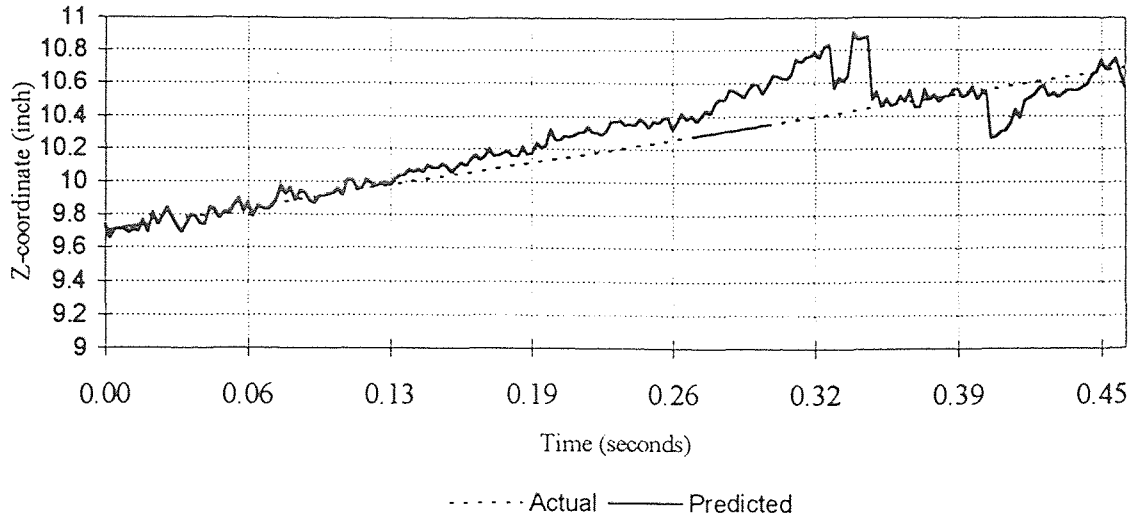

Figure 6.3 Free fall test: Z plot

6.2 Vibrated Bed Results

It has been observed that in vibrated beds larger particles tend to rise to the top. This has been attributed to convective transport. Recently, experiments have been conducted in our laboratory (La Rosa [21], Rosato et al. [22]) to study this phenomenon. The experiments simply measured the time required for a single large particle to be carried to the surface of the bed. The 3-dimensional, non-intrusive particle tracking system has been adapted to study the actual trajectory of this large particle. One set of results is presented in Figures 6.4 to 6.9. In this experiment, the larger (transmitting) sphere of 1" diameter was placed at the bottom of a bed of 0.125" diameter particles and the bed was vibrated at 15 Hz with an amplitude of 0.125". It was observed that the particle rose to the top of the bed in less than 17 seconds. The Fast Fourier Transform (FFT) of the movement of the sphere in X-direction is shown in Fig. 6.4c. The dominant frequency of 7.5 Hz, as

expected, is half the frequency of vibration. Additional results obtained from the vibrated bed setup are presented in Appendix D.

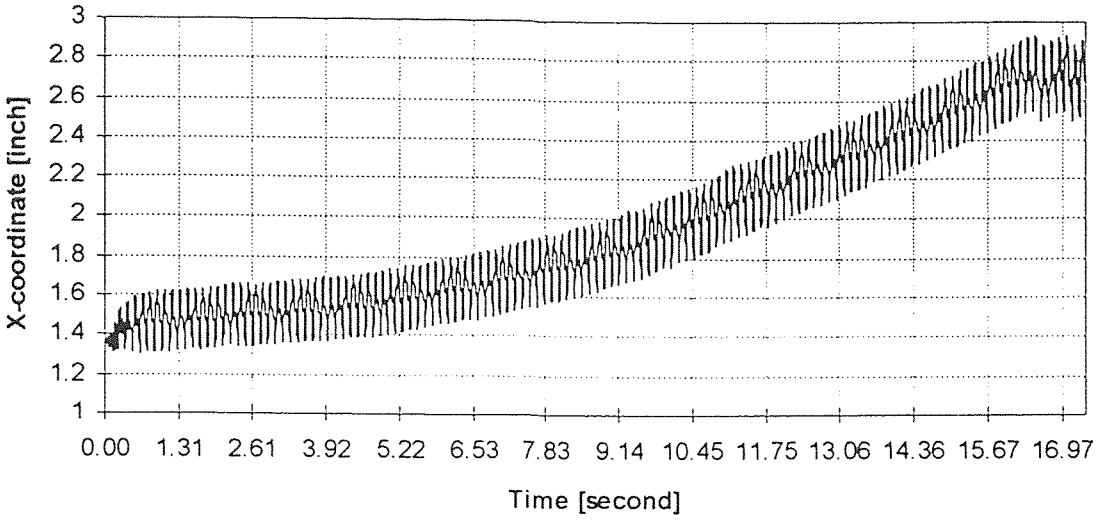

Figure 6.4a Vibrated Bed (f = 15 Hz, a = 0.125"): X plot

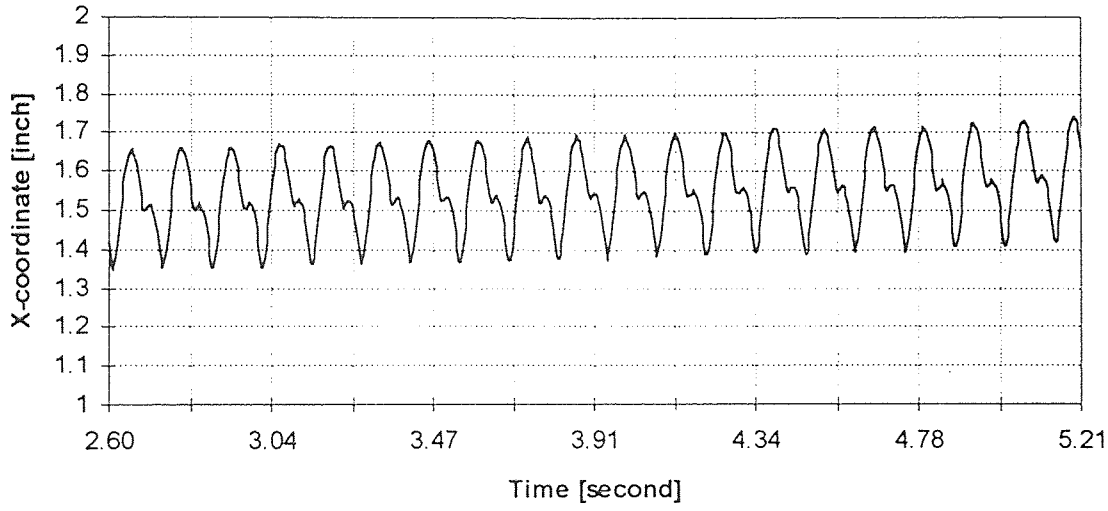

Figure 6.4b Vibrated Bed (f = 15 Hz, a = 0.125"): X plot (detailed view)

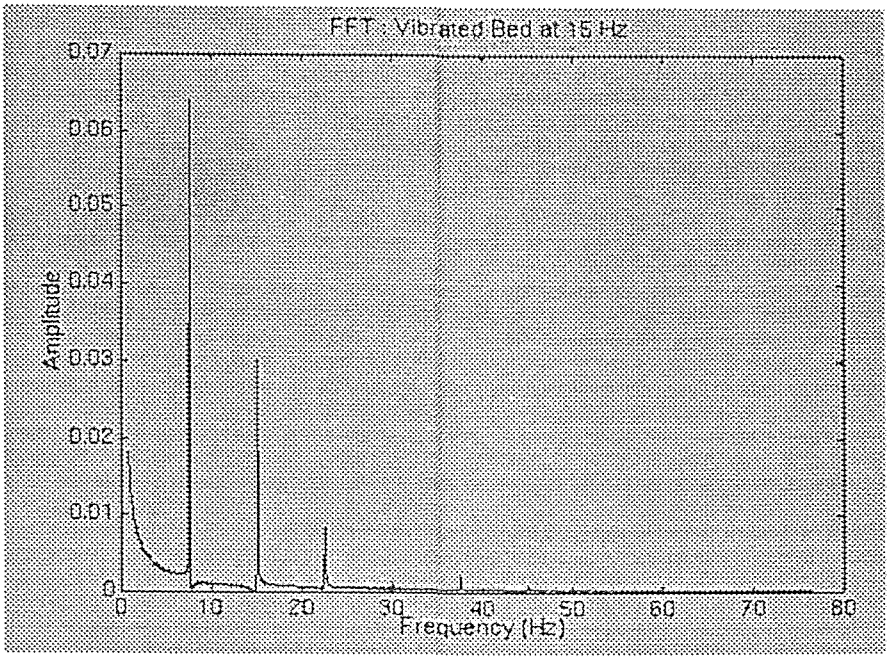

Figure 6.4c Vibrated Bed (f = 15 Hz, a = 0.125"): FFT of X plot

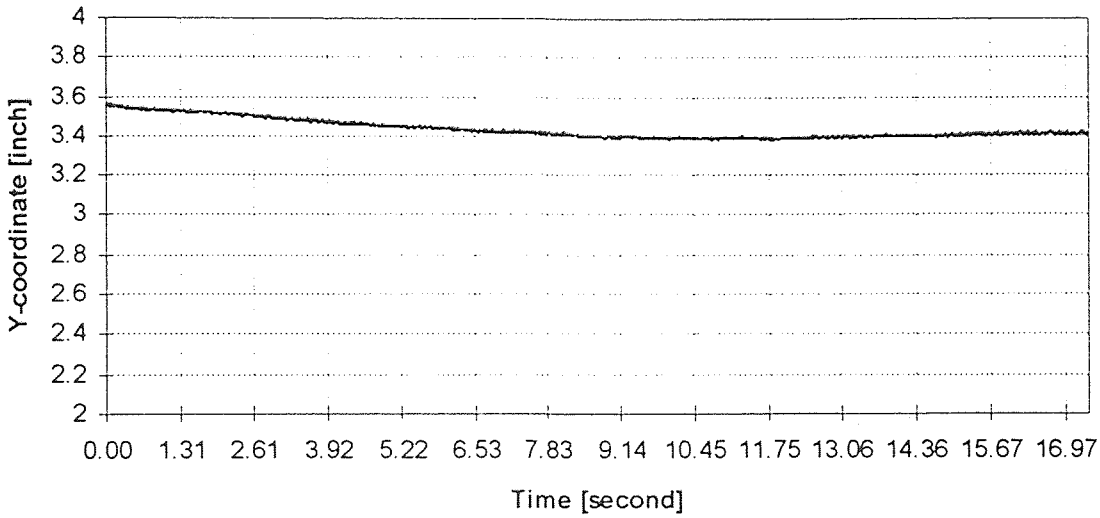

Figure 6.5 Vibrated Bed (f = 15 Hz, a = 0.125"): Y plot

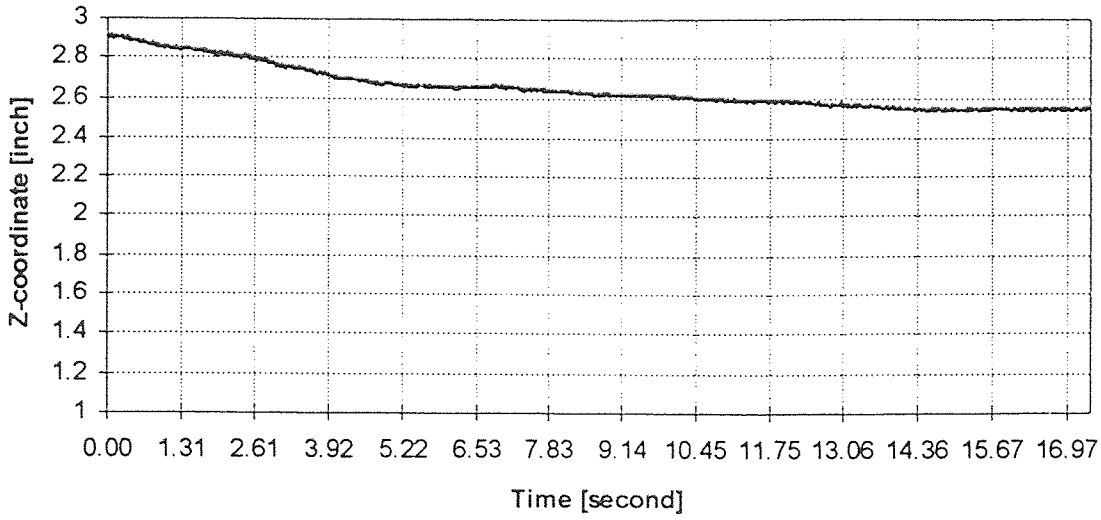

Figure 6.6 Vibrated Bed (f = 15 Hz, a = 0.125"): Z plot

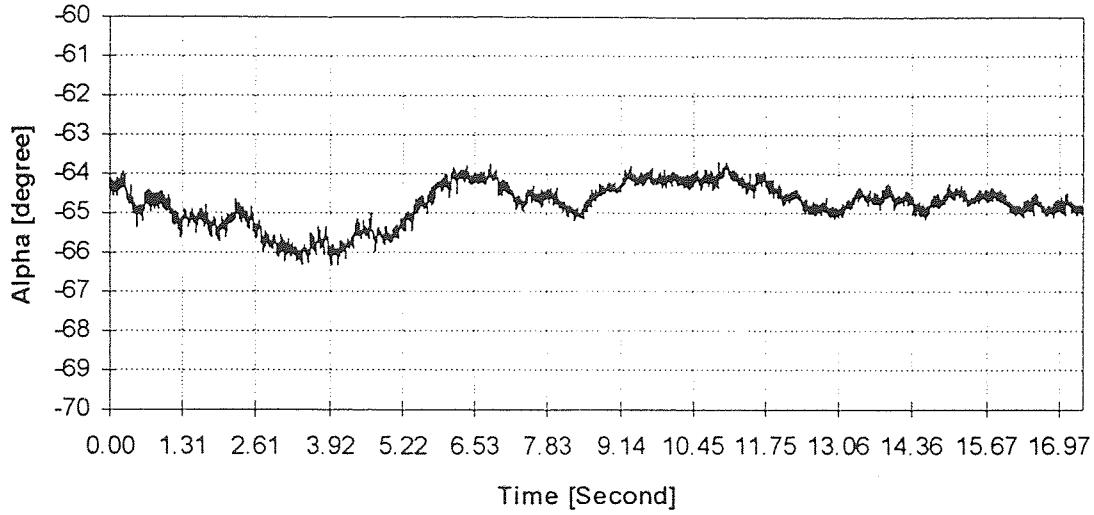

Figure 6.7 Vibrated Bed (f = 15 Hz, a = 0.125"): α plot

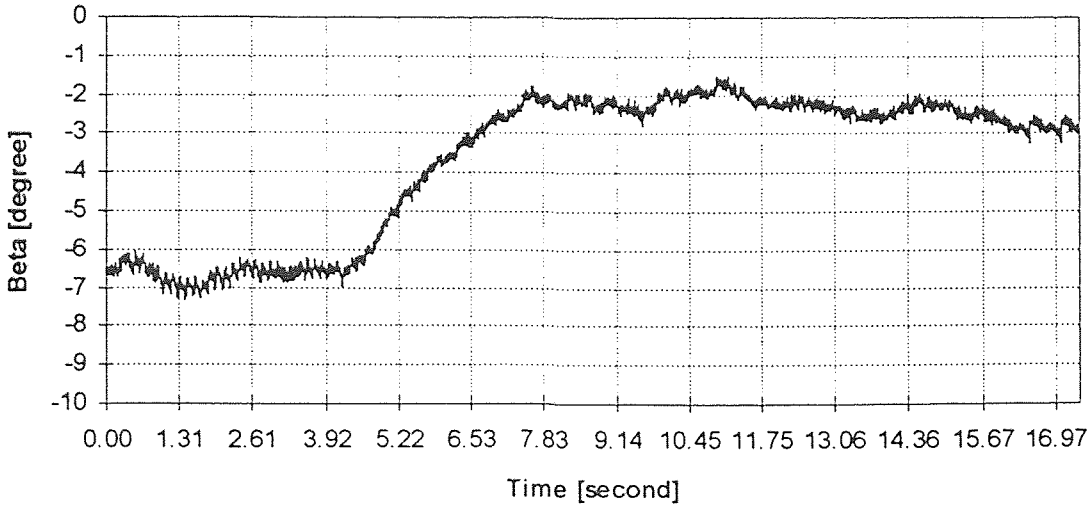

Figure 6.8 Vibrated Bed (f = 15 Hz, a = 0.125"): β plot

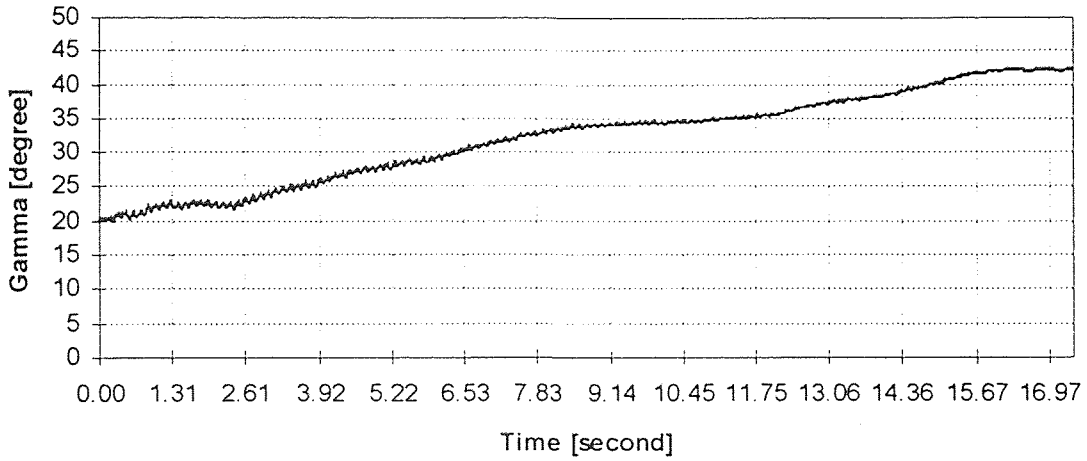

Figure 6.9 Vibrated Bed (f = 15 Hz, a = 0.125"): γ plot

6.3 Inclined Chute Results

Figures 6.10 to 6.15 are the results obtained from the bottom half of inclined chute setup. In the incremental (controlled) trajectory "cbstrt" presented below, the transmitting sphere is held in the calibration jig. The jig is then moved along the global x-axis from x=59" to x=107" in 2" increments except at data points 15 (where the increment is 3") and 17 (where the increment is 1"). The y and z coordinates are kept fixed at 12" and rotations α, β and γ are zero degrees. Very good results are obtained with only 0.34", 0.10" and 0.06" mean errors in x, y and z coordinates and 1.47°, 0.70° and 0.56° mean error in α, β and γ rotations respectively. Additional results obtained from the top as well as the bottom half of the inclined chute are presented in Appendix E.

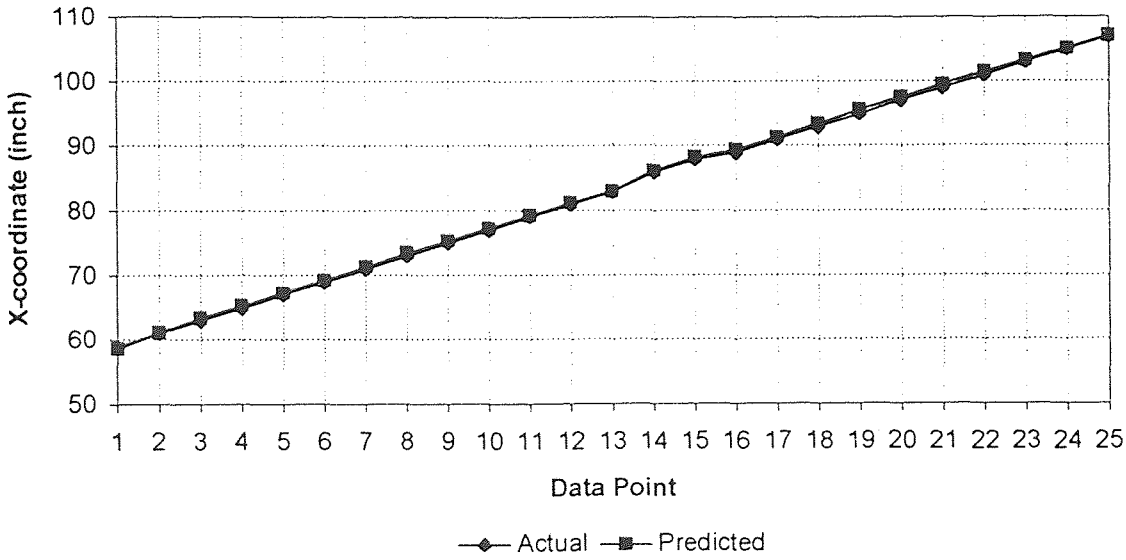

Figure 6.10 Run cbstrt: X plot
(maximum error = 0.61", mean error = 0.34", standard deviation = 0.15°)

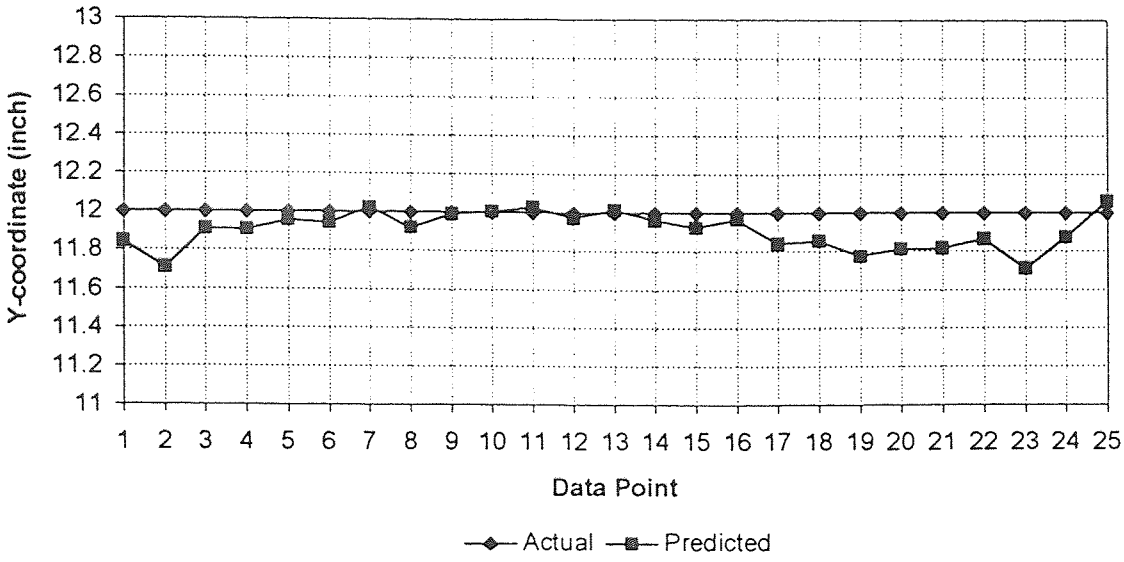

Figure 6.11 Run cbstrt: Y plot
(maximum error = 0.29", mean error = 0.10", standard deviation = 0.08")

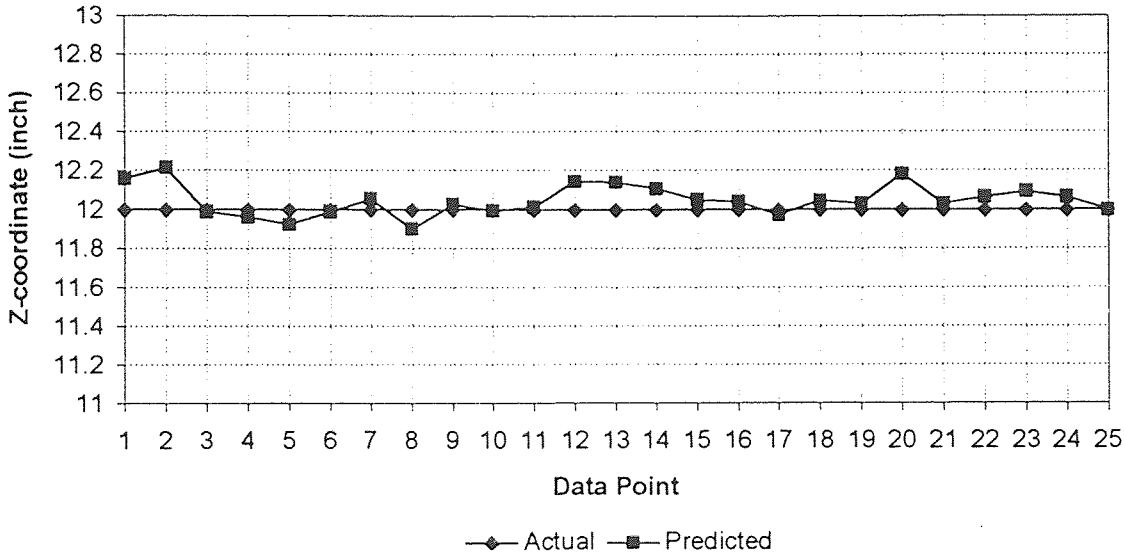

Figure 6.12 Run cbstrt: Z plot
(maximum error = 0.21", mean error = 0.06", standard deviation = 0.05")

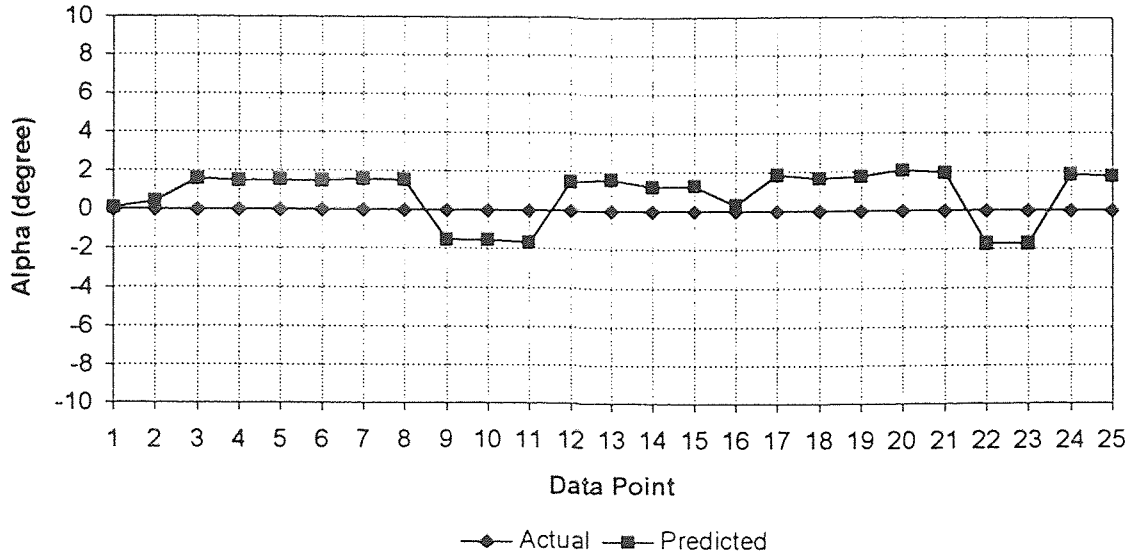

Figure 6.13 Run cbstrt: α plot
(maximum error = 2.07°, mean error = 1.47°, standard deviation = 0.47°)

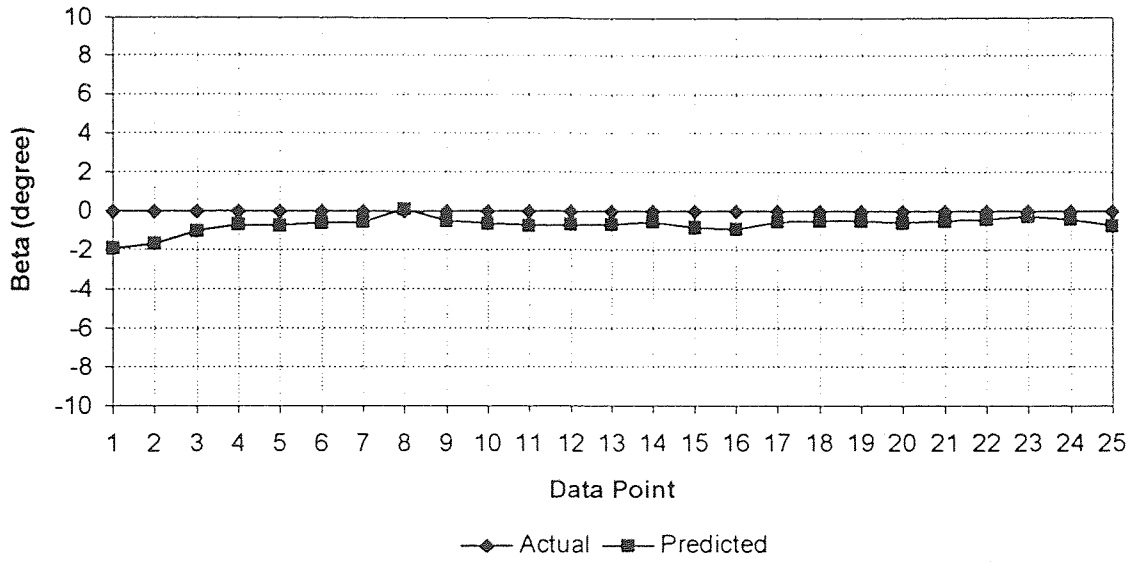

Figure 6.14 Run cbstrt: β plot
(maximum error = 1.92°, mean error = 0.70°, standard deviation = 0.37°)

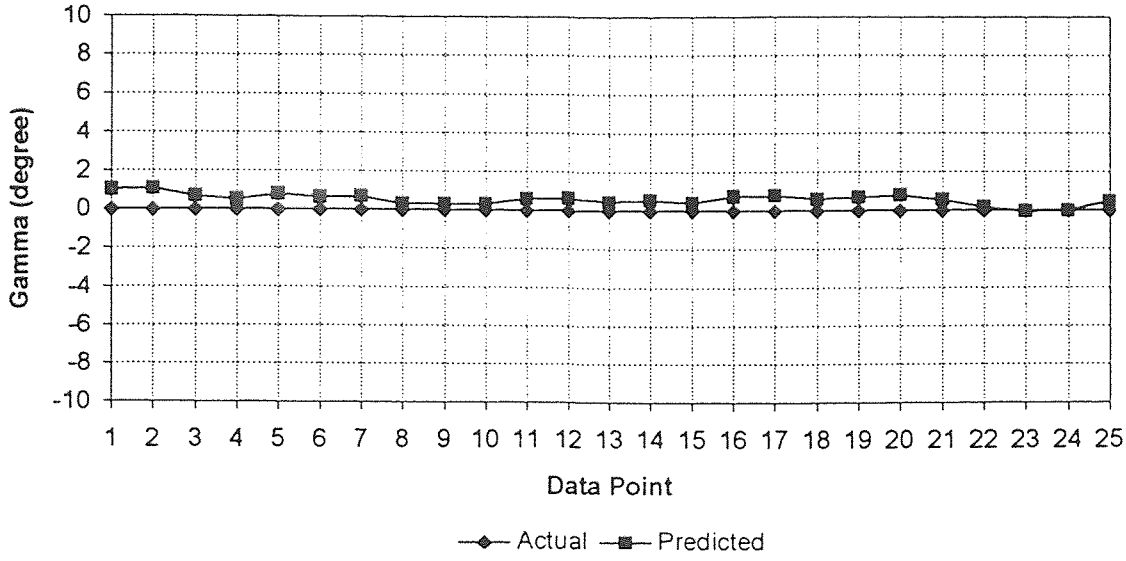

Figure 6.15 Run cbstrt: γ plot
(maximum error = 1.09°, mean error = 0.56°, standard deviation = 0.25°)

The tracking system has been tested on the vibrated bed in incremental as well as fast mode while in the inclined chute, only incremental testing has been done. From the results plotted above and in Appendices D and E, it can be concluded that the tracking system is capable of providing accurate and meaningful results. The accuracies of the tracking system for vibrated bed and inclined chute are summarized in Table 6.1.

Table 6.1 Accuracies of the tracking system

Accuracy	Vibrated Bed	Inclined Chute
Linear	0.03"	0.3"
Angular	1°	10°

CHAPTER 7

DATA SMOOTHING AND VELOCITY CALCULATION

7.1 Smoothing of the Results

Errors present in the tracking system are of two types: systematic errors and random errors. Sources of the systematic errors and techniques employed to correct these have been discussed in Chapter 3 and Chapter 4. In this section we discuss the random errors and a smoothing technique for minimizing their effect.

Random errors are unpredictable fluctuations that may be introduced by various factors such as radio noise, electromagnetic reflection etc. In order to check the nature of these random errors in the tracking system, an experiment was performed in the vibrated bed setup. The transmitting sphere was kept stationery at one position and data was collected at 463 Hz for two seconds. This data was then used to generate histograms, one of which is presented in Figure 7.1.

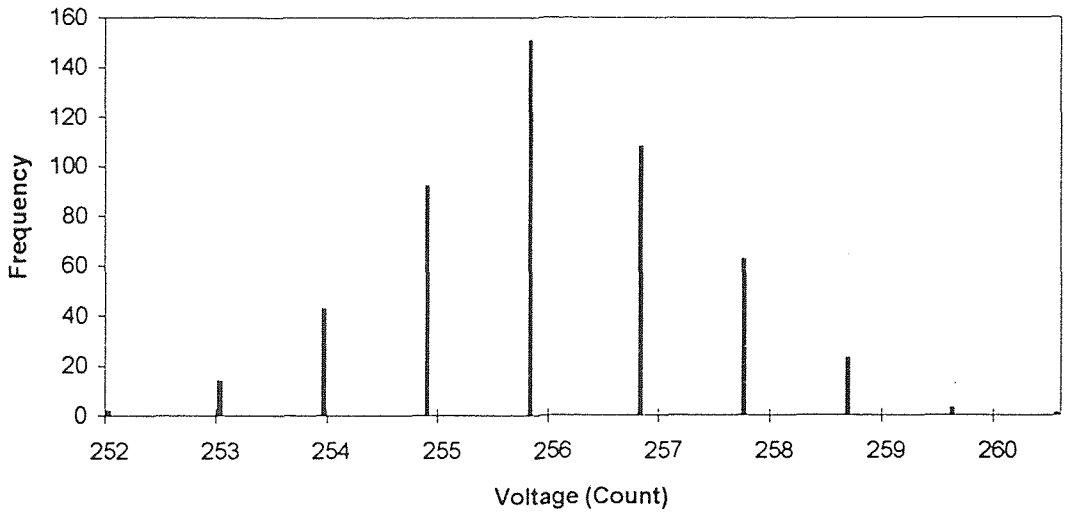

Figure 7.1 Histogram for voltage (counts)

After processing the voltage data, histograms were also generated for calculated trajectory (x, y, z, α, β, γ). The histogram for α rotation is shown in Figure 7.2. It is seen that the random errors present in voltages and resulting trajectories are almost Gaussian in nature.

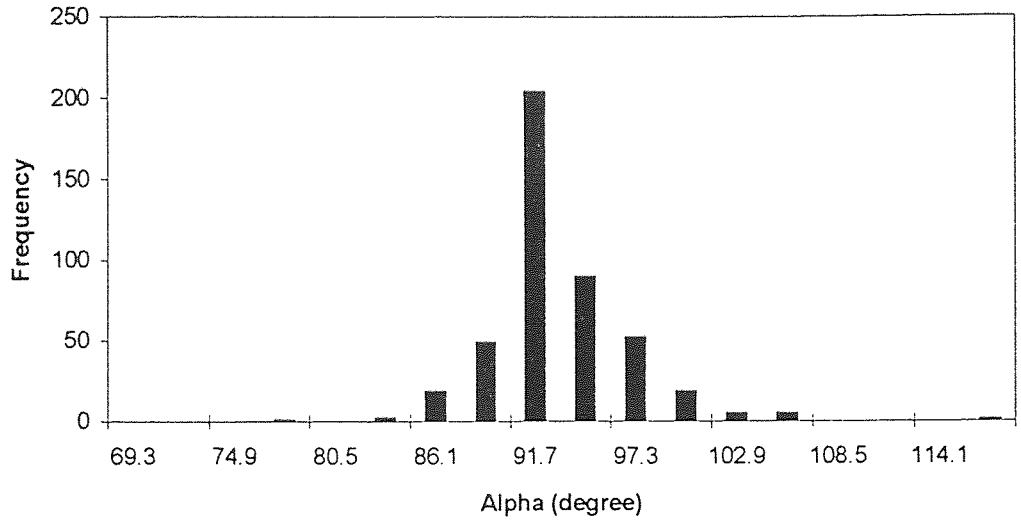

Figure 7.2 Histogram for α rotation

It has been observed that the effect of random errors which are generally Gaussian in nature, can be minimized by using Gaussian smoothing techniques (Bevington [23]) and the nature of this Gaussian distribution can be expressed by the following equation:

$$f(x) = \frac{1}{\sigma\sqrt{2\pi}} e^{-\frac{1}{2}\left(\frac{x-\mu}{\sigma}\right)^2} \qquad (7.1)$$

where,

σ is the standard deviation of the data.

μ is the mean value of data.

The smoothing technique is implemented in the form of equation (7.2) [24]. The smoothing is done in steps, determined by the number of passes P_n. The number of points in the range i_{min} to i_{max} considered for applying Gaussian weights is determined by the standard deviation σ specified by the user. In the first pass, smoothing is done directly on the unsmoothed data and in the subsequent passes, Gaussian weights are applied to the difference between unsmoothed and smoothed values of the points over the interval i_{min} to i_{max}. The amount of smoothing is thus affected by the number of successive passes and standard deviation. Thus there is a complete control over the smoothing process.

$$smo\_pt(n_P) = \sum_{P=0}^{P_n} \sum_{n=0}^{n_p} \sum_{i=i_{min}}^{i_{max}} \left(pt(n) - smo\_pt(n_{P-1}) \frac{1}{\sigma\sqrt{2\pi}} e^{-\frac{1}{2}\left(\frac{i-n}{\sigma}\right)^2} \right) \qquad (7.2)$$

where,

$pt(n)$ is the unsmoothed value of data point n.

$smo\_pt(n_P)$ is the smoothed value of data point n after P passes.

P_n is the total number of passes.

n_p is the total number of points.

i_{min} and i_{max} define the moving range of points over which Gaussian weights are applied.

Figure 7.3 shows the effect of smoothing applied to the results. The plot depicts the result of a "rigid vibration" experiment. In this experiment, the transmitting sphere is rigidly mounted on the vibration exciter of the vibrated bed setup and vibrated at a frequency of 25 Hz. Figure 7.3 shows both the raw (unsmoothed) and smoothed result of this experiment. Since the vibration is in x direction, only the X plot is shown here.

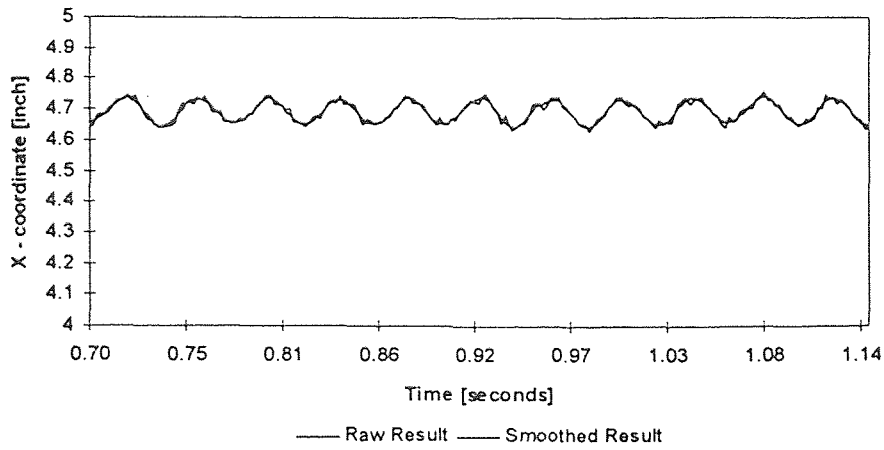

Figure 7.3 Effect of smoothing on rigid vibration result: X plot

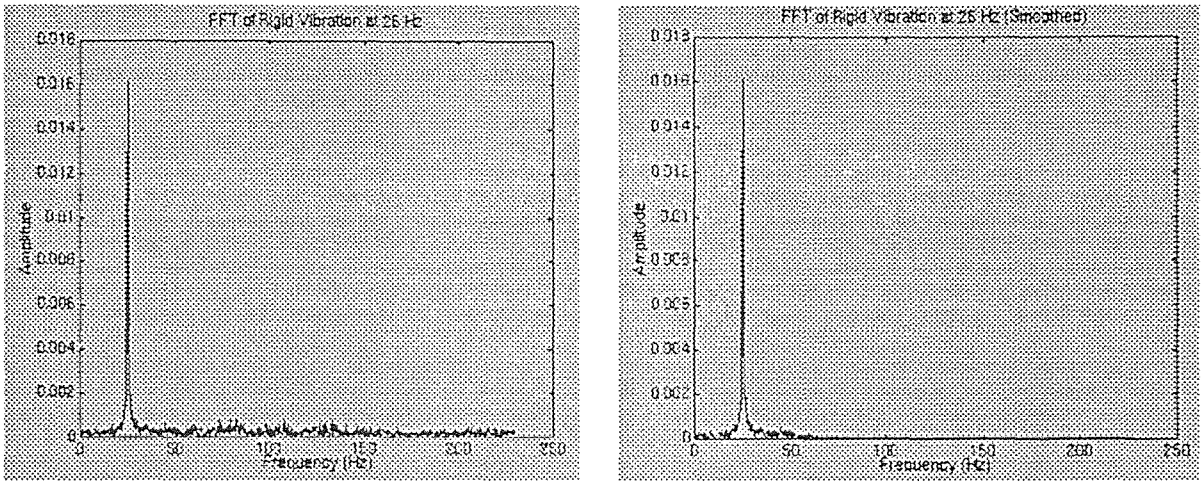

(a) (b)

Figure 7.4 Effect of smoothing on rigid vibration result: FFT

Figure 7.4 shows FFTs of the two data series in Figure 7.3. Figure 7.4(a) is the FFT of rigid vibration X plot before smoothing. It is seen that besides the dominant 25 Hz frequency, noise of higher frequency is also present. Figure 7.4(b) is the FFT of rigid vibration X plot after smoothing. The high frequency noise present in the unsmoothed results is no longer seen. A marked improvement is observed in Figures 7.3 and 7.4.

7.2 Calculation of Velocities

Once the position and orientation of the tracking sphere is known, the next step in data processing is the calculation of velocity of the ball - both linear as well as angular. The results should be post-processed prior to calculating the velocities because random errors and multiple solutions in solutions can result in large and unrealistic fluctuations in calculated velocities. This post-processing is done by smoothing the results (Section 7.1) and by reducing multiple solutions in orientations (Chapter 5).

We know that velocity is the first derivative of displacement. Hence, velocity of the transmitting sphere can be calculated numerically using the "Five Point Formula" discussed by Burden et al. [25]. This formula is used to calculate the components of linear as well as angular velocities of the sphere.

$$V_{i_j} = \frac{\left(X_{i_{j-2}} - 8X_{i_{j-1}} + 8X_{i_{j+1}} - X_{i_{j+2}}\right)}{12t} \tag{7.3}$$

where,

$X = \{x, y, z, \alpha, \beta, \gamma\}$

$V = \{V_x, V_y, V_z, \omega_x, \omega_y, \omega_z\}$

t is the time between consecutive readings

X_{i_j} is X_i at data point j

V_{i_j} is V_i at data point j

Velocities calculated for the rigid vibration experiment (discussed in Section 7.1) are presented in Figures 7.5 to 7.10. Figures 7.5 to 7.7 are the components of the linear

velocity V, while Figures 7.8 to 7.10 are the components of the angular velocity ω. The units used here are m/s for linear velocities and radian/s for angular velocities.

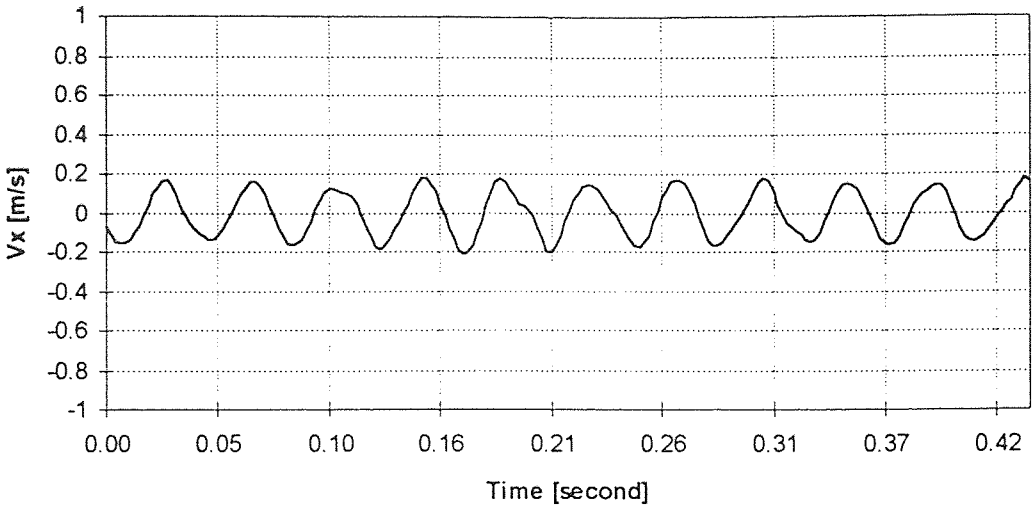

Figure 7.5 Linear velocity of rigid vibration: V_x

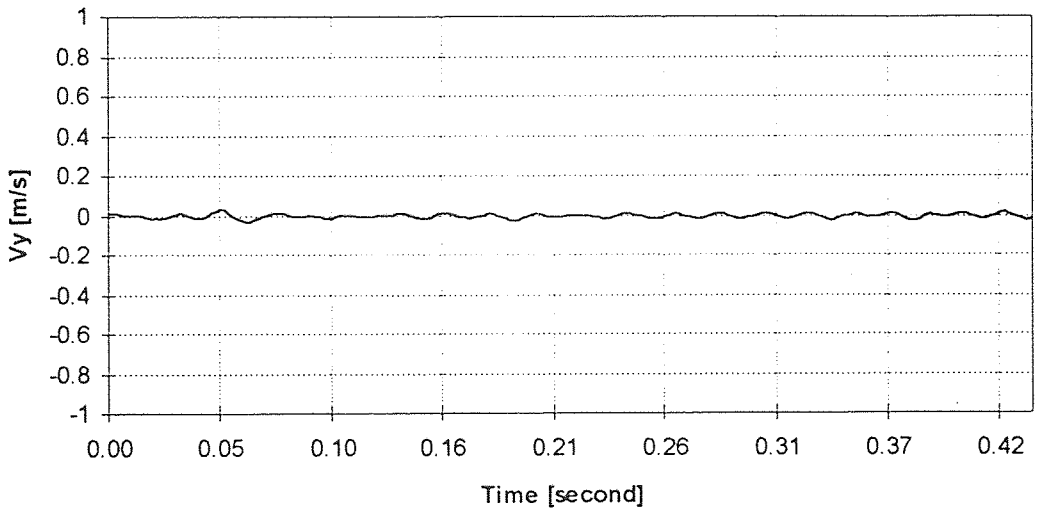

Figure 7.6 Linear velocity of rigid vibration: V_y

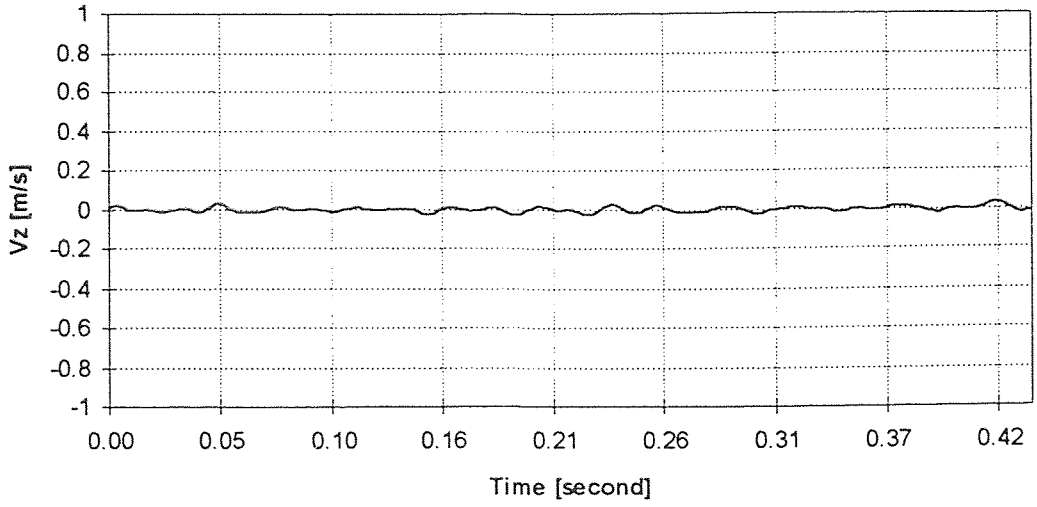

Figure 7.7 Linear velocity of rigid vibration: V_z

As expected, V_x (in the direction of vibration) is the major component of linear velocity with small fluctuations in V_y and V_z.

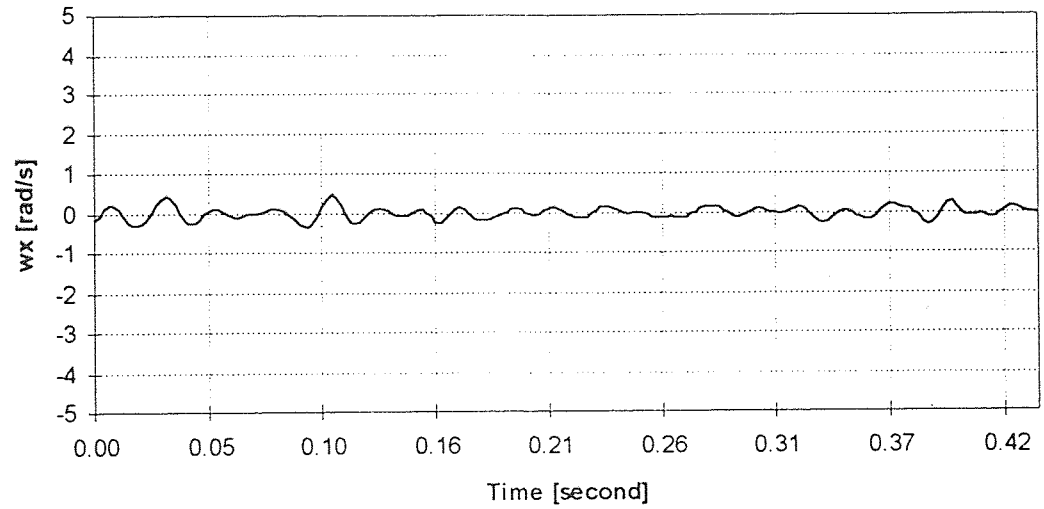

Figure 7.8 Angular velocity of rigid vibration: ω_x

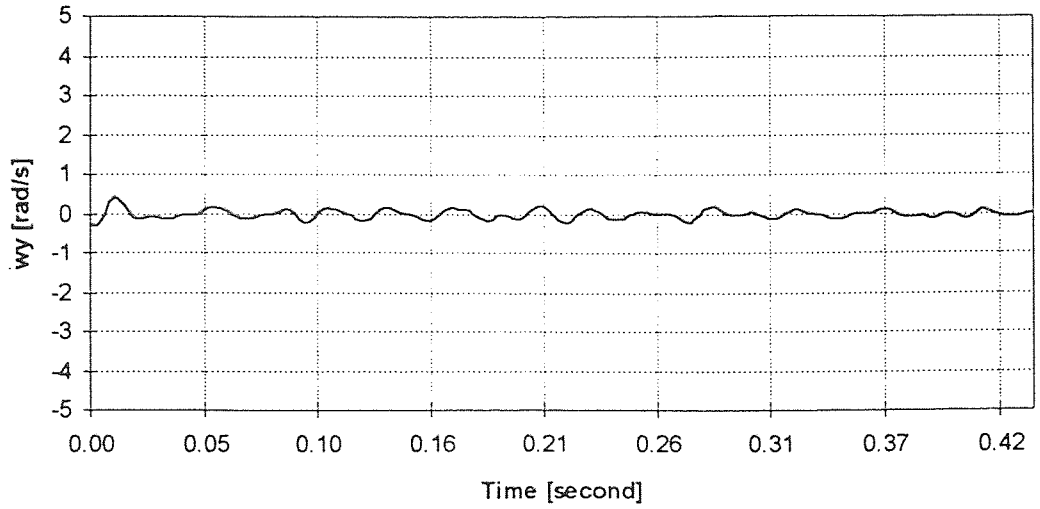

Figure 7.9 Angular velocity of rigid vibration: ω_y

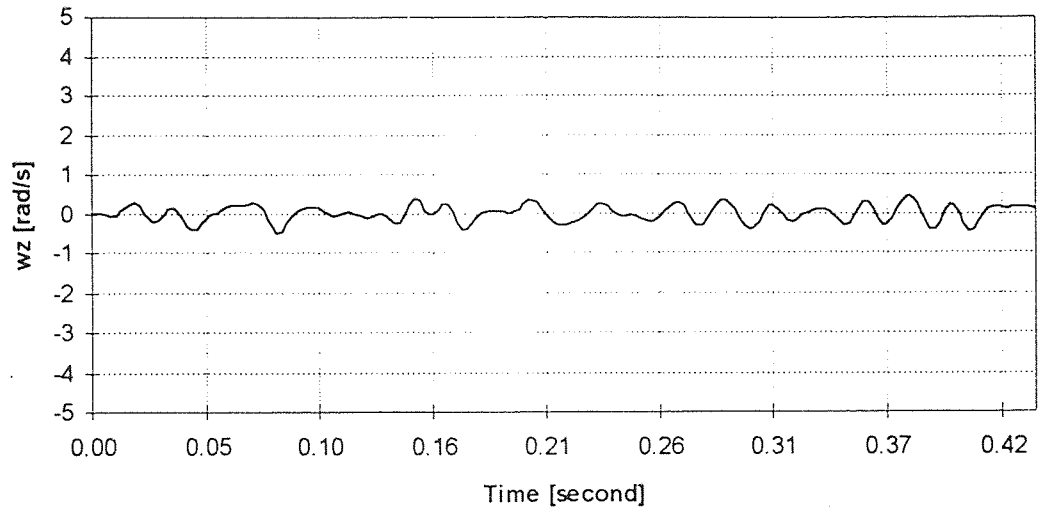

Figure 7.10 Angular velocity of rigid vibration: ω_z

Similarly it is also possible to calculate the accelerations as derivatives of velocities. Calculation of velocities and acceleration can provide valuable insight into a

physical process as velocity is directly related to energy and acceleration to forces and impulses.

Here it must be emphasized that the only direct measurement we have is that of the trajectory of the sphere. Velocity and acceleration are derived quantities. Since calculation of velocity and acceleration is the process of calculating derivatives of the positions and orientations, it is very sensitive to noise. Therefore, the accuracy with which velocity and acceleration can be calculated is dependent on the accuracy of calculation of the positions and orientations and success in filtering out the random errors and noise from the solution. Further work needs to be done on smoothing the results before velocity and acceleration can be calculated with a high degree of confidence. Hence caution should be exercised in directly interpreting the calculated velocity and acceleration values.

CHAPTER 8

SUMMARY AND CONCLUSIONS

8.1 Summary of Progress

In this thesis the implementation aspects of the three-dimensional non-intrusive particle tracking system were discussed. Various error reduction techniques were proposed and implemented. Experimental results obtained from the vibrated bed setup as well as some preliminary results from the inclined chute setup were also presented.

One of the main focus was the reduction of systematic as well as random errors. Effectiveness of the 27-point correction scheme proposed by Volcy [10] and implemented by Agrawal [9] was demonstrated experimentally and point [002] was chosen as the reference point. Further, an intuitive empirical equation was proposed to replace the 27-point correction scheme in order to overcome some of its inherent disadvantages. A Gaussian smoothing technique was also implemented for reduction of random errors present in the solution.

Another problem addressed was the multiple solutions in orientations. A solution re-extraction scheme was implemented as a post-processing technique to reduce these multiple solutions. Equivalent angle-axis representation was also introduced for better visualization of orientation results.

The tracking system has been implemented to the inclined chute and the vibrated bed experimental setup. Prior to conducting experiments, the antennae configuration was decided and the antennae were setup. The data acquisition system consisting of pre-amplifiers and demodulator boards was also fabricated. A switching circuit was designed and implemented by Ren [17] for the inclined chute setup in order to efficiently monitor

the whole chute. An optical switch was also developed by Ren [17] to conserve battery consumption.

A single data processing code was developed for all the systems by merging together different versions of the code into a single generic code controlled by command line arguments. Once the setup and solution scheme is specified, the tracking codes automatically choose the correct parameters to be used. The code was also made faster, more efficient and user friendly.

The particle tracking system has been used to obtain interesting results from the vibrated bed setup which were presented in Chapter Six and Appendix D. Further work still needs to be done on the inclined chute setup, before tracking experiments can be performed on it.

8.2 Future Work

The tracking system has been used to obtain accurate experimental results from the vibrated bed setup but further work can be done on the tracking system to perfect it and enhance its utility.

The tracking sphere is considered to be typical of the particles in the flow (for chute flows) or larger particles undergoing segregation (in the vibrated bed) whose trajectory is traced. But due to unequal weight distribution within the tracking sphere, the sphere becomes unbalanced and no longer remains typical of the other particles. This unbalance tends to bias the trajectory followed by the sphere and hence is of immediate and great concern and needs to be looked into immediately. The situation can be

remedied by better arrangement of electronic components and design and fabrication of a better packaging to balance the transmitting sphere.

Better and improved packaging is also desired to positively hold the transmitters in their relative positions inside the sphere and to facilitate quick and easy change of batteries without disturbing the transmitters.

The proposed empirical equation for replacing the 27-point correction is developed intuitively and needs to be carefully examined and fine tuned for obtaining optimum corrective effect for all the systems. An analytical approach could also be adopted for a more scientific approach to this problem.

Before the tracking system can be utilized to track the sphere in chute flow experiments, a major problem called the "Roll Problem" has to resolved. The roll problem appears only when the sphere rolls at high speeds, e.g. when speed of rotation, ω is high enough so that $= v / r$ where v is the translation speed and r is the radius of the sphere. It is characterized by significant deviations of computed positions (x, y, z) from the actual positions. These deviations occur at the same frequency as the roll frequency, thus indicating that fast changes in rotations affect the ability of the backward algorithm to resolve the positions accurately. The study of the roll problem is hampered by our inability to perform accurately controlled roll experiments. This is because we can not use any standard positioning devices available commercially for controlled roll experiments since they are made of metal and will interfere with the magnetic fields of the transmitters. Therefore, all the jigs, fixtures and mechanisms have to be fabricated of radio transparent materials and cannot be easily made as sophisticated as their commercially available

equivalents. Resolution of roll problem is a pre-requisite to successful tracking in the chute flow experiments.

Though the codes have been made more flexible and easy to use, further improvement is possible. It is possible to further automate the transition from data acquisition to data processing modules. The tracking system is currently *distributed*. The data acquisition is done using Pentium based PCs and data processing is done Sun Sparc workstations. The data processing codes can also be implemented on DOS based PCs in order to make the system more cohesive, easy to use and less expensive.

8.3 Conclusions

The Three-Dimensional Non-Intrusive Particle Tracking System has been improved and made more accurate and user-friendly. It has been tested through a series of experiments in the lab using three different setups. The results presented demonstrate that the tracking system is able to produce accurate (refer Table 6.1) and repeatable results as long as the rolls encountered are not fast.

Practical application of the tracking system is demonstrated by applying it to the study of vibrated beds. This application also proves that the tracking system is capable of three-dimensional, non-intrusive tracking.

APPENDIX A

MODEL-REALITY PLOTS

The data for all of these plots was collected using the old transmitter (used by Agrawal [9] for experiments and initial work on the 27-point scheme), and an antenna of dimensions 20" X 20". The voltages are scaled up by a factor of 10^6 for better visualization.

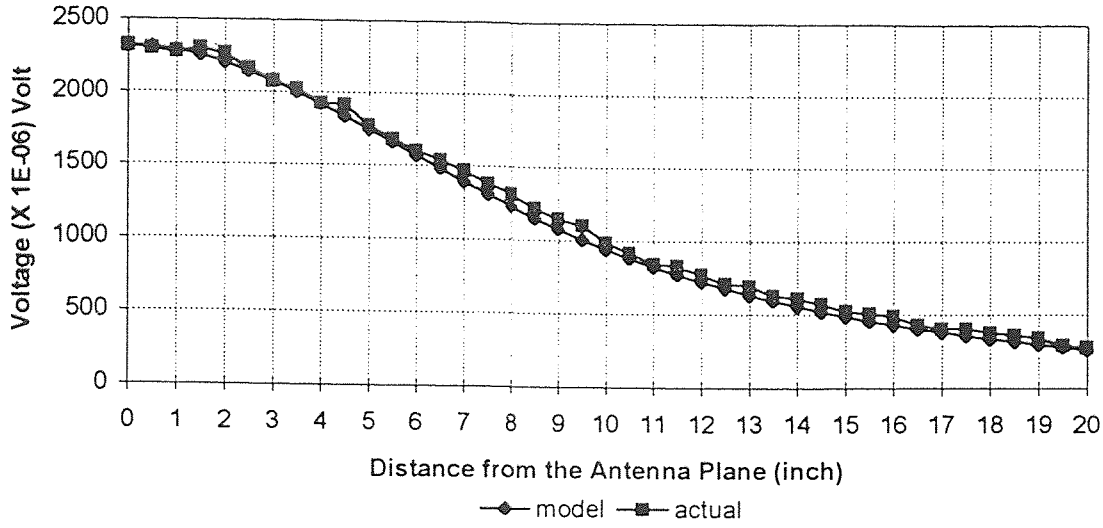

Figure A.1 M-R (I) no 27 point correction, calibration point [000]

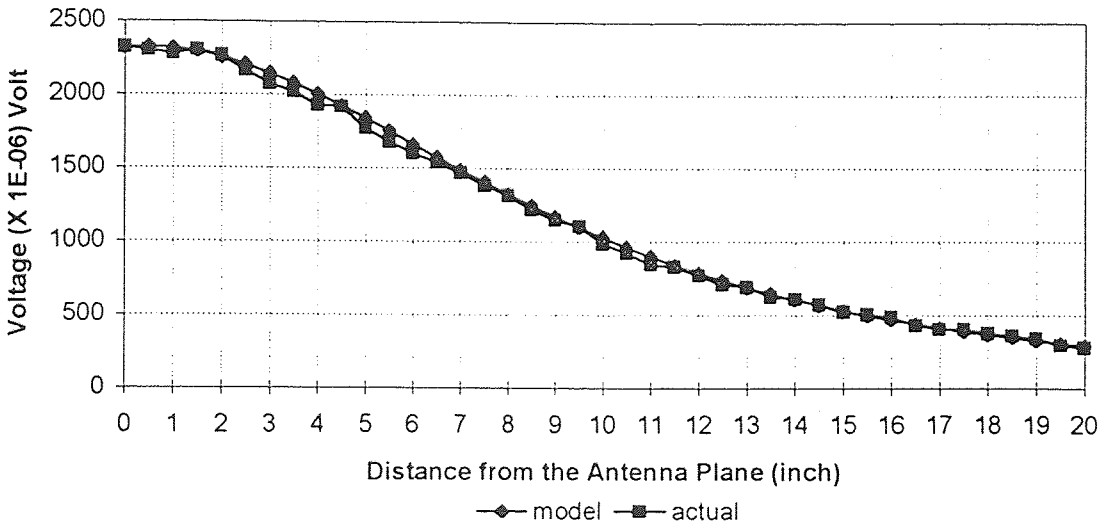

Figure A.2 M-R (I) using 27 point correction, calibration point [000]

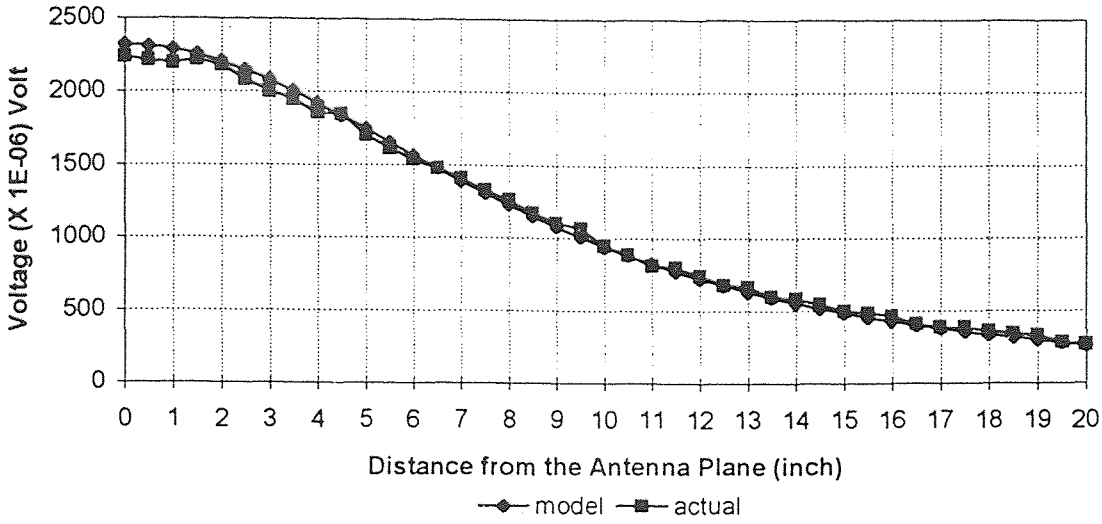

Figure A.3 M-R (I) no 27 point correction, calibration point [001]

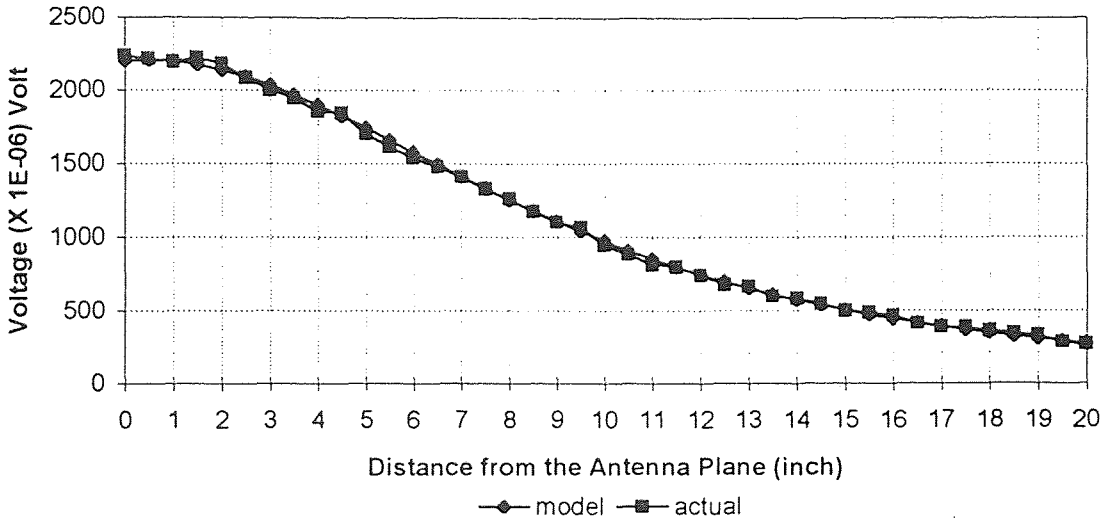

Figure A.4 M-R (I) using 27 point correction, calibration point [001]

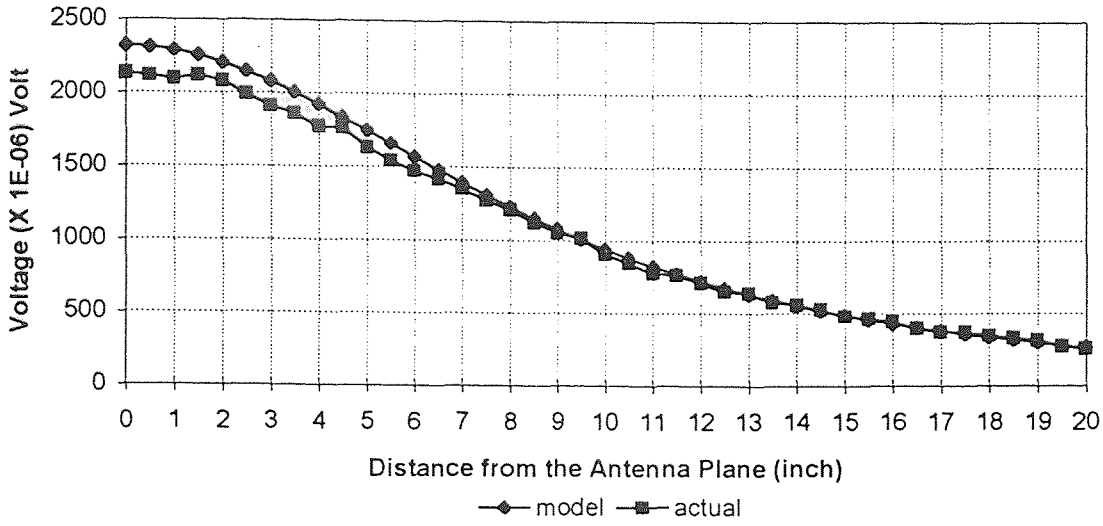

Figure A.5 M-R (I) no 27 point correction, calibration point [002]

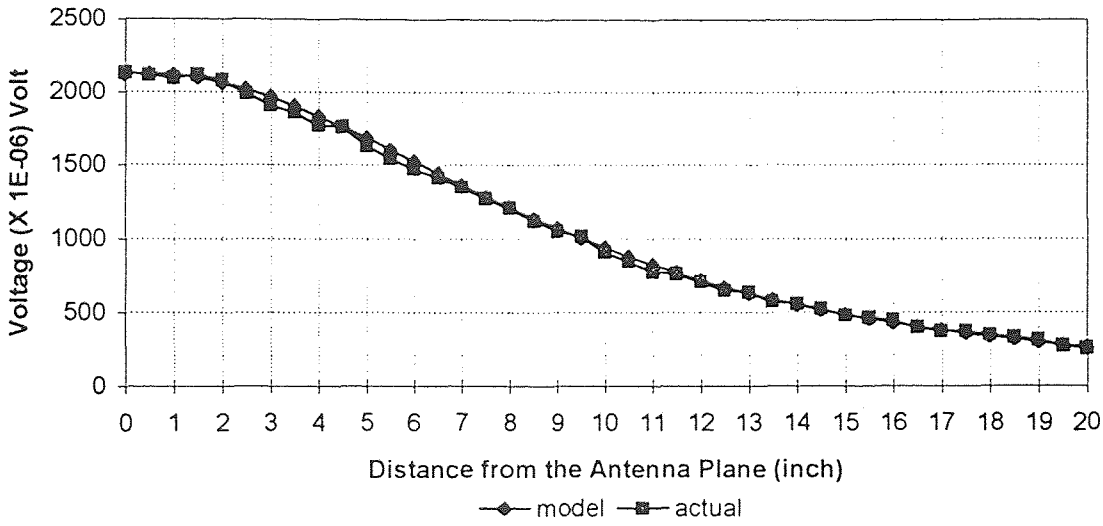

Figure A.6 M-R (I) no 27 point correction, calibration point [002]

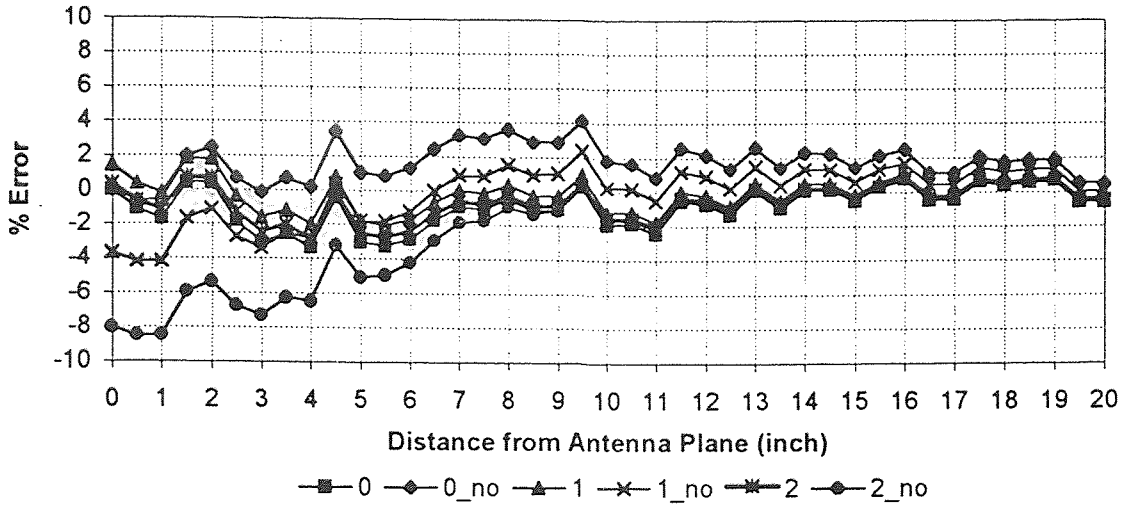

Figure A.7 Error Plot for M-R (I)

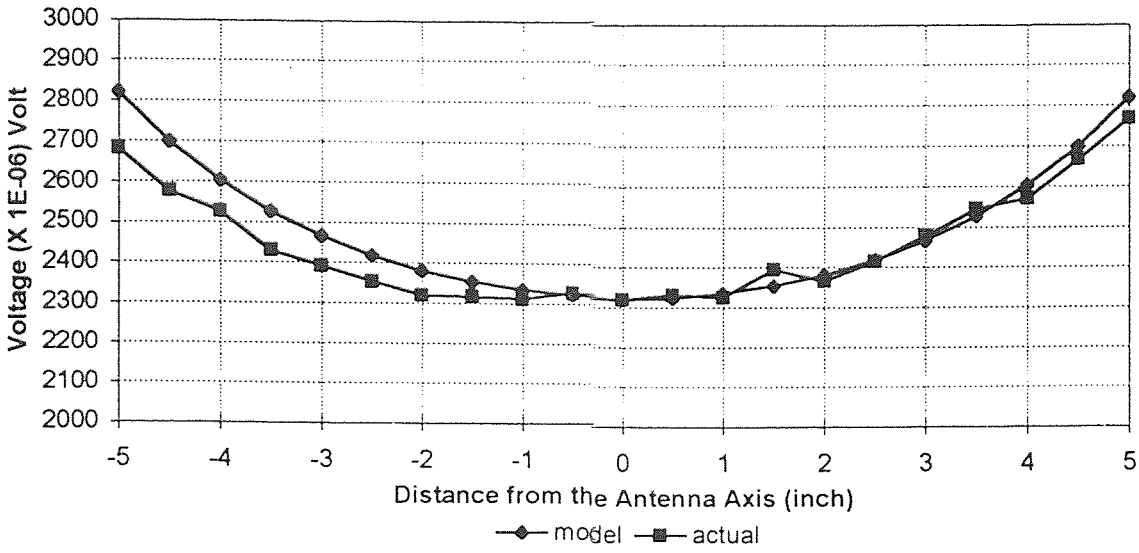

Figure A.8 M-R (II) no 27 point correction, calibration point [000]

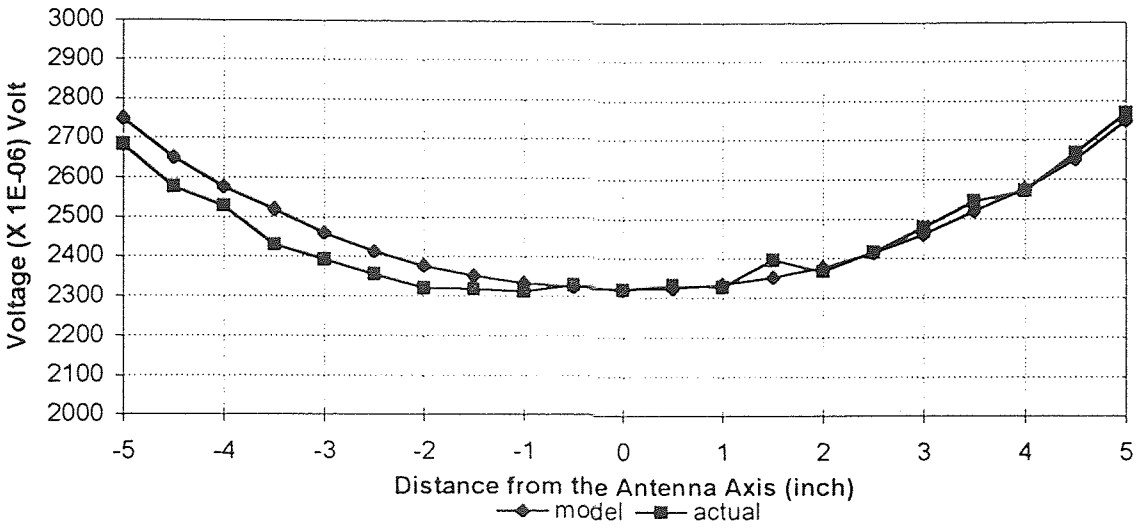

Figure A.9 M-R (II) using 27 point correction, calibration point [000]

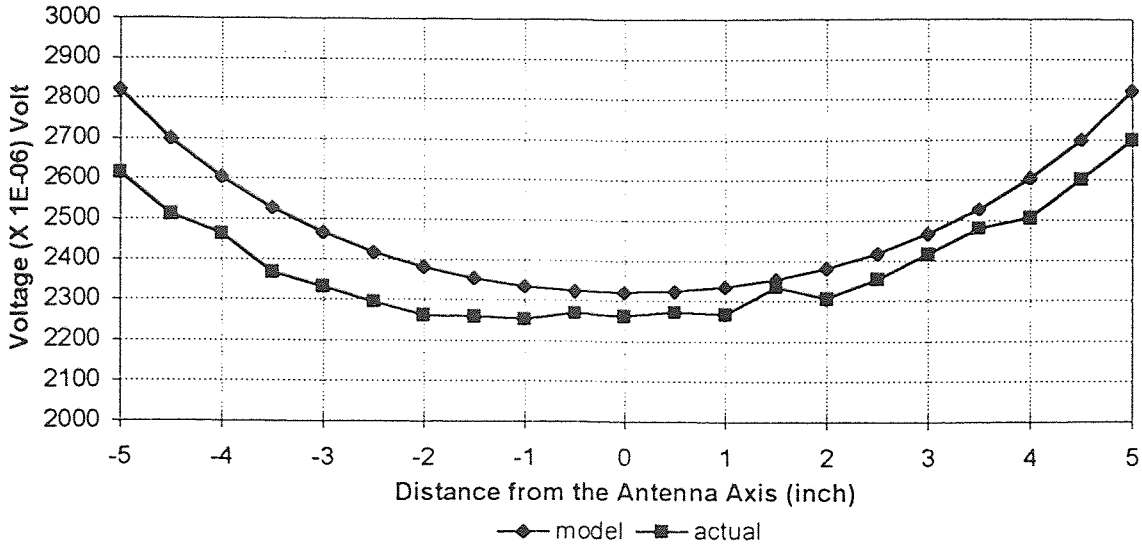

Figure A.10 M-R (II) no 27 point correction, calibration point [001]

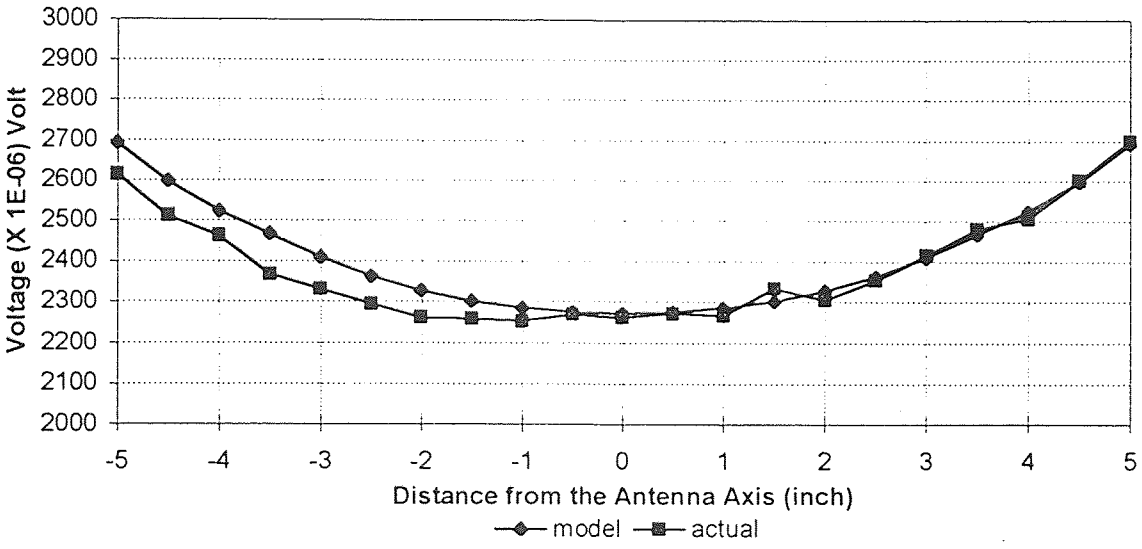

Figure A.11 M-R (II) using 27 point correction, calibration point [001]

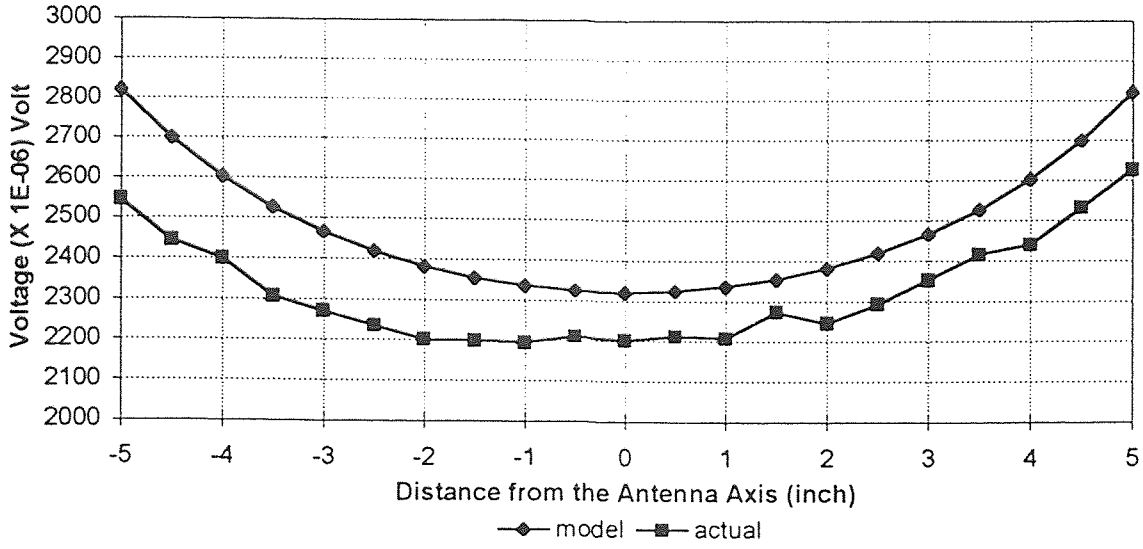

Figure A.12 M-R (II) no 27 point correction, calibration point [002]

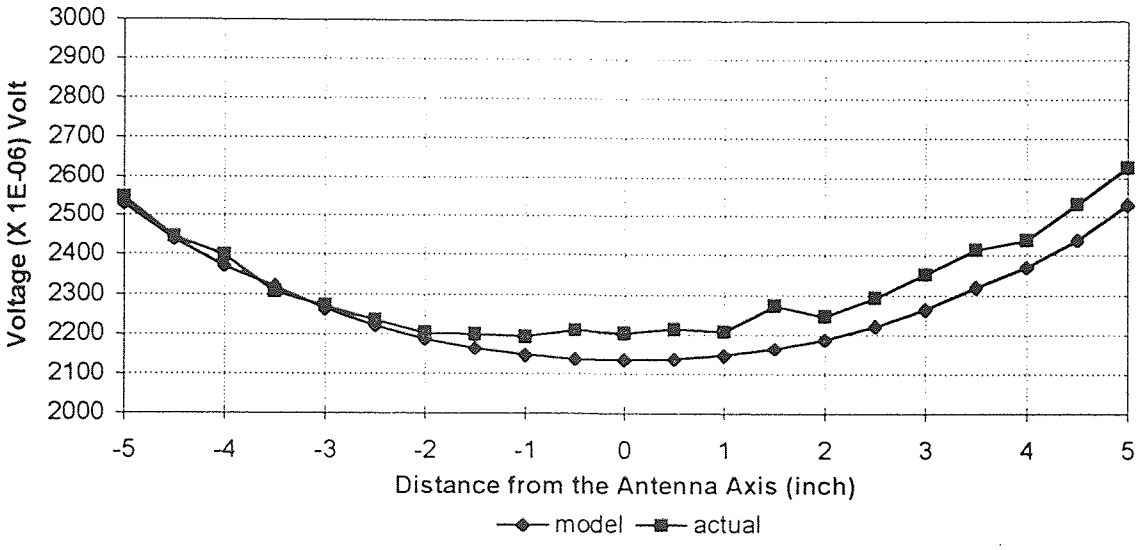

Figure A.13 M-R (II) using 27 point correction, calibration point [002]

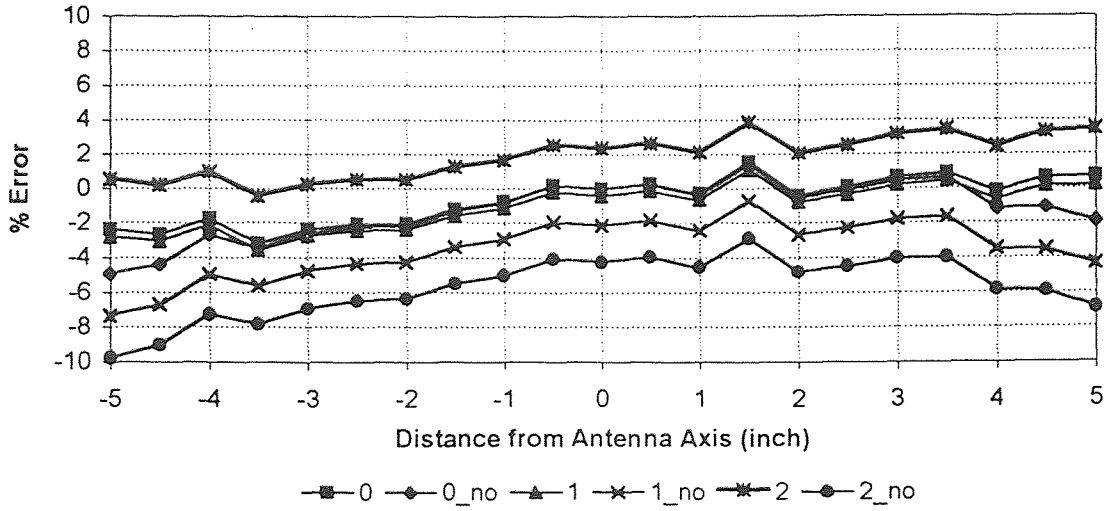

Figure A.14 Error Plot for M-R (II)

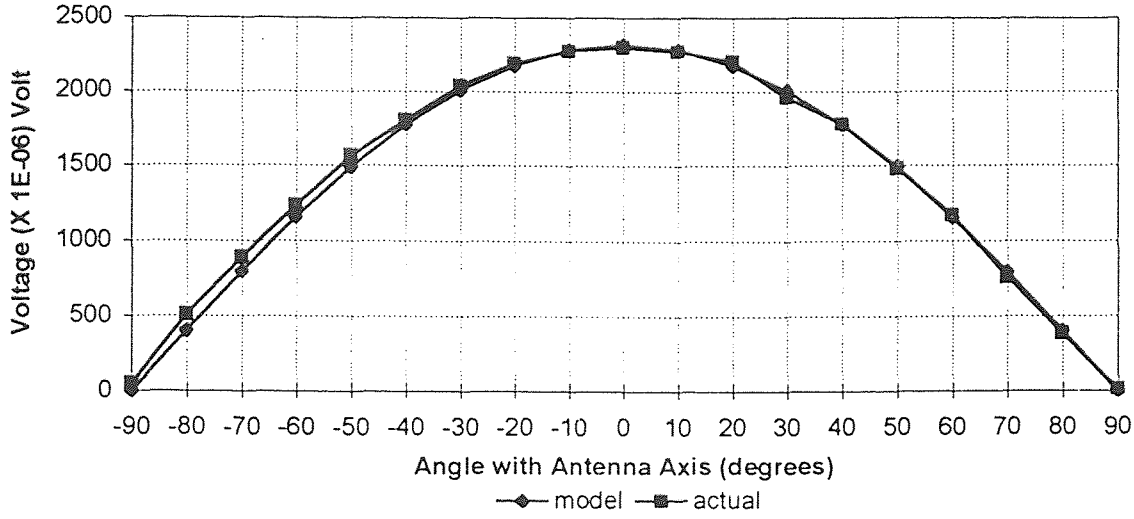

Figure A.15 M-R (III) no 27 point correction, calibration point [000]

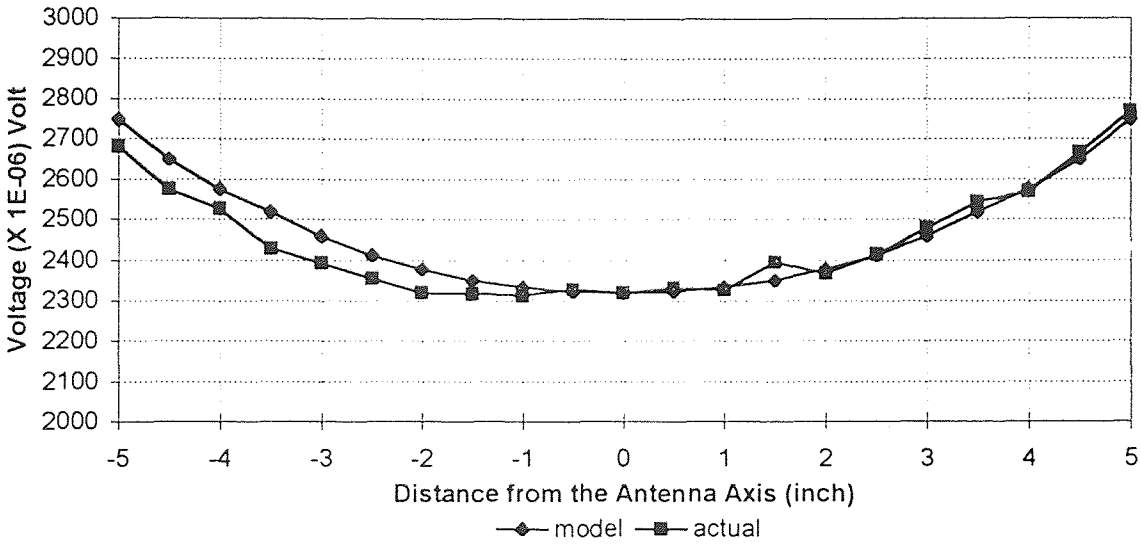

Figure A.16 M-R (III) using 27 point correction, calibration point [000]

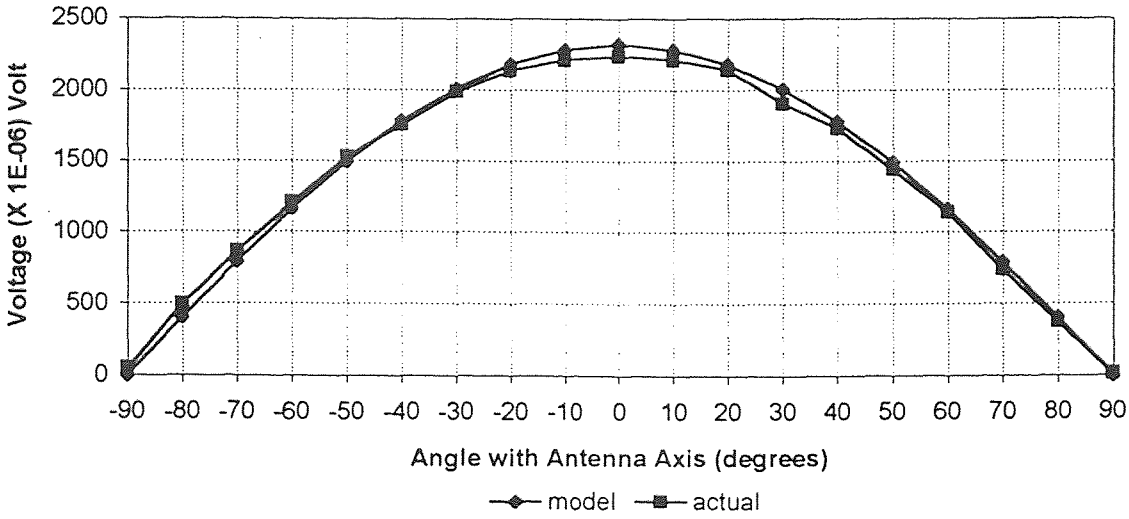

Figure A.17 M-R (III) no 27 point correction, calibration point [001]

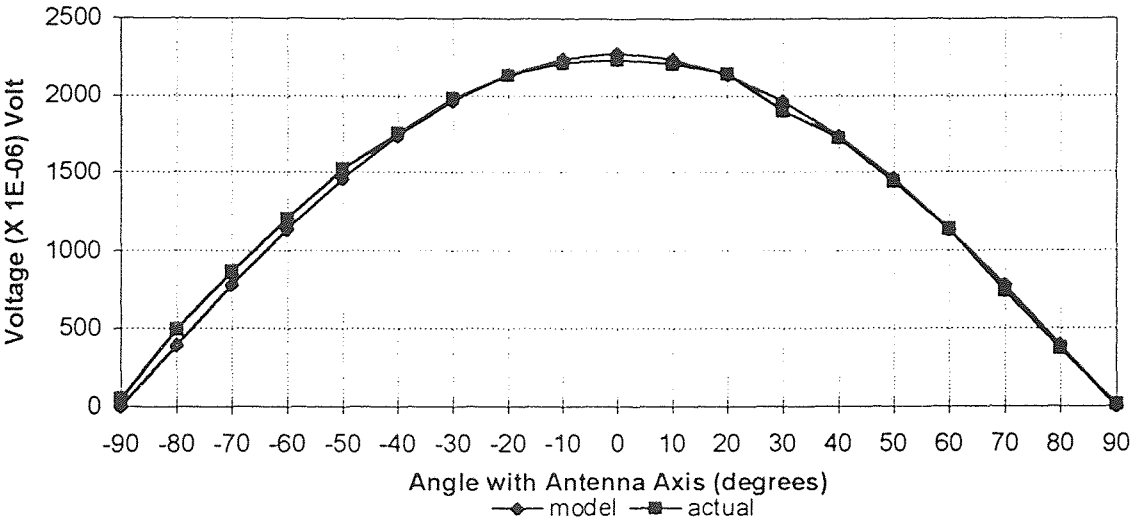

Figure A.18 M-R (III) using 27 point correction, calibration point [001]

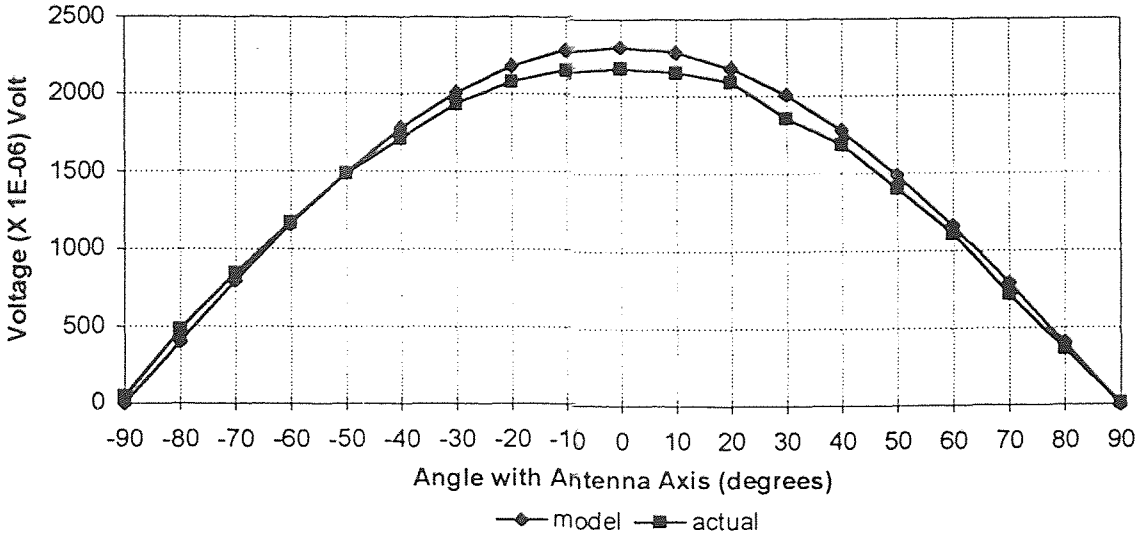

Figure A.19 M-R (III) no 27 point correction, calibration point [002]

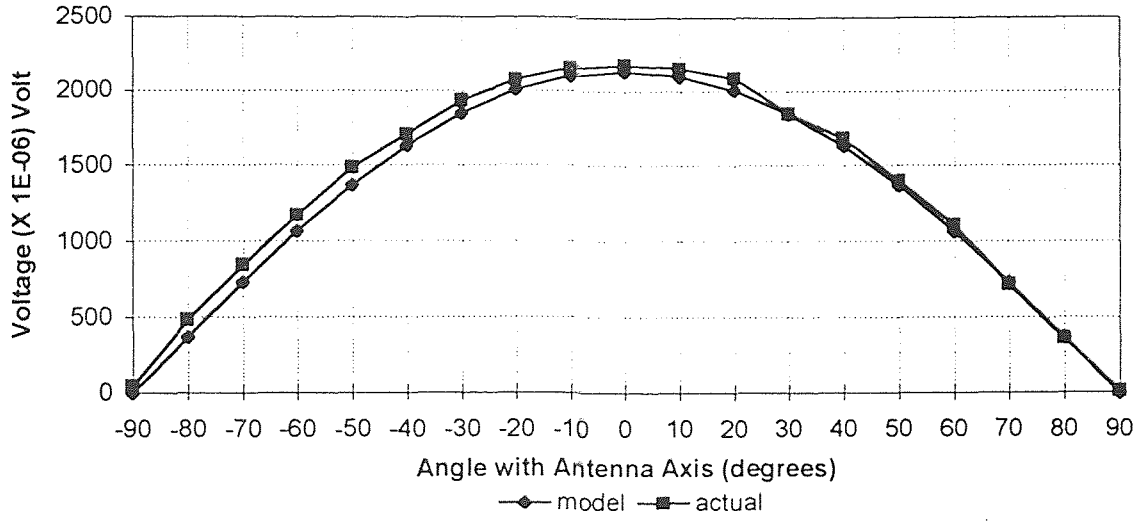

Figure A.20 M-R (III) using 27 point correction, calibration point [002]

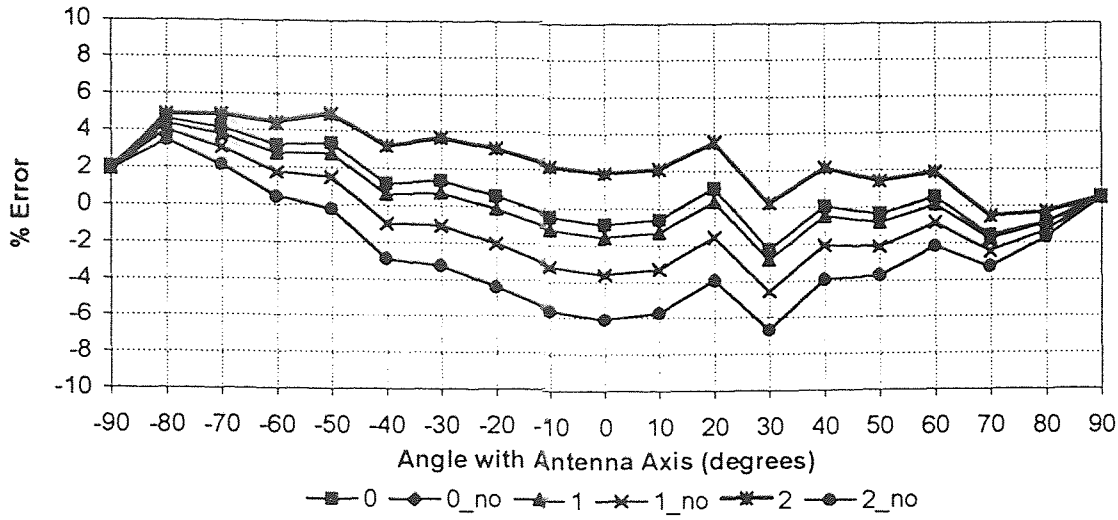

Figure A.21 Error Plot for M-R (III)

APPENDIX B

ADDITIONAL PLOTS FOR CHAPTER 4

The data for all of these plots was collected using the old transmitter (used by Agrawal [9] for experiments and initial work on the 27-point scheme) and an antenna of dimensions 20" X 20". The trajectories used for these plots are explained in Section 3.3. Each plot has four data series --

1. Voltage obtained from the DAS, calibrated using point [002] (actual)

2. Theoretical voltage corrected using 27-point correction scheme as explained in Chapter 3. (with 27 point)

3. Theoretical voltage corrected using the empirical equation as explained in Chapter 4. (with eqn)

The voltages are scaled up by a factor of 10^6 for better visualization.

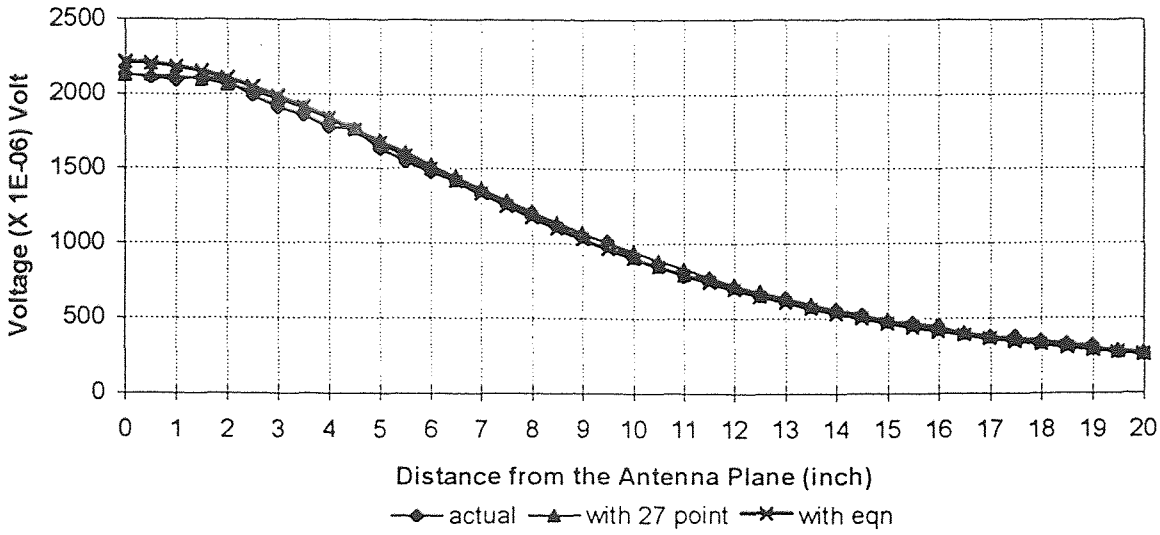

Figure B.1 Effect of empirical equation: M-R (I)

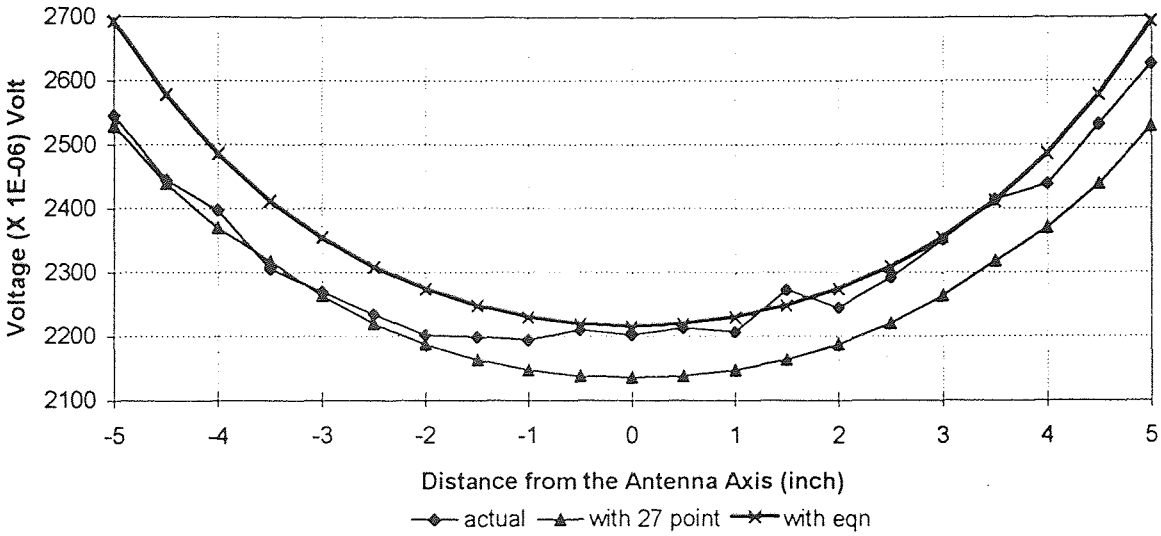

Figure B.2 Effect of empirical equation: M-R (II)

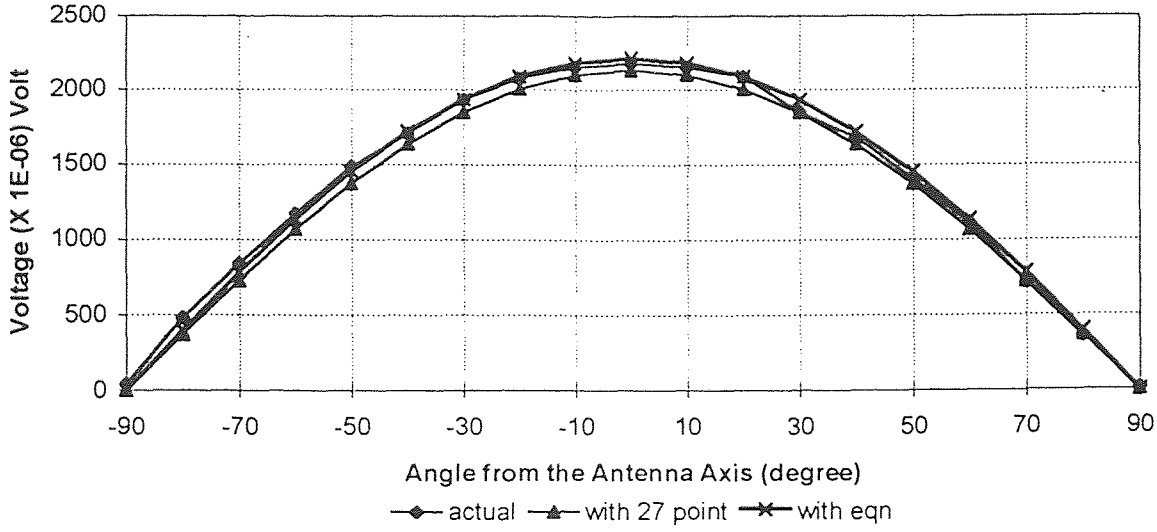

Figure B.3 Effect of empirical equation: M-R (III)

APPENDIX C

EQUIVALENT ANGLE-AXIS REPRESENTATION

Equivalent angle-axis representation of orientation is introduced in Section 5.2 as a means of better visualizing the orientations and detecting multiple solutions. The method of converting the solution obtained in the form of rotation α about x-axis, rotation β about y-axis and rotation γ about z-axis is converted into an equivalent rotation θ about an axis (k_x, k_y, k_z) using the formulae given below (adapted from Paul [11] and Craig [19]).

The RPY transformation matrix given by equation (5.1) in a simple form can be represented by equation (C.1).

$$T = \begin{bmatrix} n_x & o_x & a_x \\ n_y & o_y & a_y \\ n_z & o_z & a_z \end{bmatrix} \tag{C.1}$$

The values of the terms of this matrix are the same as those of the transformation matrix for equivalent angle-axis representation but the meaning of each term is different and is given by equation (C.2)

$$T = \begin{bmatrix} k_x k_x(1-\cos\theta)+\cos\theta & k_y k_x(1-\cos\theta)-k_z\sin\theta & k_z k_x(1-\cos\theta)+k_y\sin\theta \\ k_x k_y(1-\cos\theta)+k_z\sin\theta & k_y k_y(1-\cos\theta)+\cos\theta & k_z k_y(1-\cos\theta)-k_x\sin\theta \\ k_x k_z(1-\cos\theta)-k_y\sin\theta & k_y k_z(1-\cos\theta)+k_x\sin\theta & k_z k_z(1-\cos\theta)+\cos\theta \end{bmatrix} \tag{C.2}$$

The values of rotation angle θ and unit vectors k_x, k_y, k_z can be extracted from the matrix T using the equation given below. First of all the value of θ is found by equation (C.3). Then depending on the value of θ, further processing is done to determine the unit vectors k_x, k_y and k_z.

$$\theta = a\tan\left(\frac{+\sqrt{\left(o_z - a_y\right)^2 + \left(a_x - n_z\right)^2 + \left(n_y - o_x\right)^2}}{\left(n_x + o_y + a_z - 1\right)}\right) \quad ; \; 0^0 \le \theta \le 180^0 \qquad \text{(C.3)}$$

If $\theta < 90^\circ$, then the values of k_x, k_y and k_z are obtained straight-away from equations (C.4), (C.5) and (C.6) respectively.

$$k_x = \frac{o_z - a_y}{2\sin\theta} \qquad \text{(C.4)}$$

$$k_y = \frac{a_x - n_z}{2\sin\theta} \qquad \text{(C.5)}$$

$$k_z = \frac{n_y - o_x}{2\sin\theta} \qquad \text{(C.6)}$$

In case $\theta > 90^\circ$, then we need to analyze the values of k_x, k_y and k_z given by equations (C.7), (C.8) and (C.9) and then depending on these values, use the applicable equations (C.10) to (C.15) to find k_x, k_y and k_z. First we pick the largest component, k_x, k_y or k_z of the unit vector $\hat{k}$.

$$k_x = \mathrm{sgn}\left(o_z - a_y\right)\sqrt{\frac{n_x - \cos\theta}{1 - \cos\theta}} \qquad \text{(C.7)}$$

$$k_y = \mathrm{sgn}\left(a_x - n_z\right)\sqrt{\frac{o_y - \cos\theta}{1 - \cos\theta}} \qquad \text{(C.8)}$$

$$k_z = \mathrm{sgn}\left(n_y - o_x\right)\sqrt{\frac{a_z - \cos\theta}{1 - \cos\theta}} \qquad \text{(C.9)}$$

where,

$$\mathrm{sgn}(e) = +1 \; ; \; if \; e \ge 0^0$$
$$\mathrm{sgn}(e) = -1 \; ; \; if \; e < 0^0$$

If k_x is the largest component of $\hat{k}$, then the other components of $\hat{k}$ are given by equations (C.10) and (C.11).

$$k_y = \frac{n_y + o_x}{2k_x(1-\cos\theta)} \tag{C.10}$$

$$k_z = \frac{a_x + n_z}{2k_x(1-\cos\theta)} \tag{C.11}$$

If k_y is the largest component of $\hat{k}$, then the other components of $\hat{k}$ are given by equations (C.12) and (C.13).

$$k_x = \frac{n_y + o_x}{2k_y(1-\cos\theta)} \tag{C.12}$$

$$k_z = \frac{o_z + a_y}{2k_y(1-\cos\theta)} \tag{C.13}$$

If k_z is the largest component of $\hat{k}$, then the other components of $\hat{k}$ are given by equations (C.14) and (C.15).

$$k_x = \frac{a_x + n_z}{2k_z(1-\cos\theta)} \tag{C.14}$$

$$k_y = \frac{o_z + a_y}{2k_z(1-\cos\theta)} \tag{C.15}$$

Thus we can extract the values of the equivalent rotation angle θ about an axis $\hat{k}$ with components k_x, k_y and k_z from the transformation matrix T.

APPENDIX D

VIBRATED BED PLOTS

Three complete sets of tracking results for the vibrated bed experiment are presented here. Figures D.1 through D.6 are the results obtained by vibrating the bed at a frequency of 10 Hz with an amplitude of 0.175". Figures D.7 through D.12 are the results obtained by vibrating the bed at a frequency of 15 Hz with an amplitude of 0.125". Figures D.13 through D.18 are the results obtained by vibrating the bed at a frequency of 20 Hz with an amplitude of 0.2".

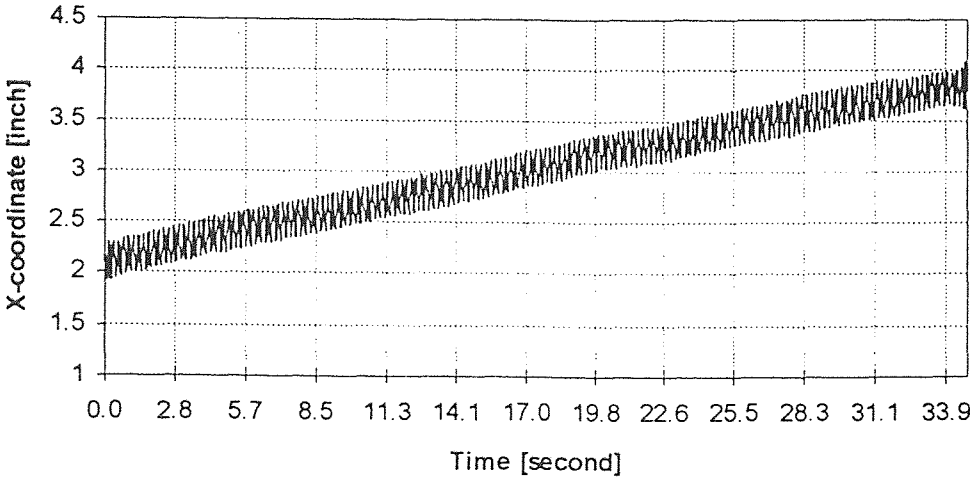

Figure D.1 Vibrated Bed (f = 10 Hz, a = 0.175"): X plot

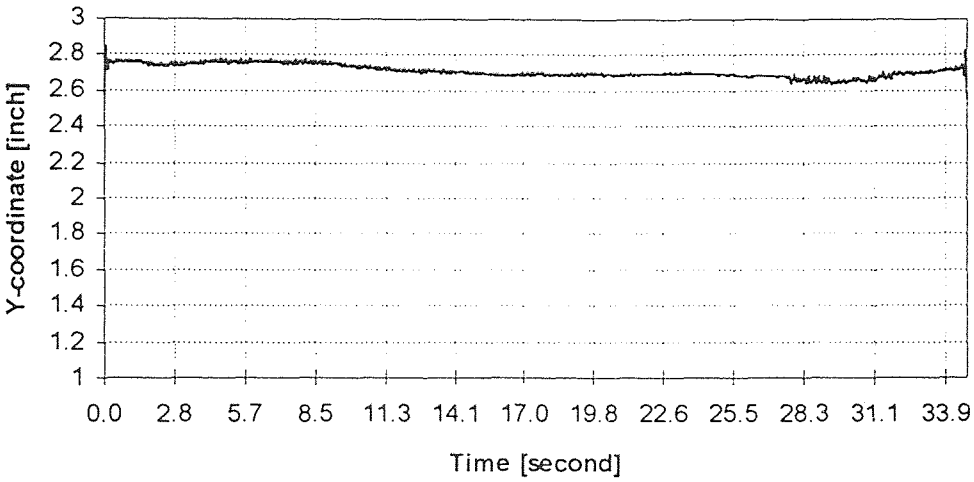

Figure D.2 Vibrated Bed (f = 10 Hz, a = 0.175"): Y plot

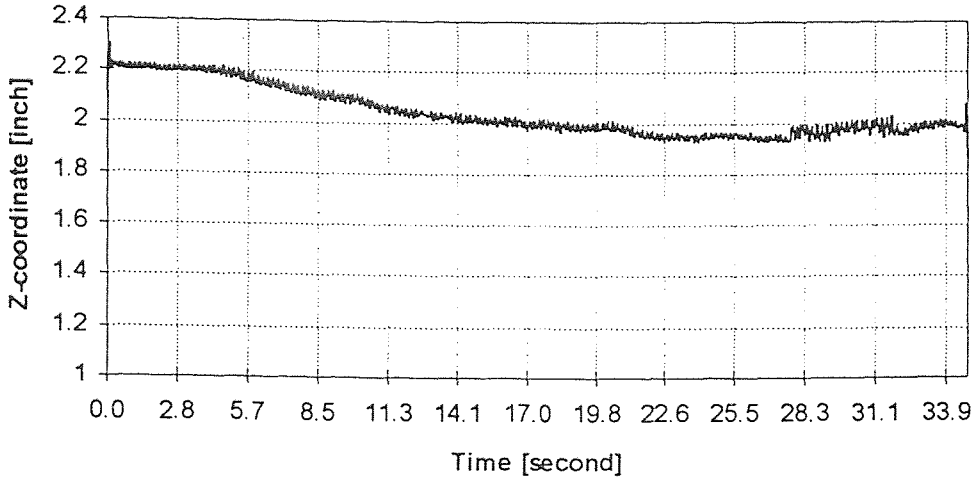

Figure D.3 Vibrated Bed (f = 10 Hz, a = 0.175"): Z plot

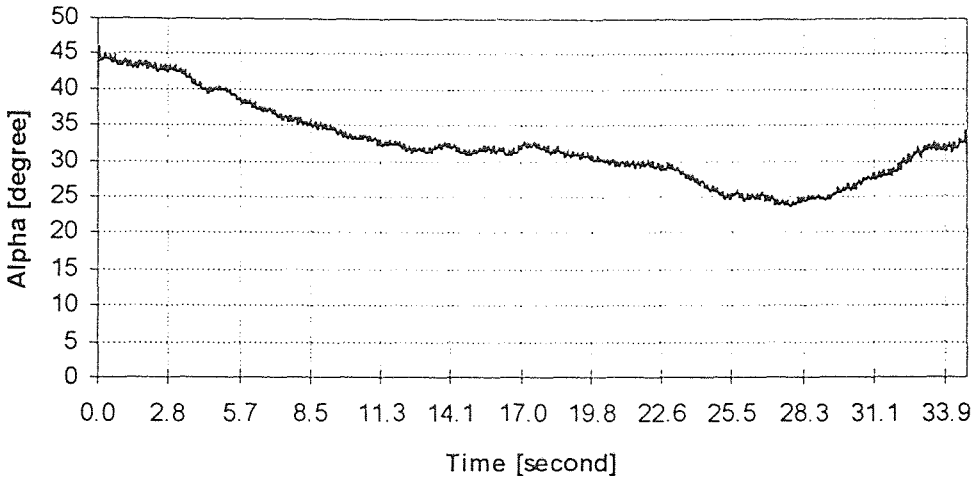

Figure D.4 Vibrated Bed (f = 10 Hz, a = 0.175"): α plot

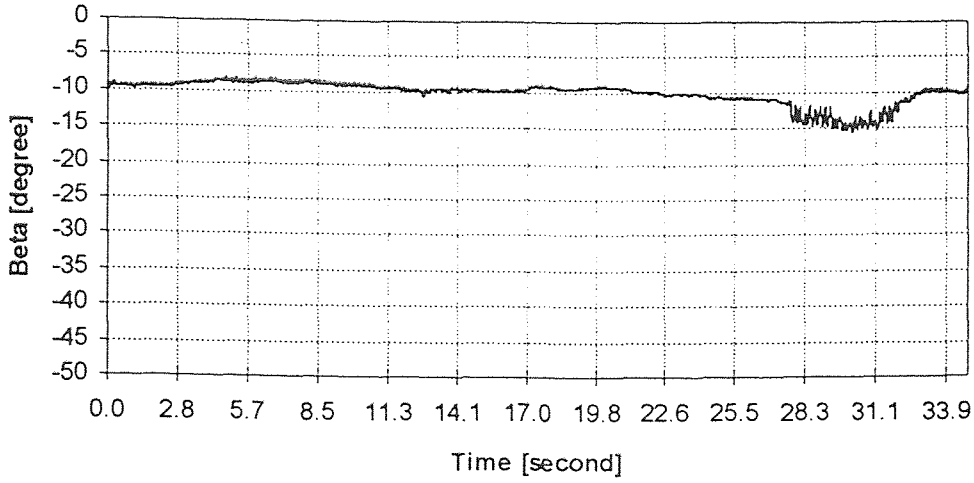

Figure D.5 Vibrated Bed (f = 10 Hz, a = 0.175"): β plot

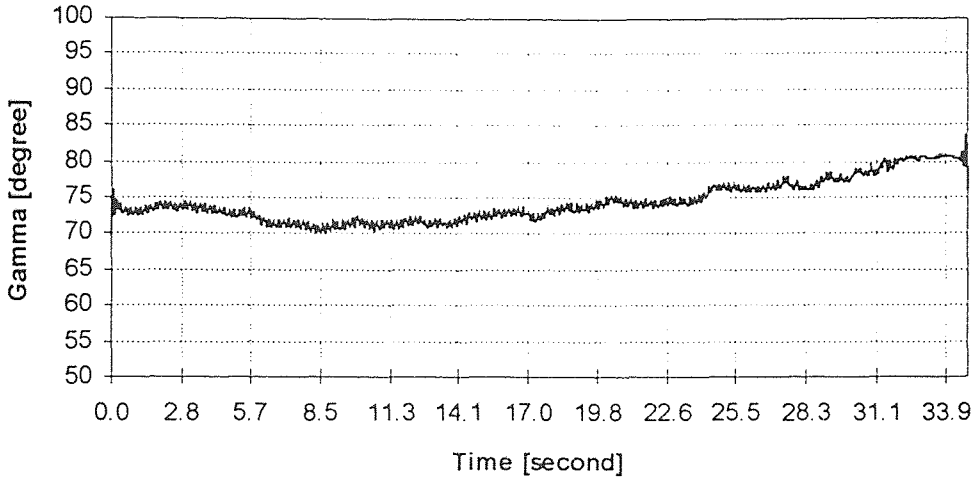

Figure D.6 Vibrated Bed (f = 10 Hz, a = 0.175"): γ plot

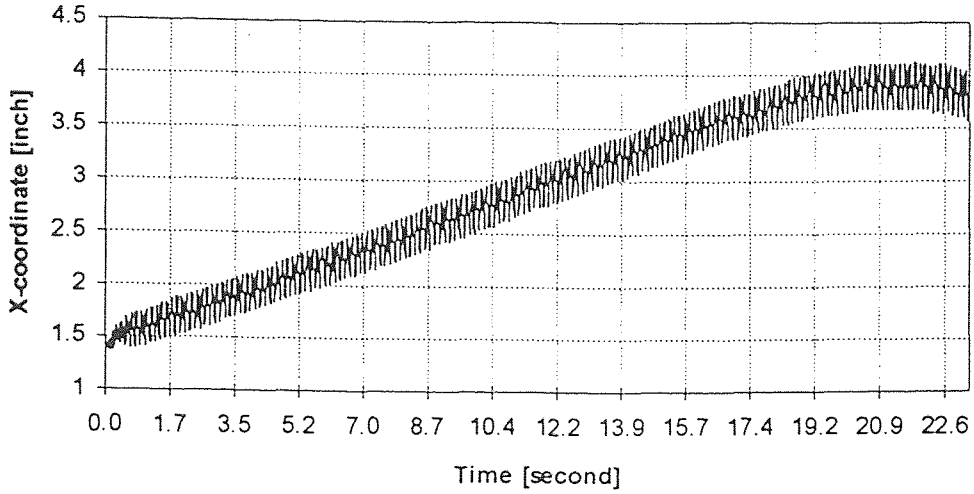

Figure D.7 Vibrated Bed (f = 15 Hz, a = 0.125"): X plot

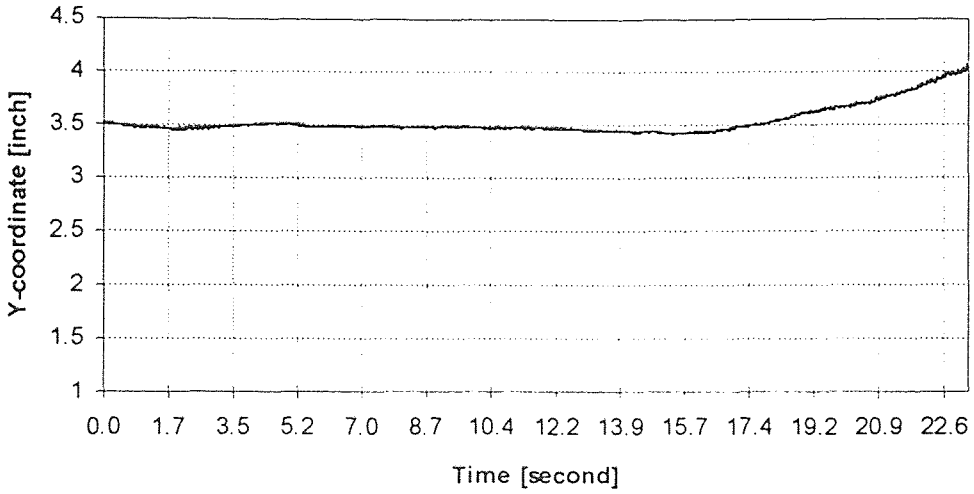

Figure D.8 Vibrated Bed (f = 15 Hz, a = 0.125"): Y plot

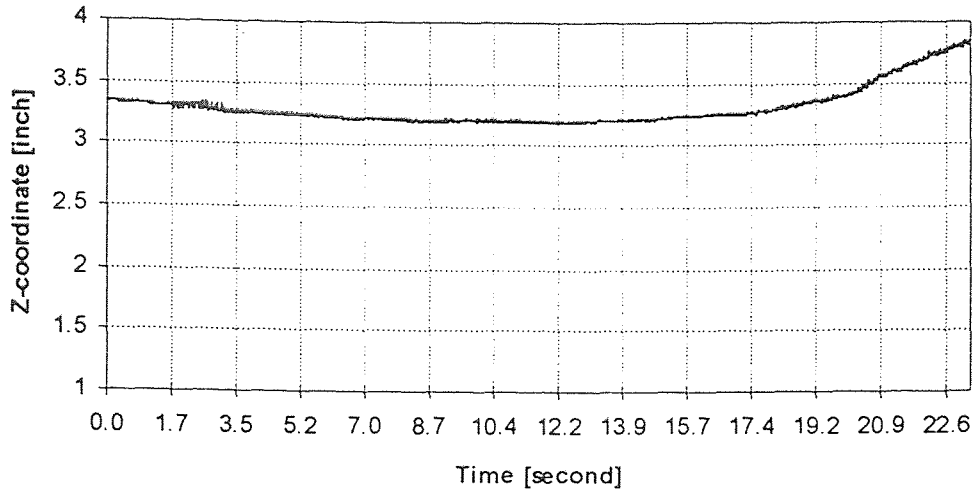

Figure D.9 Vibrated Bed (f = 15 Hz, a = 0.125"): Z plot

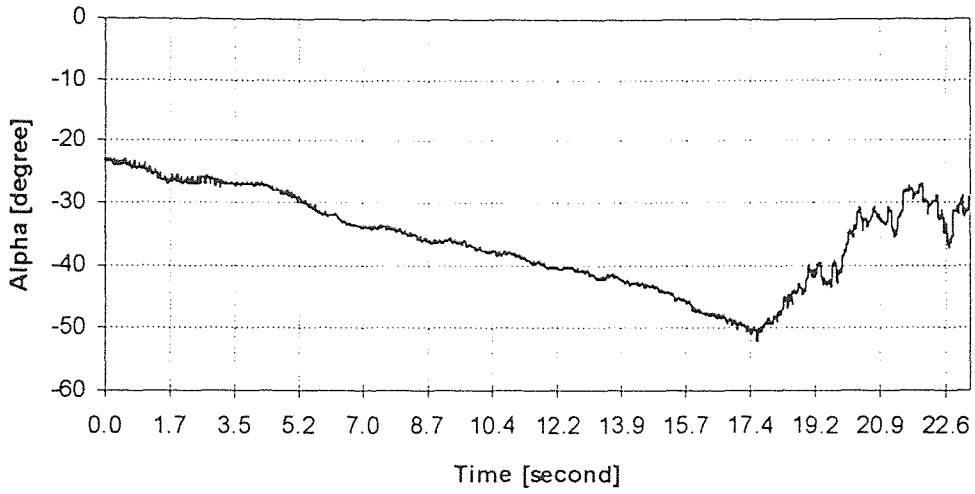

Figure D.10 Vibrated Bed (f = 15 Hz, a = 0.125"): α plot

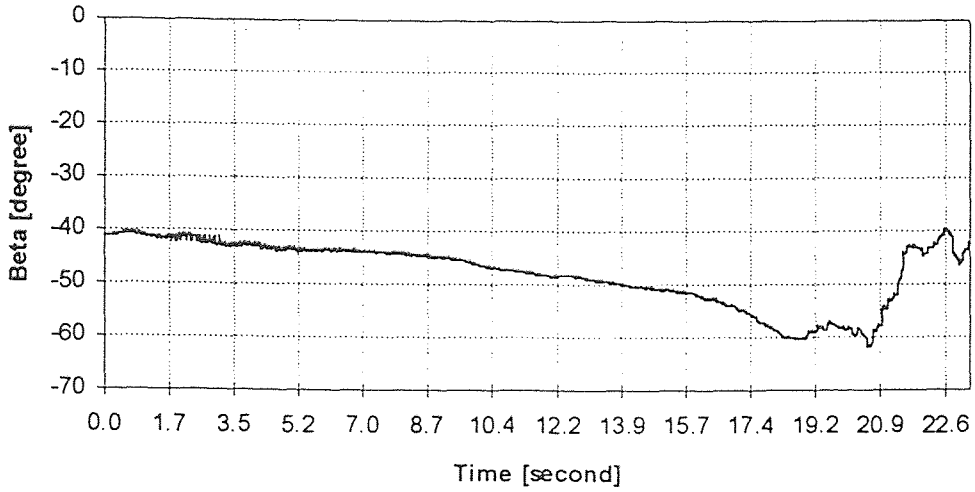

Figure D.11 Vibrated Bed (f = 15 Hz, a = 0.125"): β plot

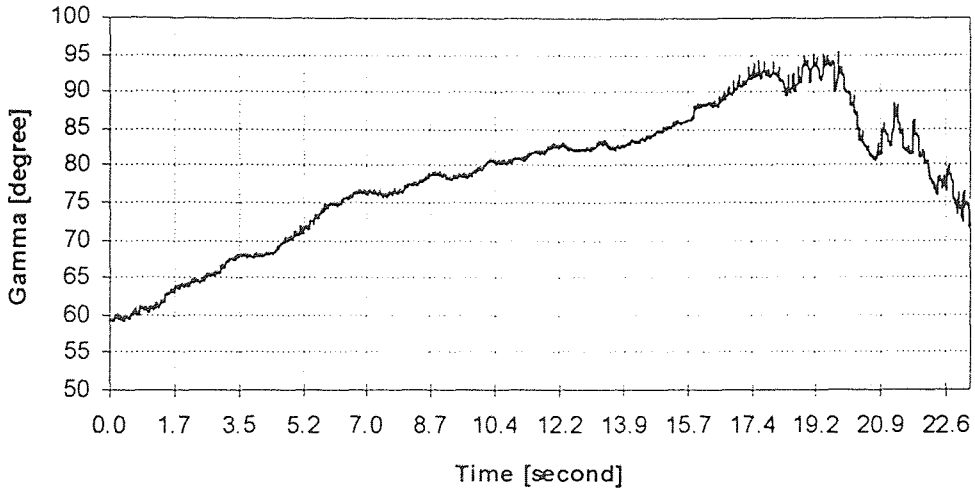

Figure D.12 Vibrated Bed (f = 15 Hz, a = 0.125"): γ plot

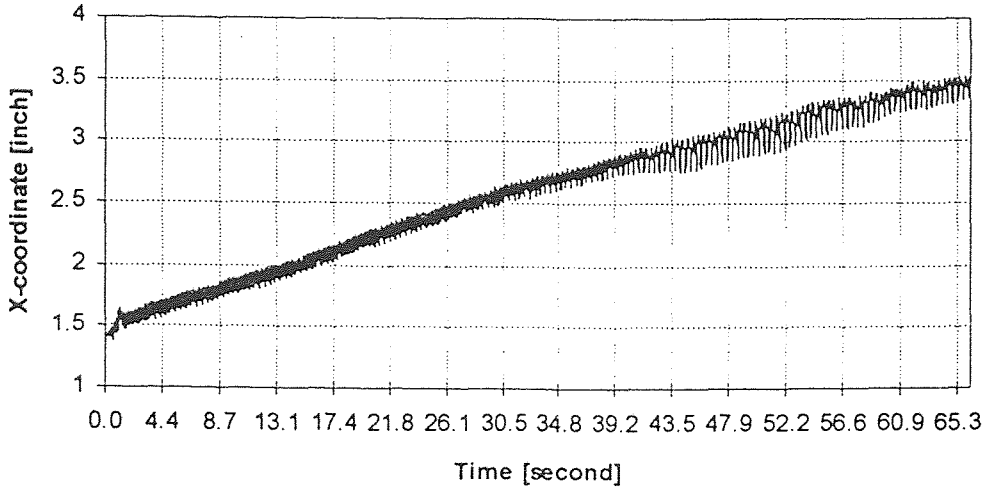

Figure D.13 Vibrated Bed (f = 20 Hz, a = 0.2"): X plot

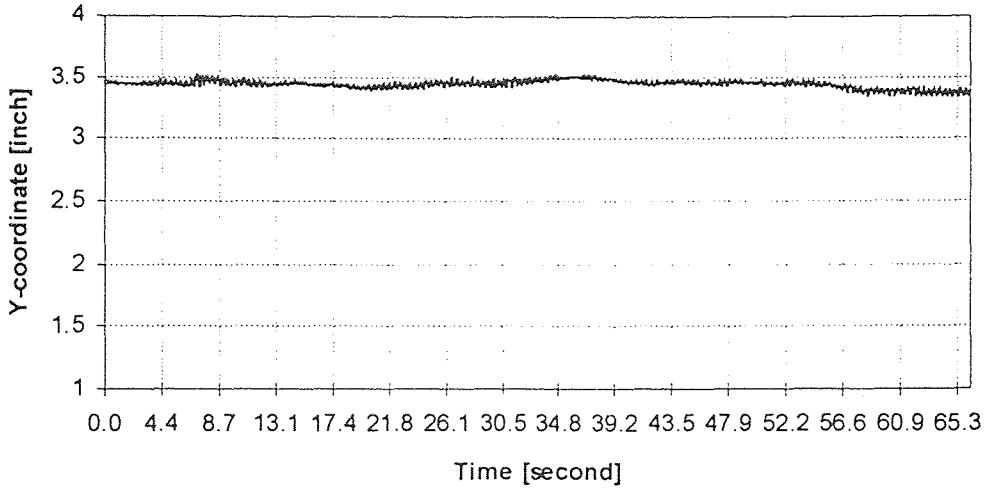

Figure D.14 Vibrated Bed (f = 20 Hz, a = 0.2"): Y plot

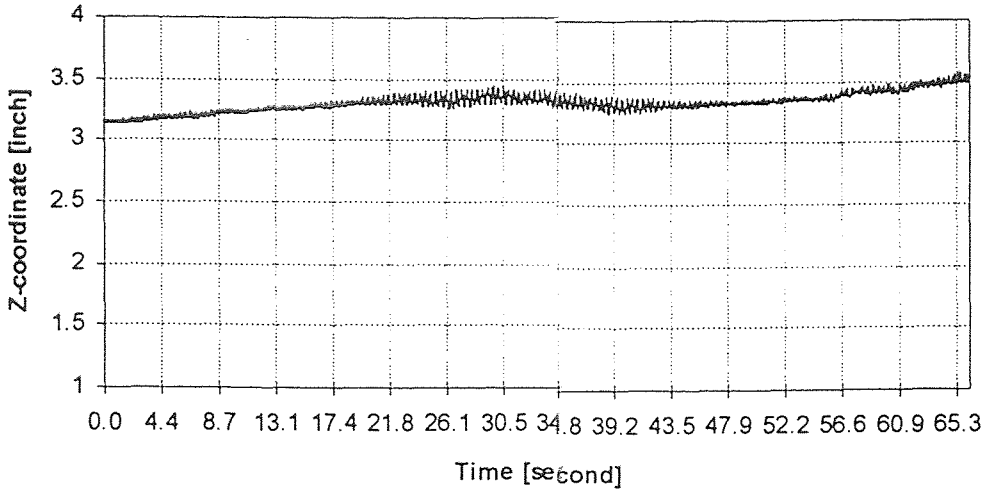

Figure D.15 Vibrated Bed (f = 20 Hz, a = 0.2"): Z plot

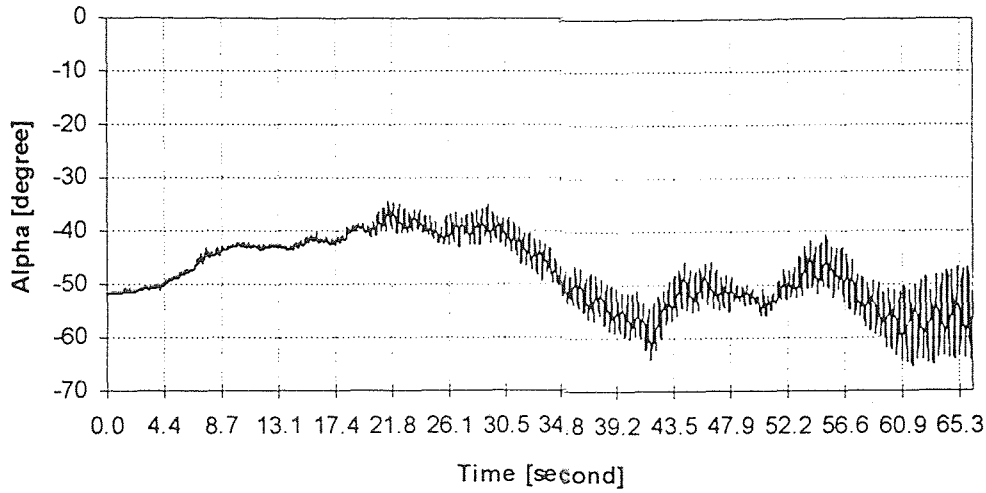

Figure D.16 Vibrated Bed (f = 20 Hz, a = 0.2"): α plot

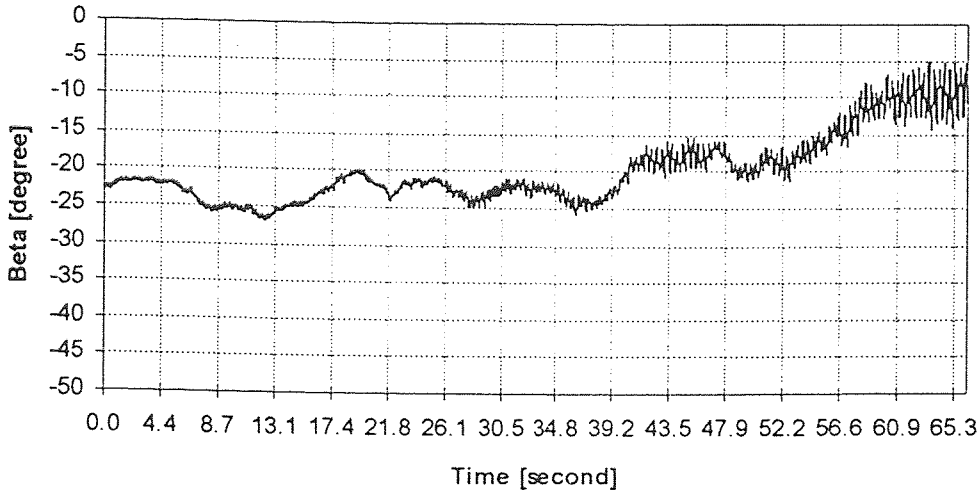

Figure D.17 Vibrated Bed (f = 20 Hz, a = 0.2"): β plot

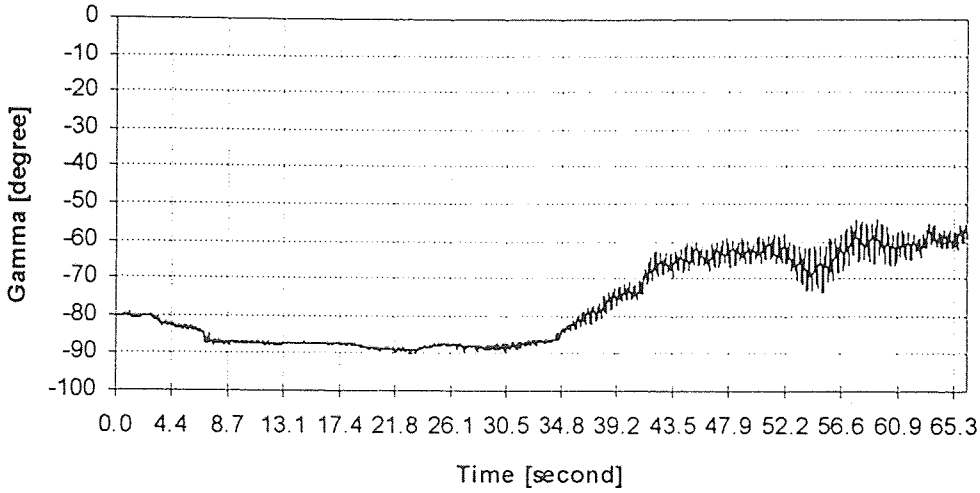

Figure D.18 Vibrated Bed (f = 20 Hz, a = 0.2"): γ plot

APPENDIX E

INCLINED CHUTE PLOTS

Two complete sets of tracking results of controlled trajectories obtained using the top as well as the bottom half of the inclined chute setup are presented here. The experiments are performed by holding the tracking sphere in the calibration jig and incrementally changing one of the coordinates x, y, z, α, β or γ.

Figures E.1 to E.6 are results of the run "ctstrt" carried out in the top half of the chute. The jig (and thus the transmitter) is moved along the global x-axis from x=10" to x=54" in 2" increments keeping the y and z coordinates fixed at 12". Rotations α, β and γ are zero degrees.

Figures E.7 to E.12 are results of the run "cbgamma" carried out in the bottom half of the chute. The jig (and thus the transmitter) is kept at x=90", y=12" and z=12". Rotations α and β are kept zero degrees and the transmitter is rotated 180° about the z-axis (i.e. γ = -90° to 90°) at 10° increments.

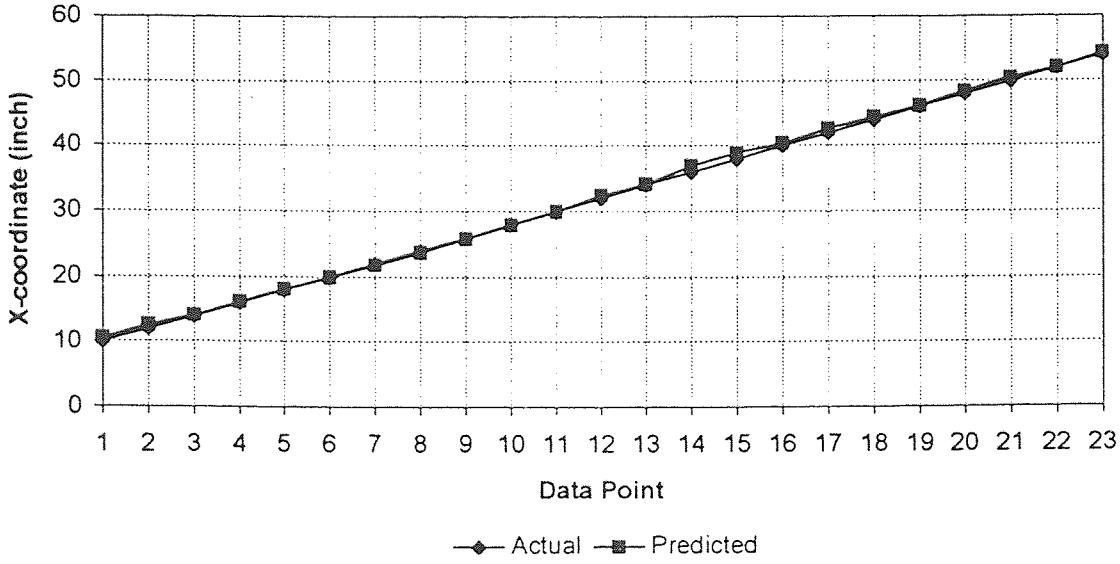

Figure E.1 Run ctstrt: X plot
(maximum error = 0.99", mean error = 0.35", standard deviation = 0.25°)

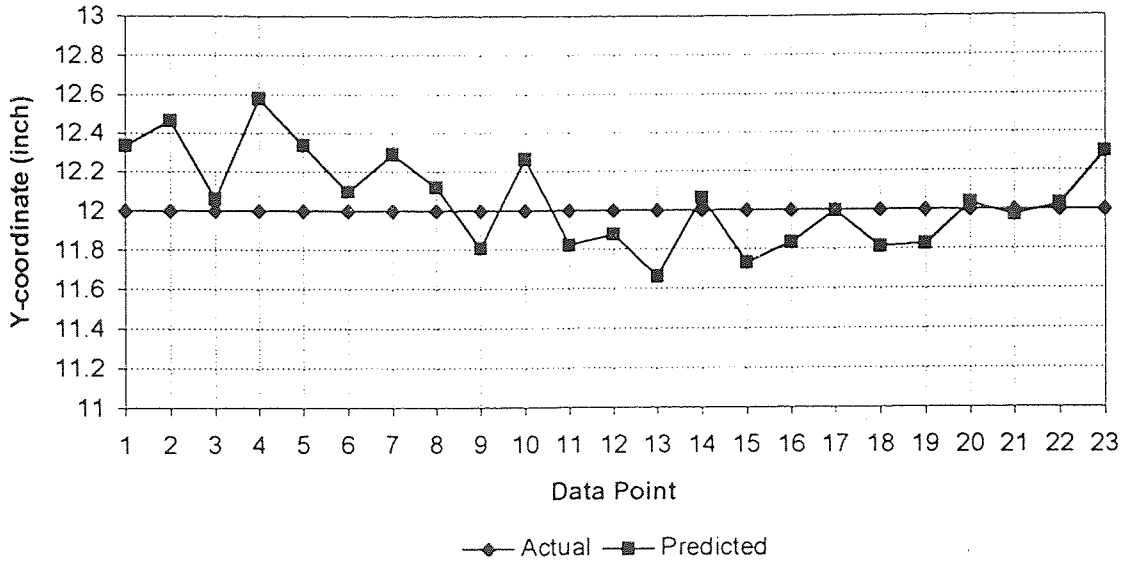

Figure E.2 Run ctstrt: Y plot
(maximum error 0.58", mean error = 0.20", standard deviation = 0.14")

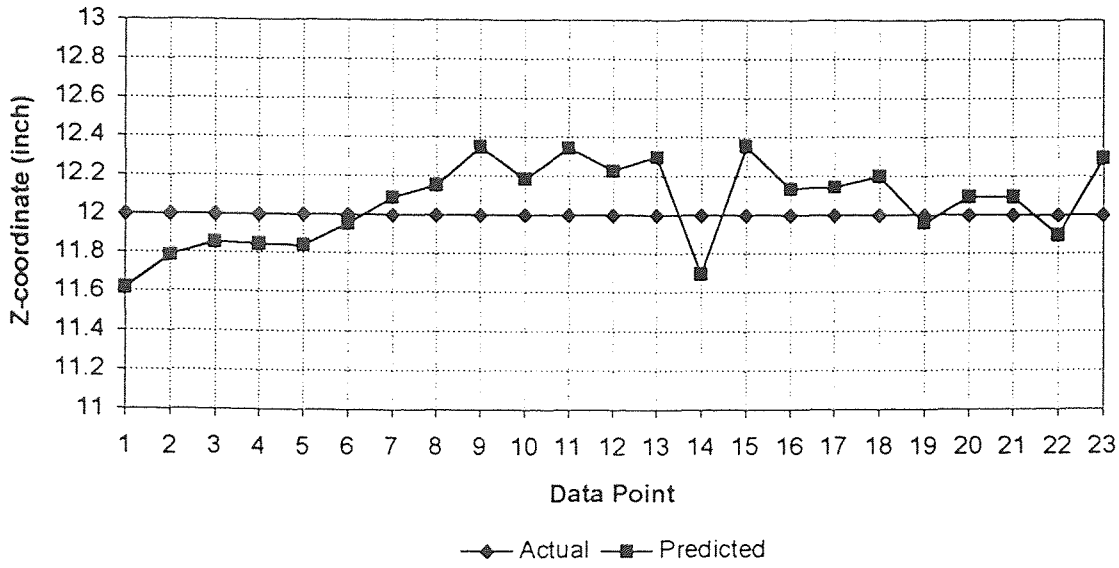

Figure E.3 Run ctstrt: Z plot
(maximum error = 0.38", mean error = 0.19", standard deviation = 0.10")

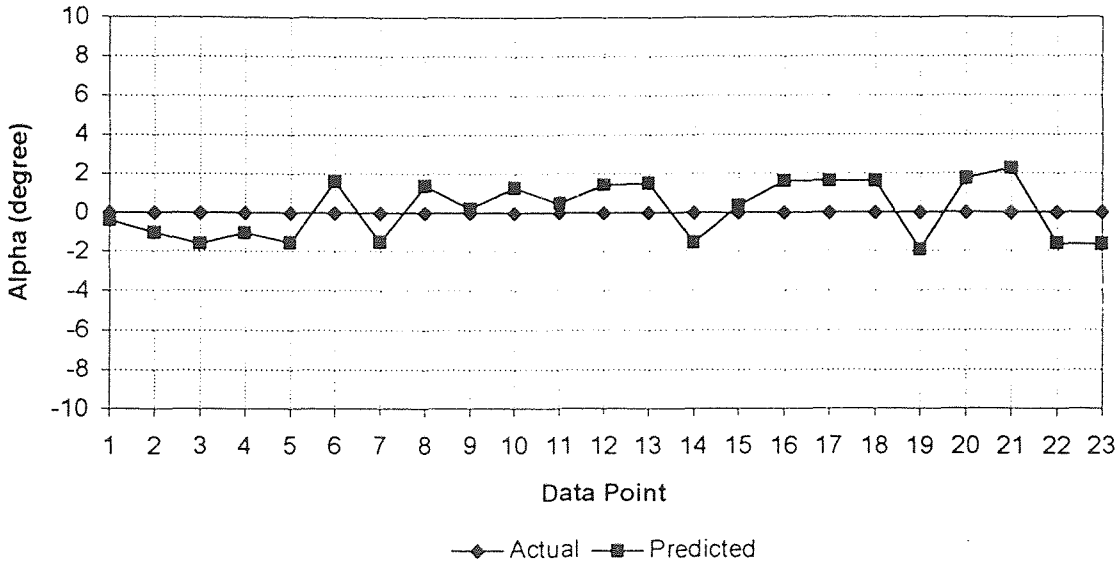

Figure E.4 Run ctstrt: α plot
(maximum error =2.28°, mean error = 1.34°, standard deviation =0.50°)

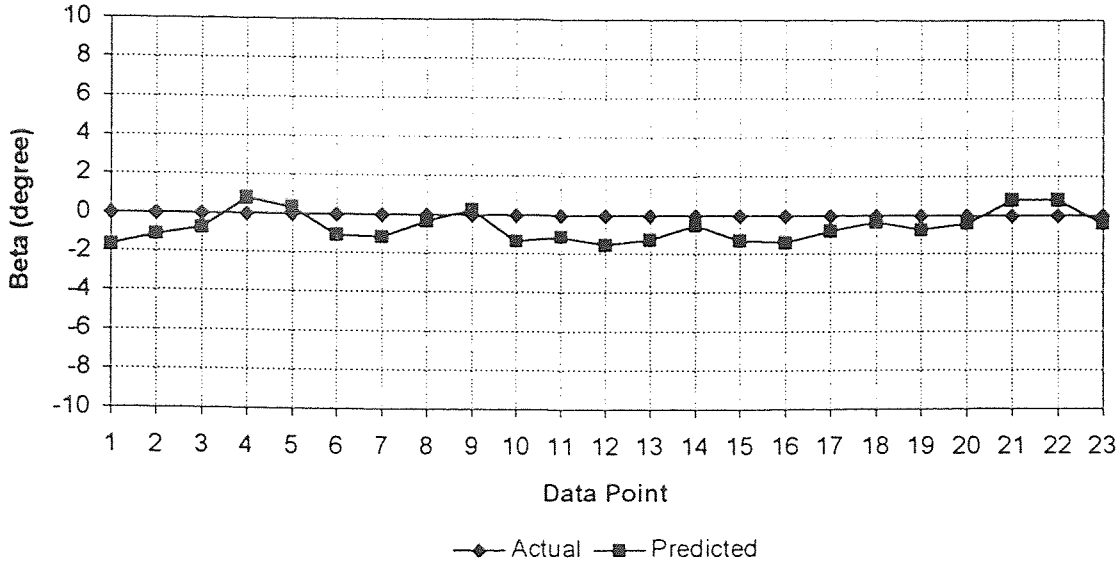

Figure E.5 Run ctstrt: β plot
(maximum error =1.69°, mean error = 0.87°, standard deviation =0.41°)

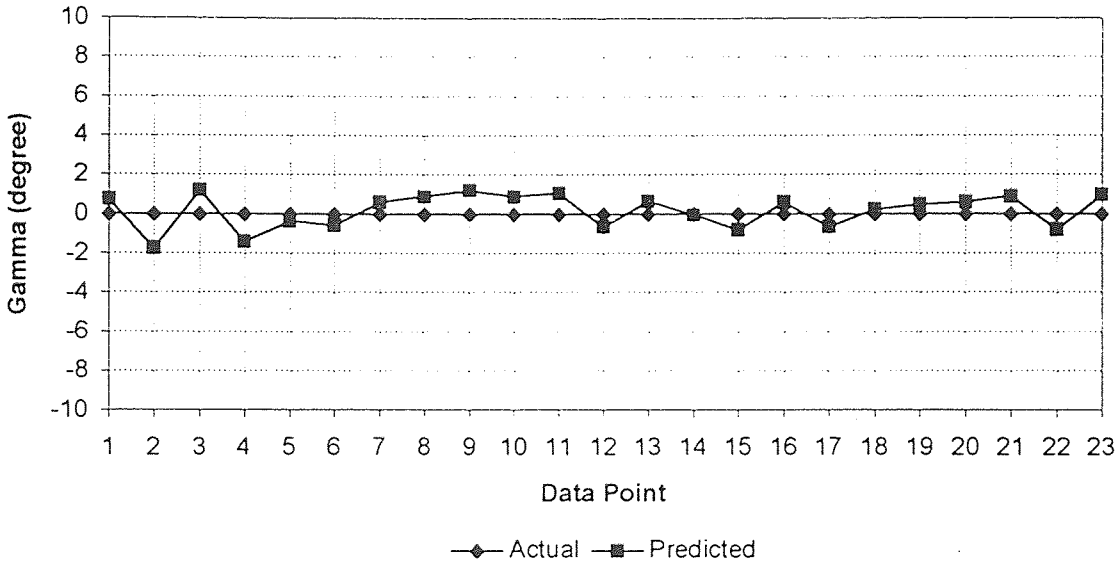

Figure E.6 Run ctstrt: γ plot
(maximum error =1.72°, mean error = 0.78°, standard deviation =0.36°)

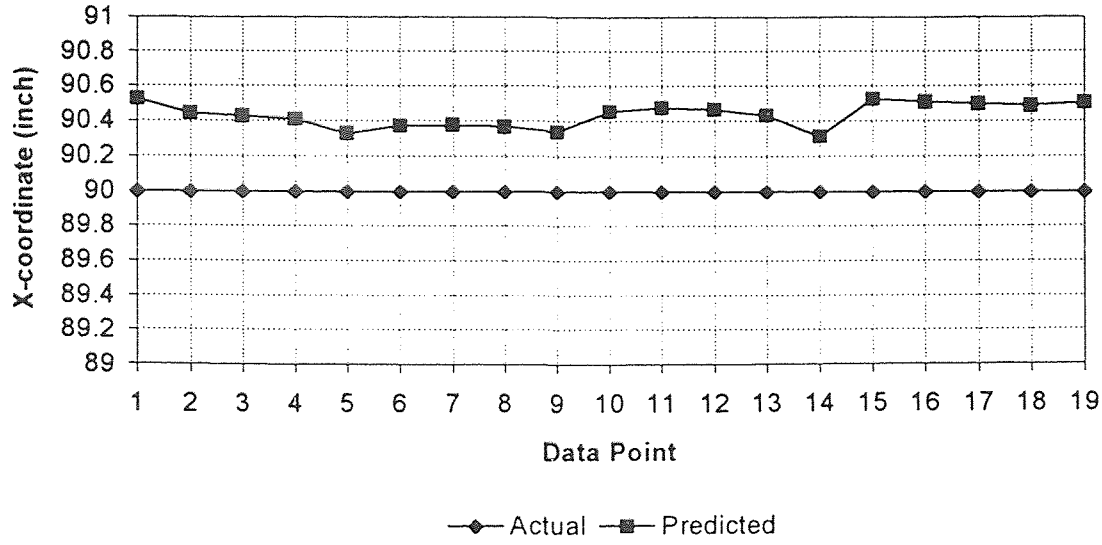

Figure E.7 Run cbgamma: X plot
(maximum error = 0.52", mean error = 0.43", standard deviation = 0.06")

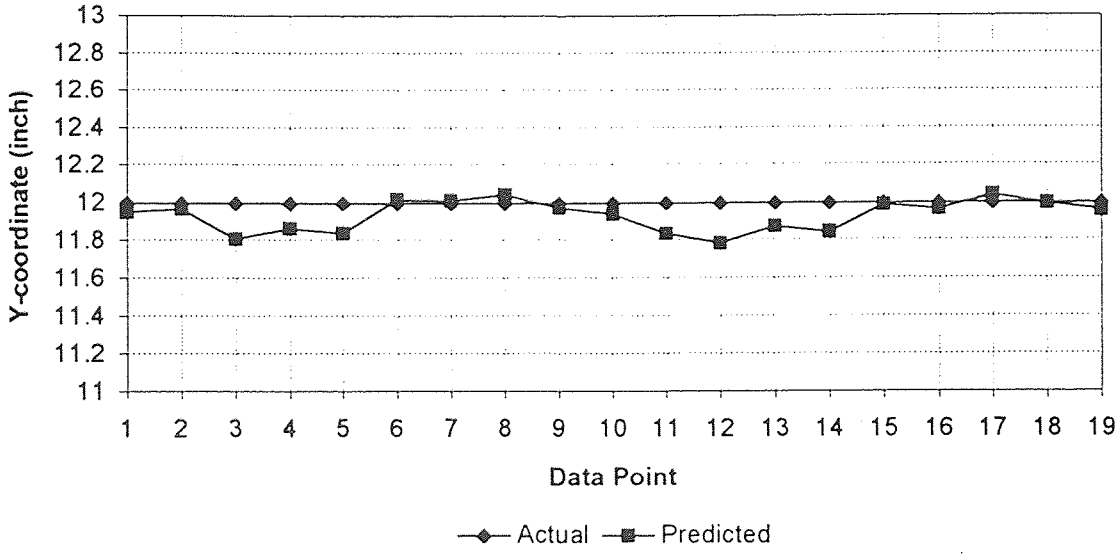

Figure E.8 Run cbgamma: Y plot
(maximum error = 0.21", mean error = 0.08", standard deviation = 0.06")

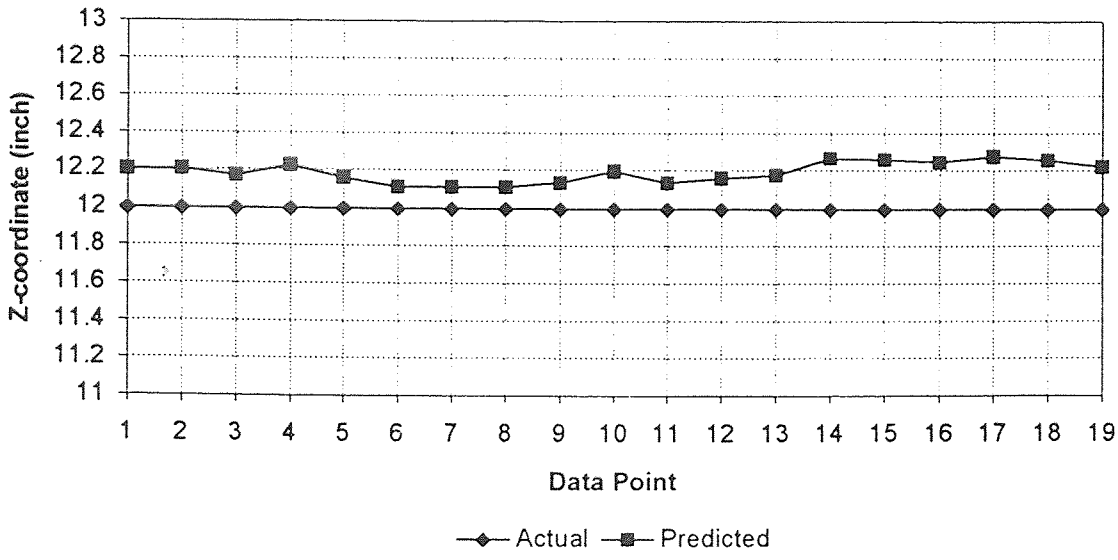

Figure E.9 Run cbgamma: Z plot
(maximum error = 0.27", mean error = 0.19", standard deviation = 0.05")

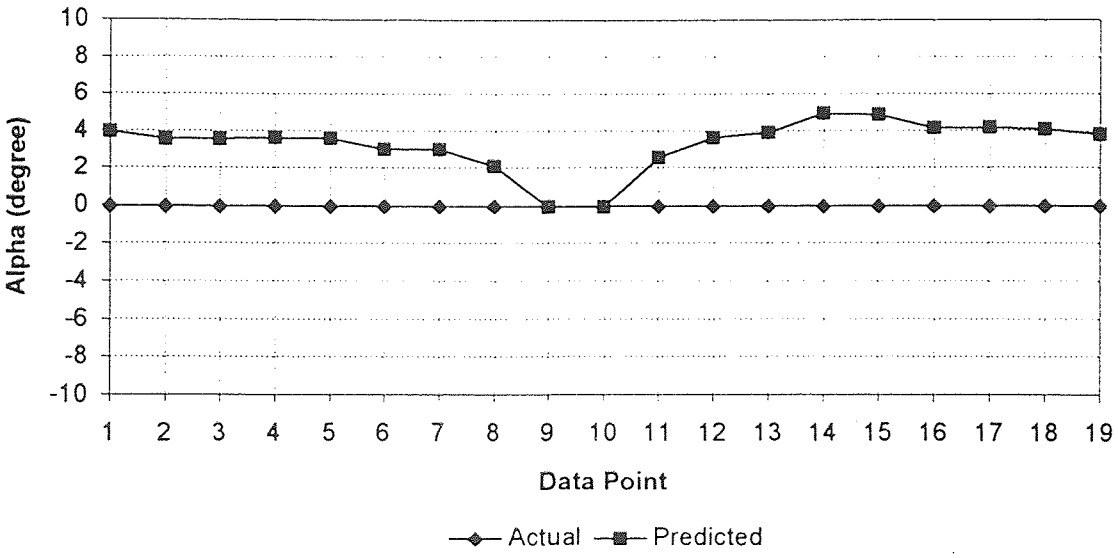

Figure E.10 Run cbgamma: α plot
(maximum error =4.98°, mean error = 3.31°, standard deviation =1.29°)

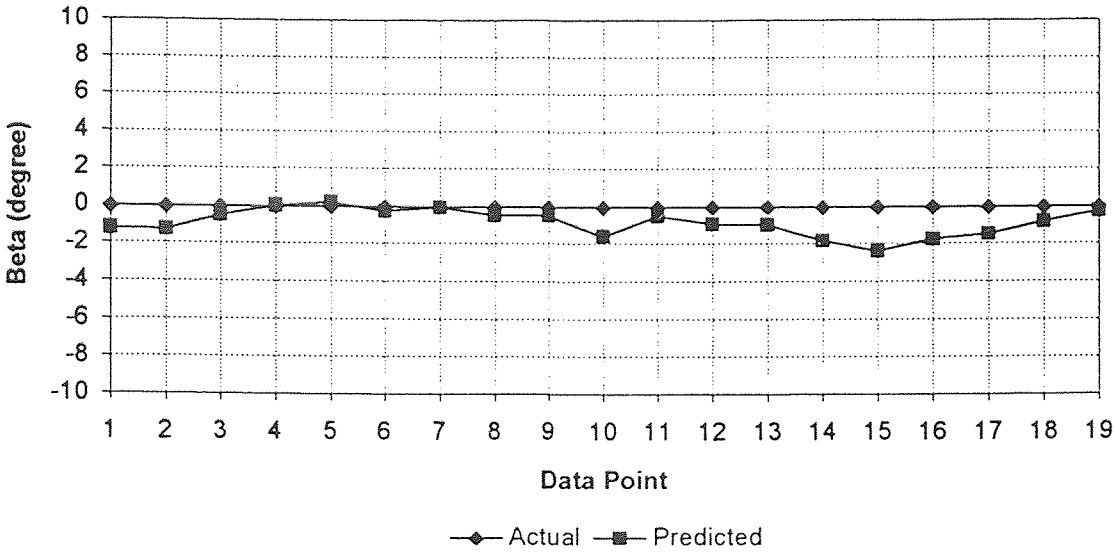

Figure E.11 Run cbgamma: β plot
(maximum error =2.36°, mean error = 0.90°, standard deviation =0.64°)

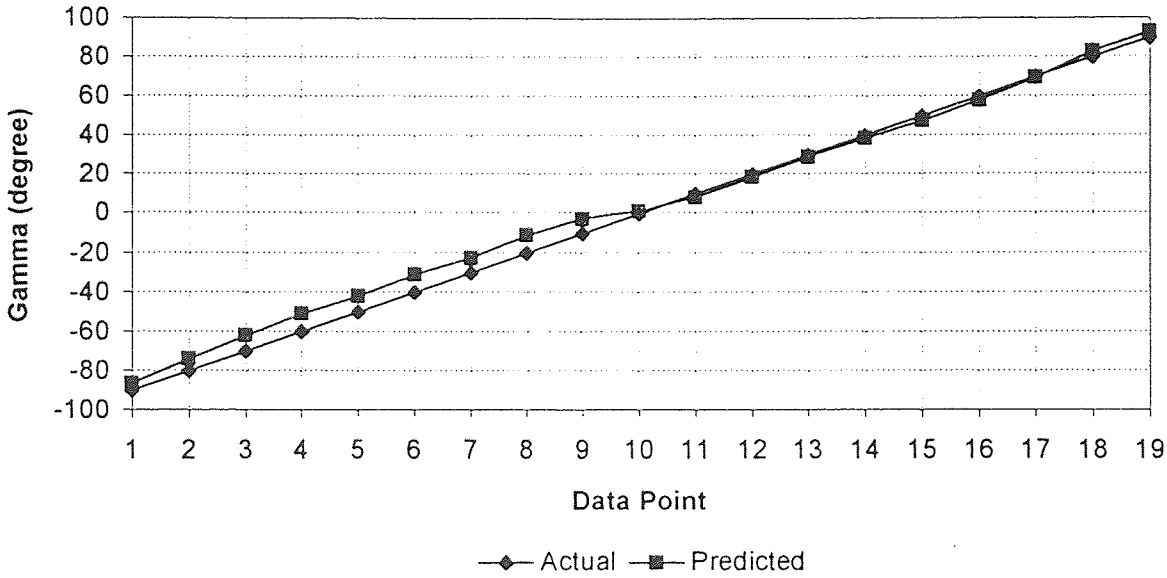

Figure E.12 Run cbgamma: γ plot
(maximum error =8.93°, mean error = 4.34°, standard deviation =3.11°)

REFERENCES

1. Jullien, R., Meakin, P., A Mechanism for Particle Size Segregation in Three Dimensions, *Nature*, p. 425-427, 1990.
2. Knight, J. B., Jaeger, H. M., Nagel, S. R., Vibration Induced Size Separation in Granular Media: the Convection Connection, Preprint, *PhysicalReview Letters*, 1993.2
3. Jullien, R., Meakin, P., Pavlovitch, A., Three Dimensional Model for Particle Size Segregation by Shaking, , p. 640-643, 1992.
4. Duran, J., Rajchenbach, J., Clement, E., Arching Effect Model for Particle Size Segregation, *PhysicalReview Letters*, p. 2431-2434, 1993.
5. Dave, R. N., Ashok, A. S., Bukiet, B. G., On Development of a Three Dimensional Particle Motion Tracking System, *Proceedings of the ASME Winter Annual Meeting*, 1992.
6. Dave R. N., Bukiet, B. G., Non-Intrusive Rigid Body Tracking Technique for Dry Particulate Flows, Part I: Theoretical Aspects, Submitted to *Measurement Science and Technology (Formerly Physics E)*, 1994.
7. Ashok, A. S., Computational Aspects of a Three Dimensional Non-Intrusive Particle Motion Tracking System, *MS Thesis*, New Jersey Institute of Technology, Newark, New Jersey, 1992.
8. Van Valkenburg, M. E., *Network Analysis*, Prentice-Hall, Englewood Cliffs, New Jersey, p. 258-259, 1974.
9. Agrawal, J. H., Use of Multiple Transmitters for 3-D Non-Intrusive Particle Tracking, *MS Thesis*, New Jersey Institute of Technology, 1995.
10. Volcy, J. R., Development of a Non-Intrusive Particle Motion Tracking Technique for Granular Flow Experiments, *MS Thesis*, New Jersey Institute of Technology, Newark, New Jersey, 1994.
11. Paul, R. P., *Robot Manipulators: Mathematics, Programming and Control*, MIT Press, Massachusetts, p. 41-47, 1981.
12. Moré, J. J., Garbow, B. S., Hillstrom, K. E., *User Guide for MINPACK-1: Argonne National Lab Report*, 1980.
13. Moré, J. J., The Levenberg-Marquardt Algorithm: Implementation and Theory, in *Numerical Analysis*, G. A. Watson, ed., Lecture Notes in Math. 630, Springer-Verlag, Berlin, 1977.
14. Patel, P. B., Simulation Study of the Particle Tracking System, *MS Thesis*, New Jersey Institute of Technology, 1995.
15. Zhang, Y., Chute Flow Experiments, *MS Thesis*, New Jersey Institute of Technology, 1995.
16. Troiano, A., Private Communications, New Jersey Institute of Technology, Newark, New Jersey, 1994.

17. Ren, S., Private Communications, New Jersey Institute of Technology, Newark, New Jersey, 1995

18. Dave, R. N., Private Communications, New Jersey Institute of Technology, Newark, New Jersey, 1995.

19. Craig, J. J., *Introduction to Robotics: Mechanics and Control.* Addison-Wesley Publications Company, p. 38-47, 1986.

20. Gupta, V. B., Testing of the Non-Intrusive Particle Tracking System, *Proceedings of the Fifth ASME Region II Graduate Student Technical Conference*, p. 53-54, 1995.

21. La Rosa, A. J., Vibratory Size Segregation of Particulate Matter, *MS Thesis*, New Jersey Institute of Technology, 1993.

22. Rosato, A. D., Dave, R. N., La Rosa, A. J., Mosch E., Experimental Studies of Vibrational 'Size Segregation', *Proceedings of the AIChE First International Particle Technology Forum*, p. 325-330, 1994.

23. Bevington, P. R., *Data Reduction and Error Analysis for the Physical Sciences,* McGraw-Hill Book Company, p. 43-48, 255-260, 1969.

24. Gottschalk, B., *Computers in Physics*, ed. Hayden, p. 74, 1987.

25. Burden, R. L., Faires, J. D., Reynolds, A. C., *Numerical Analysis*, PWS-KENT Publications Company, p. 172-181, 1979.